

ATOM PROBE TOMOGRAPHY OF SMALL-MOLECULE ORGANIC  
SEMICONDUCTING MATERIALS

by  
Andrew P. Proudian

A thesis submitted to the Faculty and the Board of Trustees of the Colorado School of Mines in partial fulfillment of the requirements for the degree of Doctor of Philosophy (Applied Physics).

Golden, Colorado

Date \_\_\_\_\_

Signed: \_\_\_\_\_

Andrew P. Proudian

Signed: \_\_\_\_\_

Dr. Jeramy D. Zimmerman  
Thesis Advisor

Golden, Colorado

Date \_\_\_\_\_

Signed: \_\_\_\_\_

Dr. Uwe Griffe  
Professor and Head  
Department of Physics

## ABSTRACT

For organic electronics, film morphology is crucial to device performance, requiring techniques with both high spatial resolution and chemical sensitivity that are suitable for these materials. This work demonstrates that atom probe tomography (APT) is well-suited to this purpose. It can provide sub-dalton mass resolution, detection thresholds of less than 100 ppm, and spatial distribution of molecules with better than nanometer precision. These capabilities mean that APT can successfully analyze systems of interest to the organic electronics community, revealing new morphological information that can enable better devices through improved understanding of structure-property relationships.

To demonstrate the power of APT to uncover structure-property relationships in organic systems that have proven extremely difficult to probe using existing techniques, three examples are discussed: (1) a model organic photovoltaic system in which a chemical reaction occurs at the heterointerface, explaining a change in open circuit voltage; (2) a model organic light-emitting diode (OLED) system in which molecular segregation occurs in the emissive layer bulk, which has ramifications for efficiency; and (3) controlled ultraviolet exposure of an OLED emitter in which photodegradation occurs, quantifying degradation product hierarchies. These examples illustrate the power of APT to enable new insights into organic molecular materials.

Additionally, a new tomographic reconstruction method is presented that corrects for near field trajectory aberrations. It does so by correcting for detector density fluctuations in an unbiased way that generates an ensemble of solutions. This is demonstrated with a simulated sample of amorphous Si with small B clusters, a system in which there is a large field difference that can completely obscure clustering signal. Comparing this new method with the standard commercial protocol, the new method improves the accuracy of reconstruction and allows for better spatial signal recovery. This enables analysis of more

challenging materials systems with APT.

APT creates numerous opportunities for studying organic electronic systems. As a result of its spatially resolved chemical information, APT allows for quantitative understanding of composition, morphology, phase behavior, device physics, and device degradation. APT is invaluable for furthering our understanding of organic electronic systems and enables us to collect information that was previously inaccessible.

## TABLE OF CONTENTS

ABSTRACT . . . . .	iii
LIST OF FIGURES . . . . .	vii
LIST OF TABLES . . . . .	xiii
ACKNOWLEDGMENTS . . . . .	xiv
DEDICATION . . . . .	xvi
CHAPTER 1 INTRODUCTION . . . . .	1
CHAPTER 2 BACKGROUND . . . . .	7
2.1 Organic Electronics . . . . .	7
2.2 Atom Probe Tomography . . . . .	9
2.3 Spatial Statistics . . . . .	16
CHAPTER 3 VALIDATION . . . . .	19
CHAPTER 4 SCIENTIFIC DISCOVERIES . . . . .	36
4.1 Interface . . . . .	36
4.2 Bulk . . . . .	44
4.3 Degradation . . . . .	48
CHAPTER 5 RECONSTRUCTION . . . . .	62
5.1 Source-Sink Process . . . . .	64
5.2 Spatial Signal and Testing . . . . .	67
5.3 Methods . . . . .	68
5.4 Results and Discussion . . . . .	70

5.5 Conclusion . . . . .	74
CHAPTER 6 CONCLUSION . . . . .	76
REFERENCES CITED . . . . .	80
APPENDIX A TAPSIM PARAMETERS . . . . .	95
A.1 Mesh Generation Configuration . . . . .	95
A.2 Sample Configuration . . . . .	97
A.3 Evaporation Configuration . . . . .	100
APPENDIX B EVAPORATION FIELDS . . . . .	103
B.1 Radius Only $F_E$ Estimation . . . . .	103
B.2 $F_E$ Including $E_p$ and $T$ . . . . .	107
B.2.1 Application to Ir(ppy) <sub>3</sub> . . . . .	108
B.2.2 Estimating $F_E$ from Table 3.1 . . . . .	111

## LIST OF FIGURES

Figure 2.1	<p>A schematic of the atom probe tomography (APT) process: A sample prepared with a sub-micrometer radius of curvature is held at cryogenic temperatures in UHV under high bias, generating a large local electric field. A voltage or laser pulse of adequate intensity causes an atom or molecule on the surface to field evaporate. The electric field accelerates this ion towards a two-dimensional position- and time-sensitive detector. This process repeats until the desired thickness of sample has evaporated. The time-of-flight of each ion gives its mass-to-charge ratio, and its position on the detector and sequence of detection allows the ion's location to be reconstructed in three dimensions. . . . .</p>	10
Figure 2.2	<p>An example correlation histogram showing four key features: (1) bright spots of two co-evaporating ions; (2) horizontal and vertical lines from a single delayed evaporation; (3) curved tracks from lower left to upper right from doubly delayed evaporation; and (4) curved tracks from upper left to lower right from mid-flight dissociation. Adapted with permission from <i>Chem. Mater.</i>, 2019, 31 (7), pp 2241-2247. © 2019 American Chemical Society. . . . .</p>	15
Figure 3.1	<p>Some example molecules successfully analyzed with atom probe tomography (APT): (1) tris-(8-hydroxyquinoline)aluminum (<math>\text{Alq}_3</math>), (2) 4,4'-bis(N-carbazolyl)-1,1'-biphenyl (CBP), (3) tris[2-phenylpyridinato-C<sub>2</sub>,N]iridium(III) (<math>\text{Ir}(\text{ppy})_3</math>), (4) bis[3,5-di(9H-carbazol-9-yl)phenyl]diphenylsilane (SimCP2), (5) <math>\text{C}_{60}</math>, (6) tetracene (Tc). Adapted with permission from <i>Chem. Mater.</i>, 2019, 31 (7), pp 2241-2247. © 2019 American Chemical Society. . . . .</p>	20
Figure 3.2	<p>A SEM image of a representative Si tip used for film deposition and subsequent APT analysis. The radius of curvature at the apex is <math>\sim 500</math> nm, which is considerably larger than a typical APT sample tip. Adapted with permission from <i>Chem. Mater.</i>, 2019, 31 (7), pp 2241-2247. © 2019 American Chemical Society. . . . .</p>	23
Figure 3.3	<p>A representative detector hit map for our samples. The evaporation varies smoothly across the detector surface. Adapted with permission from <i>Chem. Mater.</i>, 2019, 31 (7), pp 2241-2247. © 2019 American Chemical Society. . . . .</p>	24

Figure 3.4	A representative voltage curve (black) and corresponding evaporation rate (red) for small-molecule organic semiconductor samples. The fluctuations in the curve are due to CAMECA's laser drift compensation algorithm for the LEAP not working effectively for our sample geometry, requiring manual laser adjustments to keep the sample properly running. Adapted with permission from <i>Chem. Mater.</i> , 2019, 31 (7), pp 2241-2247. © 2019 American Chemical Society. . . . .	25
Figure 3.5	(a) Mass spectrum of electron-irradiated C <sub>60</sub> , showing evaporation of dimers (singly ionized peaks at 1440 Da and triply ionized peaks at 480 Da; the doubly ionized peaks are subsumed in the primary C <sub>60</sub> peak) and trimers (doubly ionized peaks starting at 1080 Da) of C <sub>60</sub> . (b) Mass spectrum of unirradiated C <sub>60</sub> showing only C <sub>60</sub> peaks with no dimers or trimers. Adapted with permission from <i>Chem. Mater.</i> , 2019, 31 (7), pp 2241-2247. © 2019 American Chemical Society. . . . .	26
Figure 3.6	Mass spectrum of C <sub>60</sub> <sup>+</sup> showing isotopic peaks; the red lines are its expected isotopic distribution. Based on the peak separation shown here, this spectrum has a mass resolving power ( $m/\Delta m$ ) of about 1000 at 720 Da. Adapted with permission from <i>Chem. Mater.</i> , 2019, 31 (7), pp 2241-2247. © 2019 American Chemical Society. . . . .	28
Figure 3.7	Mass spectrum of a blended film of 6 vol % Ir(ppy) <sub>3</sub> in CBP purified by thermal gradient sublimation; (inset) Region of the impurity 4-(N-carbazolyl)biphenyl (BPC) showing a clear offset of 1 Da from the expected fragment location, while the Ir(ppy) <sub>3</sub> <sup>++</sup> peak is at its expected mass; the vertical lines in the inset show the expected isotopic positions of the impurity. Adapted with permission from <i>Chem. Mater.</i> , 2019, 31 (7), pp 2241-2247. © 2019 American Chemical Society. . . . .	29
Figure 3.8	Mass spectrum of 6 vol % Ir(ppy) <sub>3</sub> in <i>as-received</i> CBP; the impurity at 319 Da is 5 % as compared to 0.5 % in the CBP purified by thermal gradient sublimation used in the 6 vol % Ir(ppy) <sub>3</sub> :CBP blend (Figure 3.7). Adapted with permission from <i>Chem. Mater.</i> , 2019, 31 (7), pp 2241-2247. © 2019 American Chemical Society. . . . .	30
Figure 3.9	A correlation histogram of a blended film of 6 vol % Ir(ppy) <sub>3</sub> in CBP (purified by thermal gradient sublimation) focused on the CBP <sup>++</sup> peak, which shows no evidence of fragmentation of the CBP into the unexpected peaks. Adapted with permission from <i>Chem. Mater.</i> , 2019, 31 (7), pp 2241-2247. © 2019 American Chemical Society. . . . .	31

Figure 3.10	A correlation histogram of the as-received CBP focused on the CBP <sup>++</sup> peak at 242 Da, which shows no evidence of fragmentation of the CBP into the unexpected peaks. Adapted with permission from <i>Chem. Mater.</i> , 2019, 31 (7), pp 2241-2247. © 2019 American Chemical Society. . . . .	32
Figure 3.11	An x-ray diffraction (Cu-K <sub>α</sub> ) measurement of the diindenoperylene (DIP)/C <sub>60</sub> film showing it is textured with the (111) plane parallel to the substrate. Adapted with permission from <i>Chem. Mater.</i> , 2019, 31 (7), pp 2241-2247. © 2019 American Chemical Society. . . . .	33
Figure 3.12	Spatial distribution map (SDM) of C <sub>60</sub> templated on DIP showing crystal lattice planes in the z direction. The sampled volume is ~ 2600 nm <sup>3</sup> . A fit to the peaks (red) indicates the spatial resolution of this sample in the z dimension is ~ 0.3 nm. Adapted with permission from <i>Chem. Mater.</i> , 2019, 31 (7), pp 2241-2247. © 2019 American Chemical Society. . . . .	35
Figure 4.1	Mass spectra for the co-deposited (solid black) and bilayer (dotted red) samples. Major peaks are labeled with molecular species and charge state: tetracene (Tc), Diels-Alder cycloadduct (DAc), tetracene dimer (bis-Tc), and a C <sub>60</sub> with two tetracene adducts (bis-DAc); an extended list of peaks is provided in Table 4.1. In the blended sample the concentration of DAc is ~ 11 % of the total ion count, while in the bilayer sample it is only ~ 0.36 %. Even at this low concentration in the bilayer sample, the DAc peak is clearly visible. Adapted with permission from <i>Nano Lett.</i> , 2016, 16 (10), pp 6086–6091. © 2016 American Chemical Society. . . . .	38
Figure 4.2	FTIR data demonstrating a progressive increase in the intensity of the DAc vibrational mode at 700 cm <sup>-1</sup> (inset) with increasing annealing temperature for bilayer samples (Si / 50 nm Tc / 50 nm C <sub>60</sub> ); a new automatic baseline was taken from 675 to 725 cm <sup>-1</sup> for the inset. In the as-deposited film (black), the vibrational mode is indistinguishable from the noise, demonstrating the value of APT for primary species identification. Adapted with permission from <i>Nano Lett.</i> , 2016, 16 (10), pp 6086–6091. © 2016 American Chemical Society. . . . .	40
Figure 4.3	(a) Molecular concentration profile near the interface of the C <sub>60</sub> -Tc planar heterojunction. The concentration of the DAc is confined to the interface. (b) Positions of DAc (purple spheres) in the plane of the C <sub>60</sub> /Tc interface viewed from the C <sub>60</sub> side (Tc shown as teal points). There is no discernible structure to the positions of DAc in this plane. Adapted with permission from <i>Nano Lett.</i> , 2016, 16 (10), pp 6086–6091. © 2016 American Chemical Society. . . . .	42

Figure 4.4	Representative current density-voltage ( $J$ - $V$ ) curves for Tc/C <sub>60</sub> bilayer devices under 1 sun illumination (AM1.5), tested as-deposited and after annealing at 75, 100, and 125 °C for 30 min (solid lines). Equivalent devices with a 10 nm Tc:C <sub>60</sub> interlayer are also shown in dashed lines with symbols and colors that correspond to annealing conditions for the bilayer devices. The devices with the co-deposited interlayer show higher $V_{OC}$ than the bilayer devices. The increase of $V_{OC}$ with annealing temperature in all devices corresponds to an increase in the DAc as measured by FTIR. Adapted with permission from <i>Nano Lett.</i> , 2016, 16 (10), pp 6086–6091. © 2016 American Chemical Society. . . . .	43
Figure 4.5	A three-dimensional plot of the points used to generate the $K_3$ cluster analysis shown in Figure 4.6c from the perspective of the heat maps in Figure 4.6a,b. The black dots are 4,4'-bis(N-carbazolyl)-1,1'-biphenyl (CBP) while the green spheres are tris[2-phenylpyridinato-C2,N]iridium(III) (Ir(ppy) <sub>3</sub> ). There is no obvious structure to the Ir(ppy) <sub>3</sub> , but a more rigorous test ( <i>e.g.</i> $K_3$ ) is required to determine whether they are randomly distributed in the CBP matrix. Adapted with permission from <i>Chem. Mater.</i> , 2019, 31 (7), pp 2241-2247. © 2019 American Chemical Society. . . . .	46
Figure 4.6	Heat maps showing the concentration (fraction) of Ir(ppy) <sub>3</sub> in a 40 × 40 × 20 nm box projected onto (a) the x-y plane and (b) the x-z plane. Three-dimensional renderings of the volume projected are shown in Figure 4.5a,b. (c) Transformed K-function anomaly for Ir(ppy) <sub>3</sub> in this box along with simulation envelopes. The excursion of the observed K-function above the envelopes indicates significant (deviation outside a 99.9% acceptance interval) clustering of the Ir(ppy) <sub>3</sub> in the range of about 5 to 12 nm. Adapted with permission from <i>Chem. Mater.</i> , 2019, 31 (7), pp 2241-2247. © 2019 American Chemical Society. . . . .	47
Figure 4.7	(a) Mass spectra of the degradation series. The dose increases vertically. (b) The change in intensity of the mass spectra between the first and last spectrum; the grey bar cuts an artifact from taking the difference between the large main Ir(ppy) <sub>3</sub> peaks. Five peaks stand out as changing significantly between the pre- and post-exposure mass spectra: 155, 168, 643, 983, and 1310 Da. . . . .	51
Figure 4.8	(a) Change in concentration of the five species with the dose (pJ · s). Because all spectra are collected on the same sample, the pulse energy changes as dose increases as well. The concentration of the ion at 643 Da tracks closely with the concentration of tris-Ir(ppy) <sub>3</sub> . (b) Fractional change in concentration of the five species. The ion at 168 Da (red) shows odd behavior compared to the others; this can be explained by a threshold exposure energy as shown in Figure 4.10. . . . .	53

Figure 4.9	Correlation between the concentration of the tris-Ir(ppy) <sub>3</sub> <sup>++</sup> peak and the unknown ion at 643 Da. They vary in a 1:1 fashion to within the error of the fit ( $0.965 \pm 0.073$ , $R^2 = 0.962$ ), suggesting that these two ions arise from the same process. . . . .	54
Figure 4.10	Fractional change in concentration of the five species. This clarifies the different behavior of the ion at 168 Da seen in Figure 4.8: the ion only appears at a threshold pulse energy between 20 and 30 pJ. None of the other ions appear to exhibit such a threshold at the energies tested. . . . .	55
Figure 4.11	(a) MRP of the APT spectra as a function of pulse energy, calculated by gaussian fits to the primary Ir(ppy) <sub>3</sub> peak. As pulse energy decreases, MRP improves up to $\sim 1$ pJ, and is flat afterward. (b) Spectral noise versus MRP for the APT runs at different pulse energies. There is a clear trade-off between the two. . . . .	57
Figure 4.12	Change between unexposed samples analyzed at 10 pJ (black) and 1 pJ (red). The 1 pJ spectrum shows fewer peaks, though the ppy peak at 155 Da is still present at approximately the same concentration in both. . . . .	58
Figure 4.13	(a) Mass spectra of the unexposed (black) and UV exposed (red) samples. Other than the ppy peak at 155 Da, none of the other ions from the higher energy series (Figure 4.7) are apparent. The amount of ppy approximately doubles. (b) The change in intensity of the mass spectra between the first and last spectrum; only the ppy peak appears to have increased after the dose. . . . .	60
Figure 5.1	Illustration of the assignment and neighborhood definition process: (a) detector hits are binned and counted; (b) assignments are made from bins with multiple hits to bins with no hits, minimizing the total distance; (c) individual neighborhoods are defined by surrounding each assignment; and (d) overlapping neighborhoods are combined to determine the final interaction neighborhood. . . . .	66
Figure 5.2	The clusters of the input pattern viewed (a) along the axis of the cylinder and (b) from the side of the cylinder. Each cluster contains 10 points—giving them a diameter of $\sim 0.7$ nm—and they comprise 3% of the total sample. . . . .	69
Figure 5.3	Comparison of the simulated detector heat map for (a) equal evaporation fields and (b) an approximately 2:1 field difference using the same input pattern; the diameter of each heat map is 20 cm. With the field difference the heat map is considerably more mottled. . . . .	71

Figure 5.4	Comparison of the source-sink method (blue) to the standard method (red) of reconstruction using the G function; the black curve shows the input pattern, which has a much stronger clustering signal because of the absence of the field evaporation difference. The envelopes are 98 % acceptance intervals. ( <i>inset</i> ) Zoomed-in region comparing the two reconstruction methods. The clustering signal is clear in the source-sink reconstruction ( $p < 0.001$ ), while it is not significant ( $p = 0.224$ ) for the standard reconstruction (see Figure 5.5). . . . .	72
Figure 5.5	p-values based on a DCLF test (Equation 5.1) for the measured G-functions in Figure 5.4; the envelopes are 95 % confidence bands. While the standard reconstruction (red) does not show any signs of clustering ( $p = 0.224$ ), the source-sink method (blue) shows highly significant ( $p < 0.001$ ) clustering past $\sim 0.2$ nm; this matches the expected behavior based on the input pattern (black). . . . .	73
Figure 5.6	Comparison of the source-sink method (blue) to the standard method (red) of reconstruction using the K function the envelopes are 98 % acceptance intervals. While both fail to match the behavior of the input pattern (black) at large r, the source-sink method reproduces the behavior at small r much better. . . . .	75
Figure B.1	The crudely estimated evaporation fields (Table B.1) versus molecular weight. There appears to be a weak trend, but the relationship is likely obscured by temperature and pulse energy effects that are not accounted for by Equation B.2. . . . .	105
Figure B.2	The crudely estimated evaporation fields (Table B.1) versus deposition power. Similar to Figure B.1, it seems that the expected trend is mostly obscured by temperature and pulse energy effects. . . . .	106
Figure B.3	Equilibrium evaporation voltage of $\text{Ir}(\text{ppy})_3$ versus laser pulse energy. Fitting with Equation B.4 gives $C\alpha\delta = 262 \pm 16 \text{ kV J}^{-1}$ and $Ck_B T + V_E = 7.764 \pm 0.071 \text{ kV}$ with $R^2 = 0.96$ . Simply using the intercept of this fit gives an estimate of $F_E = 7.1 \text{ V nm}^{-1}$ for $\text{Ir}(\text{ppy})_3$ . . . . .	110
Figure B.4	The estimated evaporation fields (Table B.2) versus molecular weight. The trend that was somewhat apparent in the basic field evaporation estimates (Figure B.1) is much clearer. . . . .	112
Figure B.5	The estimated evaporation fields (Table B.2) versus deposition power. The trend that was somewhat apparent in the basic field evaporation estimates (Figure B.2) is much clearer. . . . .	113

## LIST OF TABLES

Table 3.1	A table of evaporation parameters for a variety of materials that we have successfully run in the atom probe. The tip radii are nominal values; the stars indicate that the tip was made from W instead of Si, and have a larger uncertainty in their radius because of their fabrication process. The “turn-on” voltage was estimated from the voltage at which the species first became apparent in the mass spectrum. . . . .	21
Table 4.1	Masses and associated compounds for the APT mass spectrum shown in Figure 4.1, where bis-Tc is a covalently bonded Tc dimer, C <sub>120</sub> -DAc is a covalent dimer of C <sub>60</sub> with a single Tc adduct, and bis-DAc is a C <sub>60</sub> with two Tc adducts. . . . .	39
Table 4.2	The doses applied for the UV degradation series. Each exposure was performed under minimal bias ( <i>i.e.</i> 500 V, the minimum voltage for operating the LEAP) at 10 MHz. . . . .	50
Table B.1	A table evaporation fields based on the evaporation parameters in Table 3.1. The fields are calculated solely based on Equation B.2, and do not account for the pulse energy or sample temperature. . . . .	104
Table B.2	The estimated fields based on Table 3.1 accounting for the temperature and laser pulse energy, assuming a uniform heat capacity of $C_p = 50 \text{ J K}^{-1} \text{ mol}^{-1}$ in the estimate of $\delta$ in Equation B.5; the values for CBP and mCBP are the same because they were used together to fulfill the two measurement requirement. The estimated error is $\pm 1 \text{ V nm}^{-1}$ . . .	112

## ACKNOWLEDGMENTS

My adviser, Dr. Jeramy D. Zimmerman, has been a great research partner and mentor. Since before I was officially accepted at Mines, I have enjoyed our lengthy and wide-ranging conversations about research and science; our first, hours-long discussion in January of 2014 created the nucleation site for what would become this dissertation. His insight and encouragement pushed me to become a better scientist. I continue to be impressed by his dedication, hard work, and expert command of knowledge in the field. The best parts of this work are a reflection of his abilities as a mentor.

Matthew B. Jaskot has been an invaluable part of my research; this dissertation would have taken years longer to complete without his assistance in the lab. In particular, I would like to thank him for the data shown in Figure 4.4 that ties together the complete picture of the structure-property relationship described in Proudian et al. [1]

Christelle Lyiza helped bolster my understanding of organic chemistry as I learned more about the field of organic electronics. The FTIR data shown in Figure 4.2 were collected by her and helped confirm the presence of the chemical reaction observed with APT in our paper together.[1]

Galen Vincent has done an outstanding job furthering the work of analyzing atom probe data with spatial statistics. It has been a real pleasure working with him to develop new tools and methods of analysis. I look forward to his success in future endeavors.

Dr. David R. Diercks has consistently been a wealth of expertise for all things atom probe. His assistance with a myriad of technical tasks made my research significantly easier, and many ideas arose from fruitful conversations with him during our work together.

My dissertation committee, comprised of the aforementioned Dr. Zimmerman and Dr. Diercks, along with Dr. Brian P. Gorman, Dr. Reuben T. Collins, and Dr. Alan Sellinger, was a great resource as I carried out my research. Their varied expertise and viewpoints

helped me refine my work and enhanced the quality of this dissertation.

Beyond my professional relationships, I am grateful to my community of family and friends that have supported me throughout this journey. At Mines, the friendships I built in the Physics Department, Graduate Student Government, and the Harmonic Miners made me a part of the Mines community. Outside of campus, friends and family alike provided necessary respites and reality-checks that helped sustain me through this endeavor.

Finally, I cannot express the depth of my gratitude for the love and support of my wife, Dr. Megan A. Danielewicz. Throughout this process, she has always been with me, as both companion, scientist, and confidante. I hope that this dissertation in some small way reflects the degree to which she inspires me on a daily basis.

For Megan.

# CHAPTER 1

## INTRODUCTION

*We need methods to map the internal three-dimensional (3D) structure and to correlate this with device performance.*

–Jørgensen et al. [2]

Modern electronics now include a wide variety of organic devices, such as organic photovoltaics (OPVs), organic thin-film transistors (OTFTs), and organic light-emitting diodes (OLEDs). Compared to their inorganic counterparts, organic electronic devices enjoy a number of advantages, including low-cost room-temperature deposition, easy patterning at relevant length scales (*e.g.* display pixels), mechanical flexibility, and application-specific tunability; the broad commercial success of OLEDs in the past few years provides a clear example of this.[3] However, to fully realize these advantages requires more detailed knowledge of the structure-property relationships of these devices. As we will show, atom probe tomography (APT) is a valuable tool for driving our knowledge of these molecular systems.

The fundamental physics of inorganic semiconductors has been well-established for over half a century, though engineering challenges remain. In contrast, there are still many developments to be made in the fundamental physics of organic semiconducting materials.[4–6] A major difference for organic electronics—which makes them more difficult to describe theoretically—is the strong influence of small changes to morphology on device performance and reliability.[4, 7, 8] Many methods have been explored to determine how microstructure changes with material, deposition, and processing conditions;[2, 6, 8–16] in addition, morphological changes and molecular degradation impact the performance and lifetime of these devices.[10, 17–23] These studies have led to improvements in performance, but have largely been driven by empirical investigation rather than material theory.[2, 8, 9] Improved

structural characterizations of these devices in three dimensions will lead to better physical theories of organic electronics, shortening development times.[2, 7–9, 24–26]

Because their properties are strongly dependent on morphology, organic films require detailed nanoscale characterization.[8, 25] For inorganic systems, a wide variety of tools are available for high-resolution imaging and tomography.[27] Unfortunately, many of the techniques are challenging to apply to organic systems, as they are sensitive to ion, electron, and X-ray irradiation, and many techniques are hampered by weak scattering contrast between materials.[24, 25, 28–31] This does not rule out these techniques, but limits the kind and quality of data they can yield.

The first major class of techniques that have been employed to ascertain morphology in organic semiconductors are transmission electron microscopy (TEM) and its derivatives, including high-angle annular dark field scanning TEM (HAADF-STEM), and energy-filtered TEM (EF-TEM).[2, 7, 25, 26, 30, 32, 33] TEM has enabled ground-breaking studies of organic nanostructures because of its excellent spatial resolution—with some instruments capable of resolving sub-nanometer features—which greatly contributed to the development of organic electronic devices.[8, 24, 25] Unfortunately, difficulty with contrast in these systems can make it challenging to definitively identify composition.[24, 25, 29] Bright-field TEM requires defocusing to create material contrast, which can change the apparent size of features, cause contrast reversals, and lead to quantitative analysis errors.[26] EF-TEM or electron energy-loss spectroscopy (EELS) can help with this issue by using energy loss spectra to discriminate materials using a specific element or other spectroscopic signatures.[24–26, 29] However, the spectral response depends on the structure of the sample in addition to its composition, complicating species assignment.[29] HAADF-STEM can also improve contrast by looking at high-angle scattered electrons, which depend on the average atomic number, but the reduced electron count leads to a trade-off between signal-to-noise ratio and imaging time (and consequent sample damage).[25, 26] For fullerene systems, endohedral fullerenes have been substituted to increase contrast further, allowing measurement of, *e.g.*, phase purity;

however, these systems do not directly reproduce the original system because of changes to the solubility of the endohedral fullerene as compared to the original system.[26] Even in native systems with high contrast—such as cyclometallated compounds—it is challenging to determine the three-dimensional structure based on a two-dimensional projection.[8, 32] Electron tomography can overcome this limitation, giving full three-dimensional information; unfortunately, the increased beam exposure due to imaging at many angles exacerbates the material degradation problem of electron microscopy techniques.[8, 24, 25] Because of the changes in contrast between the different TEM methods and different sample preparations (*e.g.* sample thickness), comparing and interpreting different results can be challenging.[8, 25]

Scattering methods are also a common tool for probing organic film structure, and have been instrumental in developing our understanding of organic morphologies; but, due to the low scattering contrast or requirement for a tunable source, they must often be performed at beamlines or user facilities.[2, 12, 30, 33] X-ray reflectometry (XRR) measures layer thickness and roughness, including at buried interfaces, making it a great tool for examining interfacial changes and abruptness; however, it provides no chemical identification.[2, 12] Grazing incidence measurements, such as grazing incidence X-ray diffraction (GIXD) and grazing incidence wide-angle X-ray scattering (GIWAXS), probe three-dimensional morphology, but the former only images crystalline regions and the latter cannot probe the full three-dimensional space of the sample.[12, 25, 30, 33] Neutron reflectometry (NR) can measure thicknesses down to a nanometer and is more sensitive to material composition than X-rays, but generally requires deuteration of one organic species.[10, 24, 34] Resonant soft X-ray scattering (RSoXS) can examine lateral structures with a thickness of a few nanometers even at buried interfaces, and has higher scattering intensity than hard X-rays through careful selection of the photon energy.[8, 24, 33] Scattering methods generally require model fits to interpret the data that are not necessarily unique, but this can be mitigated by using reference materials to provide phase data (*e.g.* phase-sensitive NR).[8, 24]

A variety of other methods have been used to probe nanostructure as well, but these often only provide information within a limited parameter space. One of the most common methods for investigating surfaces is atomic force microscopy (AFM), which can characterize surface roughness down to a few nanometers.[2, 7, 10, 12, 24, 25, 33, 35, 36] Near-field scanning photocurrent microscopy (NSPM) allows correlation of the surface morphology with photoresponse.[24, 25, 37] Complementary to this are various optical techniques—such as UV–vis/IR spectroscopy or spectroscopic ellipsometry—which can image into the bulk of the material but spatially average the information.[2, 8, 17] X-ray photoelectron spectroscopy (XPS) and ultraviolet photoelectron spectroscopy (UPS) can quantitatively identify chemical elements and shifts within  $\sim 5$  nm of the surface, but they have a lateral resolution limit of  $\sim 30$   $\mu\text{m}$  and cannot identify molecular species.[2] Similarly, near edge X-ray absorption fine structure (NEXAFS) spectroscopy is surface sensitive within  $\sim 2$  nm and has a lateral resolution of 10 to 100 nm with the same elemental sensitivity; interpreting this information, however, strongly depends on the interaction model used.[8, 24, 25] Time-of-flight secondary ion mass spectrometry (TOF-SIMS) and dynamic SIMS (DSIMS) provide a three-dimensional spatially-resolved chemical profile; however, their lateral resolution is  $\sim 50$  nm—much larger than many morphological features—and the depth resolution from sputtering often must be correlated with a second measurement such as *in-situ* AFM.[2, 8, 16, 24, 36] Furthermore, because the material is sputtered, it generally creates fragments that make interpreting the resultant mass spectrum more difficult, and can have differences in sputtering efficiency for different materials.[24, 38] Even with these limitations, SIMS is closest to a single measurement of chemical and morphological information that is widely used by the community, but still cannot answer many questions about system morphology because of its limited spatial resolution and fragmentation of molecular species.

The immense effort to develop and adopt new tools has enabled innumerable advances in the field, but many questions remain that are difficult to explore with existing techniques. Existing imaging techniques generally have insufficient resolution or chemical contrast to

characterize the nanostructure of the material at adequate levels to inform better physical theories of organic electronics; measurements typically provide either high spatial resolution or sensitive chemical information—but rarely both—requiring indirect correlation of information from several different techniques.[24, 25]

APT, which combines both high spatial resolution ( $< 1$  nm) and high analytical sensitivity ( $< 100$  ppm) in a comparatively large volume ( $> 10^7$  nm<sup>3</sup>), simultaneously measures chemical and spatial information with high precision.[39, 40] This ability can help provide the structural information needed to propel the next generation of physical theories for organic electronics.

In APT, a sample prepared with a sub-micrometer radius of curvature is held at cryogenic temperatures in ultra high vacuum (UHV) under high bias, generating a large local electric field. A voltage or laser pulse of adequate intensity causes an atom or molecule on the surface to field evaporate. The electric field accelerates this ion towards a two-dimensional position- and time-sensitive detector; we note that, while the efficiency of this detector is not unity, it can be up to 80% in new instruments,[41] which is quite high for any ion counting technique.[42] This process repeats until the desired thickness of sample has evaporated. The time-of-flight of each ion gives its mass-to-charge ratio, and its position on the detector allows the ion's location to be reconstructed in three dimensions.[39, 40, 43]

Despite APT's excellent spatial and chemical resolution and the relative maturity of the technique, the body of APT analyses of organic systems is small.[44–52] Most of these studies looked at polymers, which, because of their chain structure, fragment during field evaporation.[48–52] In 2012, Joester et al. examined a blend of poly(3-hexylthiophene-2,5-diyl) (P3HT) and C<sub>60</sub>.<sup>[52]</sup> As before, the P3HT polymer proved difficult to study due to uneven fragmentation, but the mass-spectrum had a clear C<sub>60</sub> signal, suggesting that small-molecule organic systems should be amenable to study with APT; this can be understood by considering that the strength of the intra-molecular (covalent) bonds in small-molecule organics is roughly 2-4 times that of the inter-molecular (van der Waals) bonds.<sup>[53]</sup>

This dissertation follows through on this supposition, developing APT for small-molecule organic semiconducting systems. It is organized as follows: Chapter 2 introduces the necessary background information from organic electronics, atom probe microscopy, and spatial statistics that underpins the rest of the work; Chapter 3 describes the work done to validate APT in molecular organic systems; Chapter 4 discusses the scientific advances that have been enabled by developing APT for small-molecule organic semiconductors; Chapter 5 describes a new method of reconstructing APT data that accounts for uncertainties in the reconstruction process; and Chapter 6 provides important conclusions and suggests directions for future inquiries. Throughout, this work draws upon Proudian et al. [1] and especially Proudian et al. [54]; figure attribution is noted where appropriate.

## CHAPTER 2

### BACKGROUND

*Begin at the beginning and go on till you come to the end; then stop.*

–Lewis Carroll

There are three main topics that comprise this dissertation: organic electronics, atom probe tomography (APT), and spatial statistics. As each of these are necessary to form a complete understanding of this work, the salient portions of each topic are covered below.

#### **2.1 Organic Electronics**

Organic electronic materials, as a rule, contain  $\pi$  bonds that allow for delocalized electron densities within the molecule. The energy of these  $\pi$  bonds give these molecules absorption and emission spectra around the visible range. Furthermore, through the ingenuity of synthetic organic chemists, these spectra can be tuned through changes to molecular structure.[55]

The nature of these intramolecular bonds means that the intermolecular forces are generally weak, van der Waals forces. This means that solids composed of these molecules retain their individual molecular properties to a larger extent compared to other solids. However, the properties of these solids are complex, allowing for wide variation with relatively minor changes in the chemistry of the constituent molecule. This makes them challenging but fascinating objects of study for the physicist seeking to describe their behavior, and there are still many developments to be made in the fundamental physics of organic semiconducting materials.[4–6]

The motivation to study these materials is practical as well as academic. A variety of devices have been developed using organic materials. Of these devices, organic light-emitting diodes (OLEDs) are the most commercially successful. Electroluminescence of

organic materials has been observed since the 1960s,[56] and the first device above 1% efficiency was demonstrated by Tang and Vanslyke in 1987;[57] however, the efficiency of these fluorescent devices were limited because of spin statistics because the singlet state corresponding to fluorescence accounts for only 25% of the radiative exciton relaxation pathways. In many systems, radiative triplet states are not readily accessible because the ground state is spin anti-symmetric, meaning 75% of the generated excitons are lost off the top to non-radiative processes.[58] The commercial success of OLEDs did not come until the development of phosphorescent systems that circumvented this efficiency restriction by introducing a molecule with strong spin-orbit coupling that leads to intersystem crossing (ISC).[59]

Triplet states can become radiative by applying a perturbation that permits triplet-singlet transfer. For this reason, Baldo et al. designed a system with strong ISC that permits access to the triplet state, with correspondingly higher device efficiencies.[59] This is done via spin-orbit coupling: by creating a heavy-metal complex, a metal-ligand mixed state arises which has some ligand character.[60] Baldo et al. chose platinum and iridium complexes to achieve this because they have sufficiently short phosphorescent lifetimes, allowing device applications (*i.e.* 1 to 10  $\mu$ s).[61] In these systems, the emissive layer is composed of at least two parts—a minority guest phosphorescent molecule and a majority host.

The lifetime of the phosphorescent excited state in these OLED systems is still considerably longer than the fluorescent state, causing a correspondingly higher exciton density at a given brightness; this means that exciton quenching processes are important when considering efficiency, particularly triplet-triplet annihilation (TTA) and triplet-polaron quenching (TPQ).[61] TTA occurs when two triplet excitons interact on the same molecule creating a higher energy exciton which thermally relaxes back to a singly-excited triplet state, removing an exciton. TPQ occurs when a triplet exciton and a polaron interact on a molecule to cause the exciton to non-radiatively decay. These quenching processes can also lead to degradation through the energy released into the molecule during the decay of the exciton.[62]

## 2.2 Atom Probe Tomography

APT is a technique that has its origins in the field emission electron microscope nearly 100 years ago.[63] The first atom probe was developed in 1968; it was one-dimensional and only applicable to metals.[64, 65] However, since then its utility has greatly expanded to include a wide variety of materials characterized in three dimensions.[66]

APT is based on a process called field evaporation, wherein an atom or molecule is ionized from the surface of a sample by the application of a large electric field ( $\sim 10 \text{ V nm}^{-1}$ ). The details of this process are as follows:[65]

1. The sample is prepared with a small radius of curvature ( $< 1 \mu\text{m}$ ) and cooled to cryogenic temperatures ( $< 50 \text{ K}$ ) under ultra high vacuum (UHV) ( $< 5 \times 10^{-10} \text{ Torr}$ ).
2. The sample is placed under a large bias (1 to 9 kV), which, due to the small radius of curvature of the sample (50 to 500 nm), creates an electric field of between 1 to  $50 \text{ V nm}^{-1}$ .
3. The sample is subjected to a voltage or laser pulse that brings the atoms or molecules at its surface briefly (100 to 400 ps) to a state of high ionization probability. Some small fraction of these pulses (0.1 to 3%) lead to an atom or molecule being ionized.
4. The generated ion is rapidly accelerated from the surface by the electric field. Typically, this is assumed to happen within a very short distance from the sample surface, so that the acceleration may be treated as instantaneous.
5. After traveling for a period of time (0.3 to 8  $\mu\text{s}$ ), the ion impacts a two-dimensional time- and position-sensitive detector.
6. The process repeats until the desired volume of the sample has been analyzed.

A schematic of this process is given in Figure 2.1. Through a reconstruction process, the sample can be rendered in three-dimensions with a time-of-flight (TOF) mass-to-charge ratio for every detected ion.

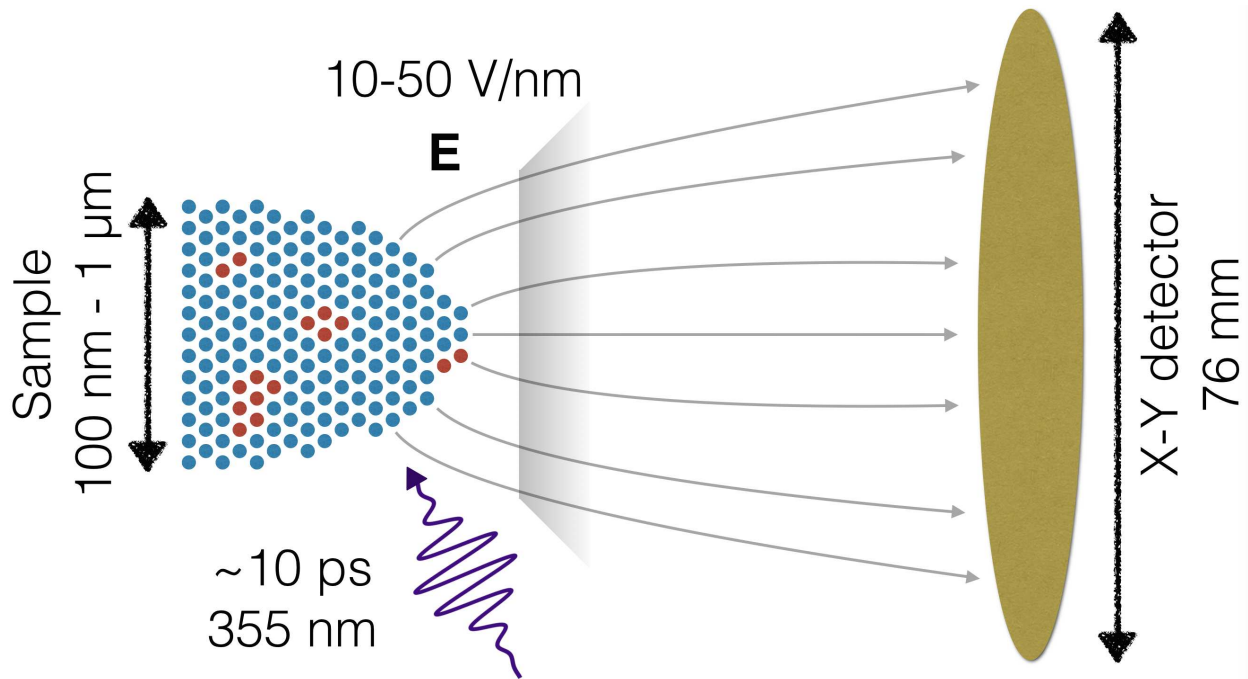


Figure 2.1: A schematic of the atom probe tomography (APT) process: A sample prepared with a sub-micrometer radius of curvature is held at cryogenic temperatures in UHV under high bias, generating a large local electric field. A voltage or laser pulse of adequate intensity causes an atom or molecule on the surface to field evaporate. The electric field accelerates this ion towards a two-dimensional position- and time-sensitive detector. This process repeats until the desired thickness of sample has evaporated. The time-of-flight of each ion gives its mass-to-charge ratio, and its position on the detector and sequence of detection allows the ion's location to be reconstructed in three dimensions.[54]

Within this dissertation, we use the CAMECA Local Electrode Atom Probe<sup>TM</sup> 4000X Si (LEAP). This instrument uses a local electrode, which allows a smaller bias to be applied to create the same electric field at the sample surface.

Operation of the LEAP requires the user to select a number of run-time parameters:[65]

- Base temperature
- Analysis type (voltage or laser pulse)
- Pulse repetition rate
- Pulse fraction (voltage) or pulse energy (laser)
- Detection rate, which is the fraction of ions detected per pulse

For organic materials, to achieve evaporation in the middle of the voltage range (3 to 7 kV), these are typically:

- Base temperature (set-point): 25 K
- Analysis type: laser
- Pulse repetition rate: 250 kHz
- Pulse energy: 10 pJ
- Detection rate: 1 ion per 100 pulses

Reconstruction is performed using CAMECA's integrated visualization and analysis software (IVAS) (3.6.14), which follows the method proposed by Bas et al..[43] The general procedure is as follows:[65]

1. Select a continuous voltage range to reconstruct.
2. Select an elliptical area on the detector to reconstruct.
3. Correct the TOF with voltage and bowl corrections; the voltage correction accounts for the TOF difference due to changes in the accelerating voltage, while the bowl correction corrects for TOF differences across the sample surface due to the sample shape.
4. Adjust the mass spectral peak positions to align known peaks.
5. Assign labels and volumes to peaks in the mass spectrum

6. Reconstruct the hit positions using a set of reconstruction parameters and voltage, shank angle, or tip profile evolution.

The free parameters of the reconstruction are:[65]

- The image compression factor (ICF), which characterizes the deviation of ion trajectories from sample surface normal projections
- The tip radius ( $R$ )
- The field factor ( $k_f$ ), which accounts for the influence of the tip shape on the electric field
- The volume of the ion ( $V$ )
- The detection efficiency ( $\eta$ )

In addition, there are three choices of reconstruction evolution methods that estimate the change in tip radius throughout the run:[65]

**Voltage** Use the change in voltage.

**Shank Angle** Use the shank angle of the tip.

**Tip Profile** Use a scanning electron microscopy (SEM) or transmission electron microscopy (TEM) image of the tip to define radii through the sample; the radius is then interpolated between these defined locations.

For our samples, these are typically:

- Voltage evolution
- ICF: 1.6
- $R$ : 200 to 500 nm
- $k_f$ : 3.3
- $V$ : 0.3 to 1.2 nm<sup>3</sup>
- $\eta$ : 0.55

Primary analysis of APT data relies on four values:  $(x, y, z)$  coordinates of the particle in the reconstructed space, and the mass-to-charge state of the ion. This, however, is not all the information that is in the data, and other information can be helpful in extracting more information. APT data contains much more information than simply the reconstructed  $(x, y, z)$  position and mass-to-charge-state ratio. They also contain fields for the detector  $(X, Y)$  position and TOF, along with the pulse index of the event and the specimen voltage.[65]

With advances in APT instrumentation, volumes of  $200 \text{ nm} \times 200 \text{ nm} \times 1000 \text{ nm}$  can be analyzed, with data sets containing upwards of  $10^8$  events.[66] This makes analyzing APT data difficult because of the sheer volume of data, even just considering event locations;[67] if the large numbers of marks (*e.g.* mass-to-charge ratio and multiple detection events (MDEs)) are incorporated, the standard computational methods of spatial statistics become prohibitive for efficient analysis;[68] however, the richness of information that can be gleaned from the ancillary data should not be overlooked, as it provides critical insights into the material under study.[69–71]

Knowing the  $(X, Y)$  location of an ion’s impact on the detector can be valuable for a few reasons. First, it allows for the estimation of the field-of-view (FOV) in crystalline samples where zone axes can be observed.[72] Second, it allows for analysis of two-dimensional hit correlations, which is a more developed area of spatial statistics (see below).[73] These data have recently been used to aid in extracting crystallographic information, suggesting other avenues for enhanced analysis.[74] Finally, it permits alternative reconstruction methods from those provided above; an alternative method for reconstruction using this information will be described in Chapter 5.

The assumption of single evaporation events is an idealization, as often MDEs are observed in a single pulse.[75] This has become less problematic as detector technology has improved—allowing for better collection of MDEs—but still remains an issue for the reconstruction.[76] Furthermore, while the rate of single events matches a Poisson distribution based on the overall detection rate, the frequency of MDEs is relatively insensitive to the

total event detection rate and has a much heavier tail than one would expect from a Poisson process.[77] Some in the field have suggested that the rate of MDEs is tied to the material under study, and the atom probe community has recently recognized the importance of fully characterizing MDEs to improve the quality of APT analysis.[71, 75–77]

Correlation histograms of events when two ions are detected for a single laser pulse were proposed by Saxey to aid in mass spectrum analysis for APT.[76] They plot the masses ( $i$  &  $j$ ) of each detection event against each other and then bin these data to examine occurrence frequencies; as a result, they are symmetric about  $i = j$ .

An example correlation histogram is shown in Figure 2.2. There are four key features that are visible in these correlation histograms. First are the expected bright spots at coincidences between major peaks  $i$  and  $j$  representing the field evaporation of two ions. More interesting are the three types of lines that emanate from these points. Horizontal and vertical lines are due to the delayed evaporation of one ion of the pair. Curved tracks that go from low  $i$  and  $j$  (lower left) to high  $i$  and  $j$  (upper right) are the result of delayed evaporation for both ions. Finally, tracks that go from upper left to lower right are due to mid-flight dissociation of the parent ion, which are of interest when investigating possible molecular fragmentation.

Preliminary analysis of APT is done using the tools within CAMECA’s IVAS. This provides basic visualization of the reconstructed volume, along with tools for analyzing spatial concentrations and species distributions. These tools, however, are relatively rudimentary, and must be supplemented with more advanced analysis techniques.

In this dissertation, this analysis is performed in R, in which numerous libraries exist for analysis of all aspects of APT data. We have written a library—`rapt`—to collect, extend, and supplement the capabilities of current R packages. It allows for the importation of data created by IVAS, mass spectral and spatial analysis, simulation, and visualization. It is available freely at <https://github.com/aproudian2/rapt>.

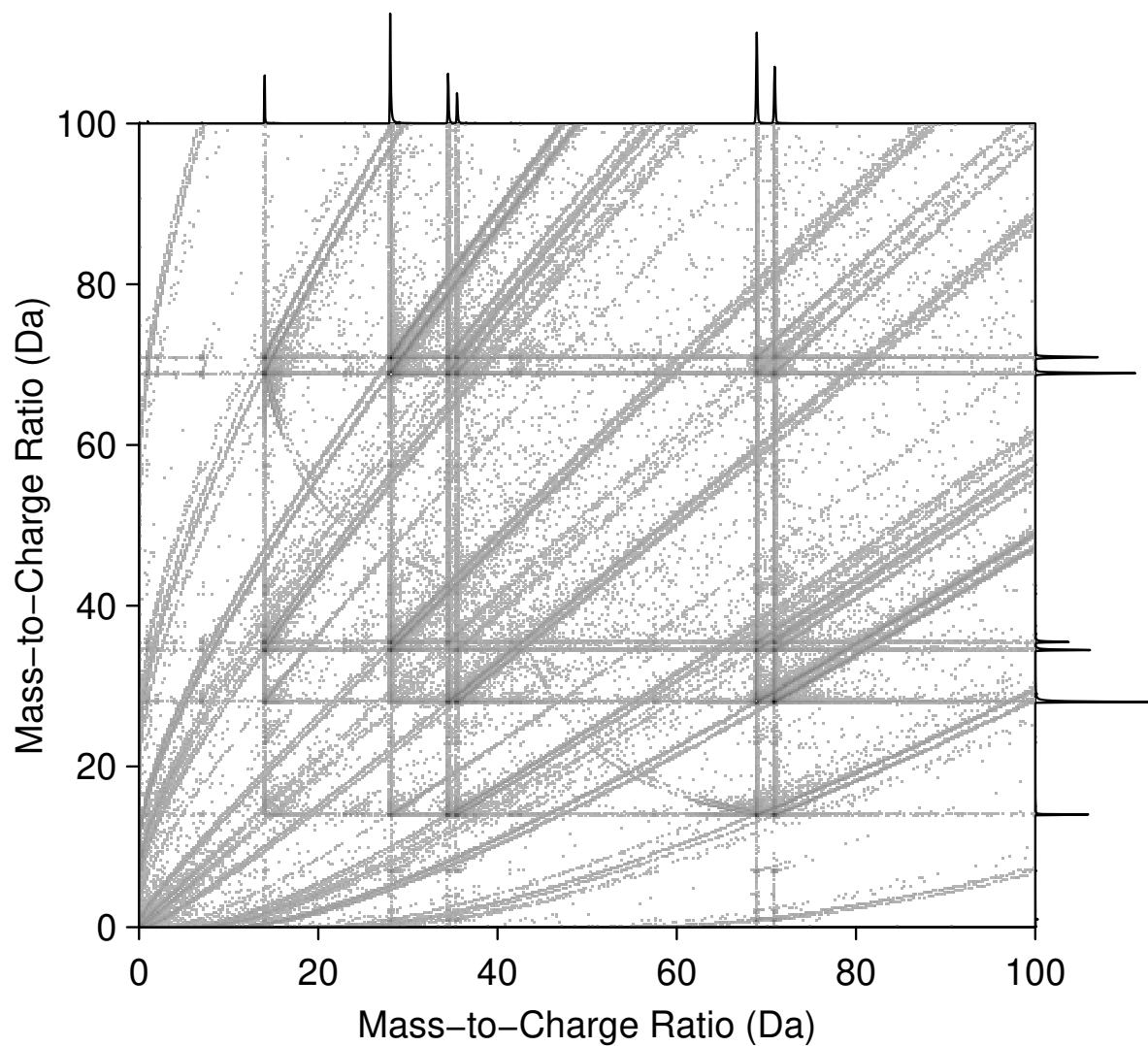


Figure 2.2: An example correlation histogram showing four key features: (1) bright spots of two co-evaporating ions; (2) horizontal and vertical lines from a single delayed evaporation; (3) curved tracks from lower left to upper right from doubly delayed evaporation; and (4) curved tracks from upper left to lower right from mid-flight dissociation. Adapted with permission from *Chem. Mater.*, 2019, **31** (7), pp 2241-2247.[54] © 2019 American Chemical Society.

## 2.3 Spatial Statistics

An important part of characterizing APT data is understanding the significance of what has been observed. However, because the large volume of data generated ( $> 10^6$  Ions), accomplishing this requires us to extract a summary of the data that is easy to interpret; this analysis toolset is called spatial statistics, specifically the branch related to point patterns.[78]

In its most basic form, a spatial point pattern is a set of locations distributed within a region. The interest of the spatial statistician is to characterize the distribution of these points. This is done in a variety of ways that provide a complementary set of tools to analyze point patterns; some of the most common are:[79]

### **G-Function**

The  $G$ -function measures the number of nearest neighbor points contained within a sphere of radius  $r$  centered about each point of the pattern, normalized by the point pattern intensity (*i.e.* the average number of events per unit volume). It is estimated by:

$$\hat{G}(r) = \sum_i I(r_i \leq r)/n \quad (2.1)$$

where  $I$  is the indicator function and  $n$  is the number of points in the pattern. This definition makes  $G(r)$  a cumulative distribution function of nearest neighbor distances.

### **F-Function**

The  $F$ -function measures the number of nearest points contained within a sphere of radius  $r$  centered about an independent set of sampling locations, normalized by the point pattern intensity. It is estimated by:

$$\hat{F}(r) = \sum_i I(r_i \leq r)/n \quad (2.2)$$

### **J-Function**

The  $J$ -function is a derived quantity that is an unbiased estimator of observed clustering and inhibition. It is defined as:

$$J(r) = \frac{1 - G(r)}{1 - F(r)} \quad (2.3)$$

### **K-Function**

The  $K$ -function measures the number of additional points contained within a sphere of radius  $r$  centered about each point of the pattern, normalized by the point pattern intensity. It is estimated by:

$$\hat{K}(r) = \lambda^{-1} \sum_{i \neq j} I(r_{ij} < r) / n \quad (2.4)$$

where  $\lambda$  is the pattern intensity, defined by:

$$\lambda = \frac{n}{D} \quad (2.5)$$

where  $n$  is the number of points in the pattern and  $D$  is generalized volume of the point pattern's domain.

### **Pair Correlation Function / Radial Distribution Function**

The pair correlation function (also called the radial distribution function) is a derived quantity that highlights changes in spatial behavior. It is defined as:

$$g(r) = \frac{K'(r)}{2\pi r} \quad (2.6)$$

Because this definition involves a derivative, care must be taken in dealing with the resultant noise and required smoothing when estimating the pair correlation function from observed data.

In addition to point locations, points can have other data associated with them, called marks. There are two types of marks: categorical and continuous. Categorical marks are discrete labels applied to the data, which classify them into one of a finite set of categories, while continuous marks are a range of values. Continuous marks can be turned into categorical marks through the use of binning. This is how we treat APT data, converting the continuous mark of mass-to-charge ratio to a categorical mark of molecular species.

Cross-functions are defined similarly to their unmarked counterparts, but look at the relationship between points of (categorical) mark types  $A$  and  $B$ . These are useful for examining cross-correlations (*e.g.* what is the distribution of one molecule in relation to another?). Each function can also be used to only look at a single type of mark relative to the whole pattern (the so-called “dot” functions) or to itself (*e.g.* a cross-function of  $A$  to  $A$ ).

To characterize the observed measure (*e.g.*  $K$ -function), there must be a way to test it against a hypothesis. The first test is to determine whether the pattern deviates from randomness. For a categorically marked point pattern, we can also test the random labeling hypothesis. This focuses on the distribution of marks on the points without regard to the underlying point positions, and tests whether the marks deviate from that expected from the random assignment of labels. This can be useful if the point positions are known to have some non-random structure, but the distribution is unknown (*e.g.* an atom probe reconstruction).

Beyond this test, there are many models that have been developed for testing various distribution hypotheses. These permit us to move beyond simply rejecting randomness and selecting a probable model of behavior with physical parameter estimates.[79] Commonly, there is no analytic expression for these functions given a particular distribution of points or marks. In this case, selecting a model for the observed point pattern is done *via* simulation. `rapt` has a number of functions implemented for this purpose.

The majority of the spatial analysis in this dissertation is performed using the `spatstat` package in R or extensions implemented in the `rapt` package. `spatstat` has full open-source documentation at `spatstat.org`, and its author wrote a book detailing its use in analyzing spatial point pattern data.[73] Extensions to `spatstat` are primarily to accommodate three dimensional data as most work on point patterns has been in two dimensions. By creating `rapt`, we have helped bring together the fields of APT and spatial statistics, which are a natural fit.

## CHAPTER 3

### VALIDATION

*There is substantial need for techniques that can resolve the distribution of the different carbonaceous components with chemical sensitivity on the nanoscale.*

Schindler et al. [29]

As stated in Chapter 1, the volume of work studying small-molecule organic semiconducting materials using atom probe tomography (APT) is very small. Therefore, it is critical to determine rough parameters for using APT (*e.g.* sample preparation, laser energies) and demonstrate how the technique performs on these materials (*i.e.* mass and spatial resolution).

**The following discussion draws heavily from Proudian et al. [54].**

Organic molecular materials span a wide range of structures, bond types, masses, and atomic constituents. This variety makes organic electronics very versatile, but presents a challenge when trying to generalize their properties. We have successfully analyzed a number of materials systems with APT that represent a reasonable cross-section of common organic electronic molecules, including organometallics such as tris-(8-hydroxyquinoline)aluminum ( $\text{Alq}_3$ ) and tris[2-phenylpyridinato-C<sub>2</sub>,N]iridium(III) ( $\text{Ir}(\text{ppy})_3$ ), fullerenes, tetracene (Tc), and polycyclic aromatics such as 4,4'-bis(N-carbazolyl)-1,1'-biphenyl (CBP) and bis[3,5-di(9H-carbazol-9-yl)phenyl]diphenylsilane (SimCP2) as shown in Figure 3.1; other materials we have successfully run include bathophenanthroline (BPhen), diindenoperylene (DIP), and 4-(dicyanomethylene)-2-methyl-6-julolidyl-9-enyl-4H-pyran (DCM2). Table 3.1 provides information on various materials and their analysis parameters; B explores possible evaporation fields for these materials.

Because of the sensitivity of organic films to electron radiation, we deposit films directly on a curved Si or W tip rather than using the standard practice of cutting them out from a flat film using a focused ion beam.[39] The low evaporation field of molecular organic

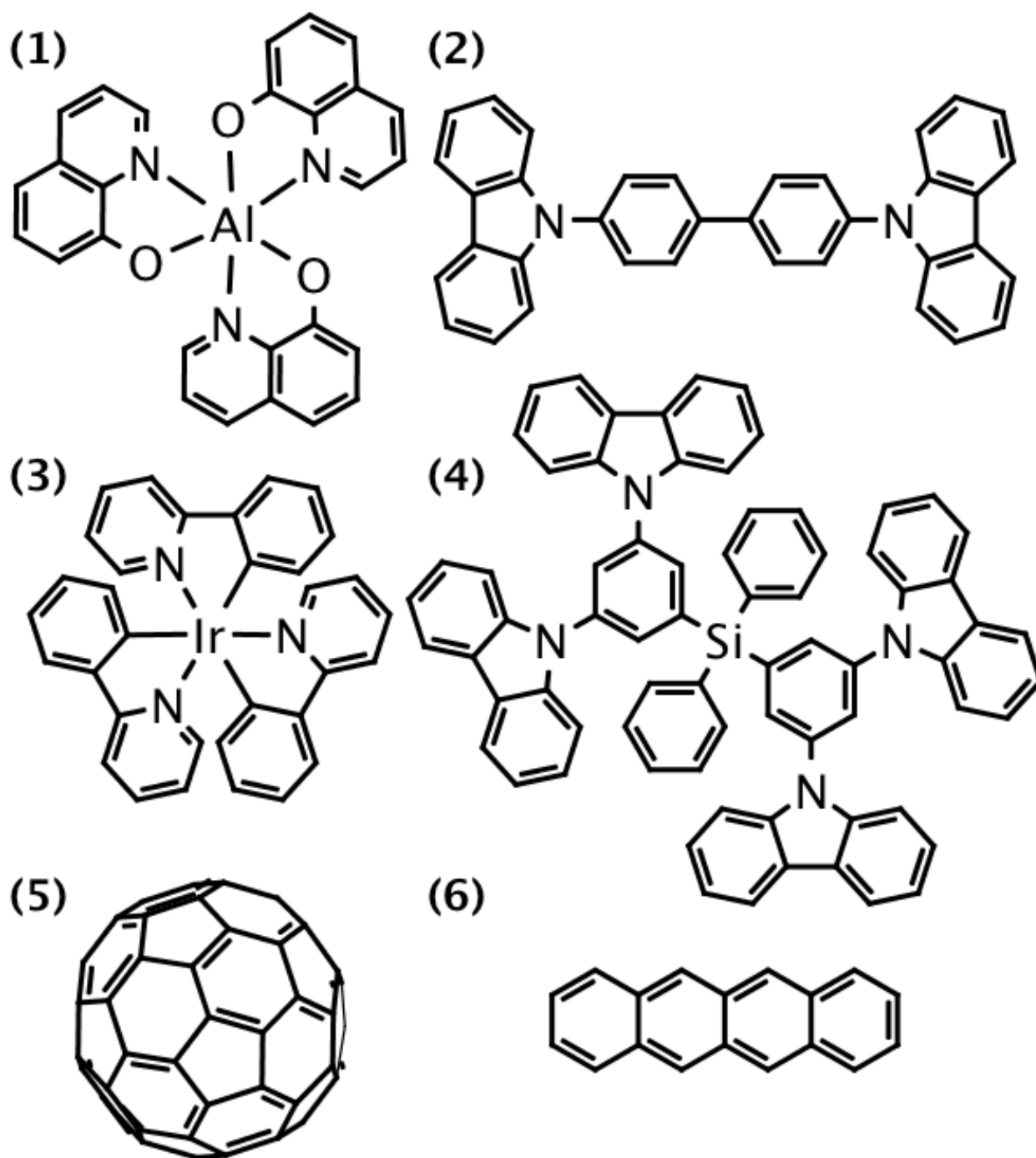


Figure 3.1: Some example molecules successfully analyzed with atom probe tomography (APT): (1) tris-(8-hydroxyquinoline)aluminum ( $\text{Alq}_3$ ), (2) 4,4'-bis(N-carbazolyl)-1,1'-biphenyl (CBP), (3) tris[2-phenylpyridinato-C2,N]iridium(III) ( $\text{Ir}(\text{ppy})_3$ ), (4) bis[3,5-di(9H-carbazol-9-yl)phenyl]diphenylsilane (SimCP2), (5)  $\text{C}_{60}$ , (6) tetracene (Tc). Adapted with permission from *Chem. Mater.*, 2019, **31** (7), pp 2241-2247.[54] © 2019 American Chemical Society.

Table 3.1: A table of evaporation parameters for a variety of materials that we have successfully run in the atom probe. The tip radii are nominal values; the stars indicate that the tip was made from W instead of Si, and have a larger uncertainty in their radius because of their fabrication process. The “turn-on” voltage was estimated from the voltage at which the species first became apparent in the mass spectrum.

Material	Radius (nm)	Temperature (K)	Energy (pJ)	Voltage (kV)
Alq <sub>3</sub>	250	30	15	3.8
Alq <sub>3</sub>	500*	40	20	3.9
BPhen	250	40	30	1.7
C <sub>60</sub>	250	35	12	2.2
C <sub>60</sub>	500*	40	60	1.2
CBP	250	30	8	3.5
DCM2	500*	40	20	4.3
DIP	250	35	12	3.0
DIP	500	30	12	7.5
Ir(ppy) <sub>3</sub>	250	40	30	2.5
Ir(ppy) <sub>3</sub>	500	30	18	6.2
mCBP	250	40	30	2.3
SimCP2	250	30	10	3.9
Tc	500*	40	20	2.2
Tc	500*	40	50	1.4
TCP	250	30	10	3.5
TCP	500	30	10	7.0

materials allows us to use a tip with a radius of curvature ( $R = 250$  to  $500$  nm) which approximates a flat surface locally. A scanning electron microscopy (SEM) image of a Si tip is shown in Figure 3.2.

These tips, though very large compared to a typical APT sample radius of curvature (usually  $\sim 50$  nm),<sup>[40]</sup> still yield smooth evaporation both spatially and temporally. Figure 3.3 shows the smooth variation of hits across the detector, and Figure 3.4 shows the narrow window of voltage used during APT. We note that the fluctuations in voltage during the run are due to CAMECA’s laser drift compensation algorithm for the Local Electrode Atom Probe<sup>TM</sup> 4000X Si (LEAP) not working for our sample geometry, requiring manual laser adjustments to keep the sample properly running; this leads to more abrupt changes in evaporation rate and hence voltage than in typical APT runs.

Thus far we have confined ourselves to thermally evaporable molecules, but this is not a known limitation of the technique. Because small-molecule organic films are sensitive to electron irradiation, the common atom probe practice of imaging the sample in an SEM or transmission electron microscopy (TEM) prior to performing APT can damage the film, creating covalently bridged  $C_{60}$  dimers and trimers, which are both insoluble and cannot be sublimed. Figure 3.5a shows the mass spectrum of a  $C_{60}$  sample that was imaged in a SEM before analysis, which created dimers and trimers of  $C_{60}$ . Because these species are insoluble and cannot be sublimed, this means they must have been created during the electron imaging process. That they evaporate during APT suggests that materials may be analyzed using APT that are not necessarily thermally evaporable, given the right processing conditions. We note that these  $C_{60}$  dimers and trimers are not observed in appreciable quantities in films that have not undergone SEM imaging (Figure 3.5b) under similar analysis conditions. The limits for applicability of APT to organic and other materials systems are not fully known, and merit further study.

In applying a new technique to any system, it is important to understand the quality of information it provides. For APT, there are three major concerns: (1) species discrimination,

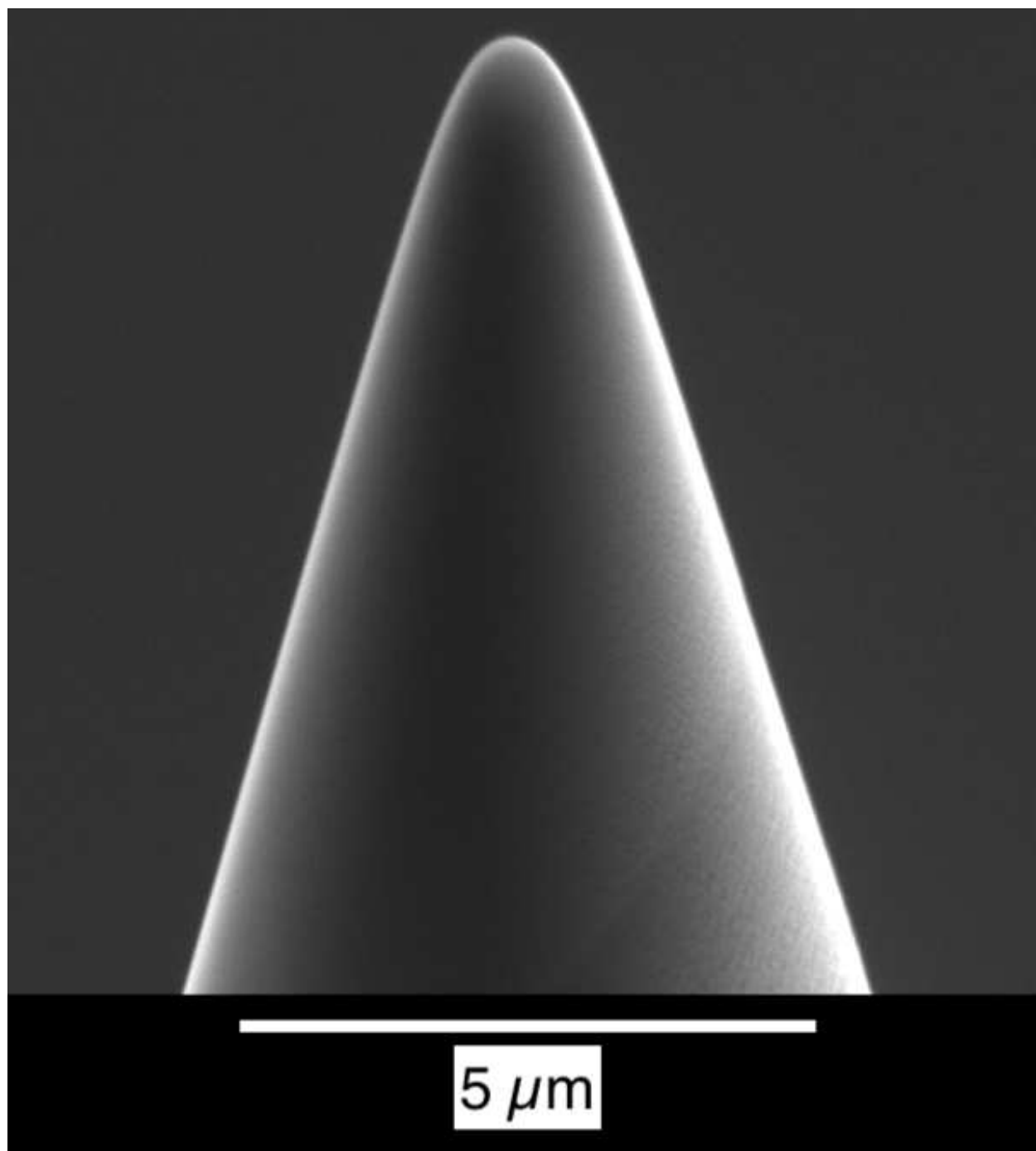


Figure 3.2: A SEM image of a representative Si tip used for film deposition and subsequent APT analysis. The radius of curvature at the apex is  $\sim 500$  nm, which is considerably larger than a typical APT sample tip. Adapted with permission from *Chem. Mater.*, 2019, **31** (7), pp 2241-2247.[54] © 2019 American Chemical Society.

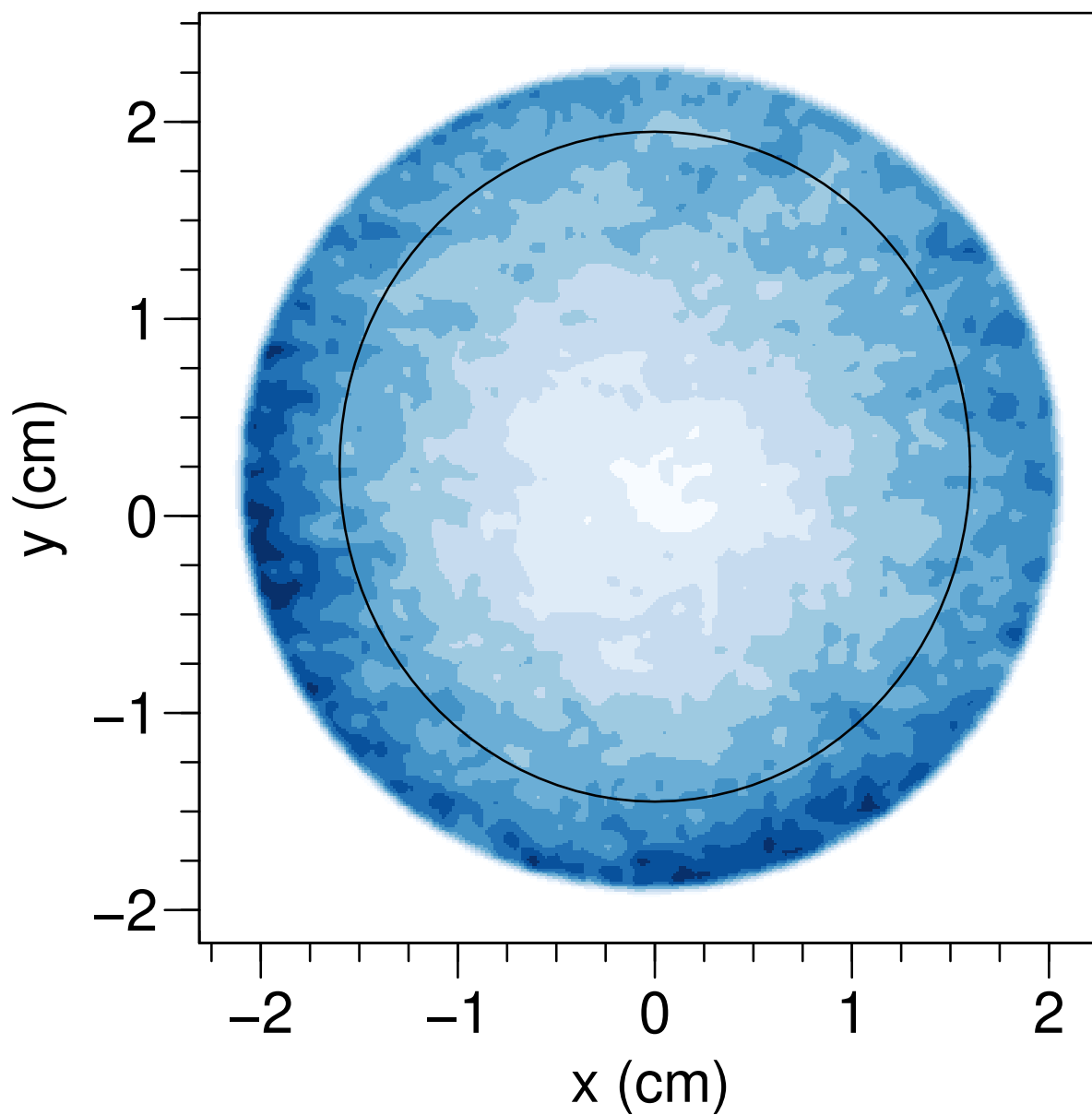


Figure 3.3: A representative detector hit map for our samples. The evaporation varies smoothly across the detector surface. Adapted with permission from *Chem. Mater.*, 2019, **31** (7), pp 2241-2247.[54] © 2019 American Chemical Society.

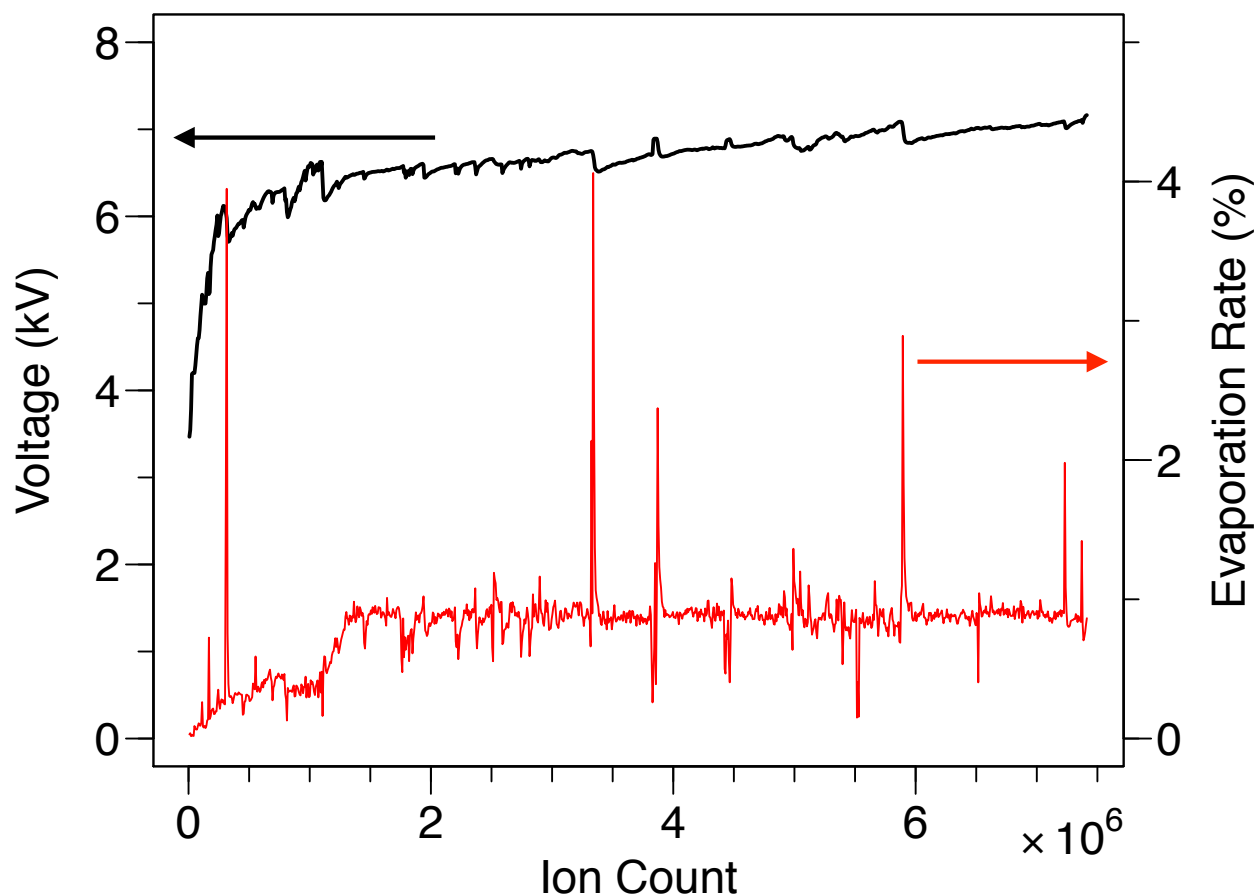


Figure 3.4: A representative voltage curve (black) and corresponding evaporation rate (red) for small-molecule organic semiconductor samples. The fluctuations in the curve are due to CAMECA's laser drift compensation algorithm for the LEAP not working effectively for our sample geometry, requiring manual laser adjustments to keep the sample properly running. Adapted with permission from *Chem. Mater.*, 2019, **31** (7), pp 2241-2247.[54] © 2019 American Chemical Society.

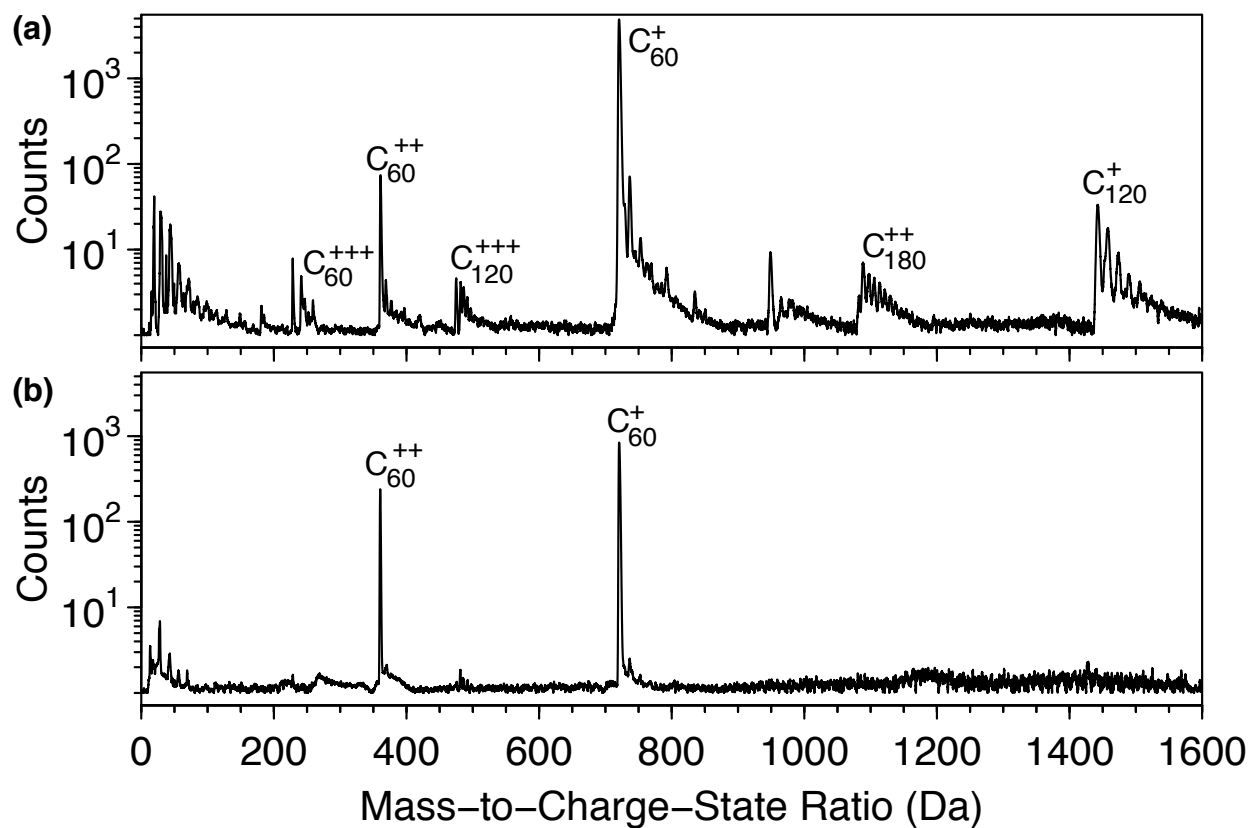


Figure 3.5: (a) Mass spectrum of electron-irradiated  $C_{60}$ , showing evaporation of dimers (singly ionized peaks at 1440 Da and triply ionized peaks at 480 Da; the doubly ionized peaks are subsumed in the primary  $C_{60}$  peak) and trimers (doubly ionized peaks starting at 1080 Da) of  $C_{60}$ . (b) Mass spectrum of unirradiated  $C_{60}$  showing only  $C_{60}$  peaks with no dimers or trimers. Adapted with permission from *Chem. Mater.*, 2019, **31** (7), pp 2241-2247.[54] © 2019 American Chemical Society.

(2) molecular fragmentation, and (3) spatial resolution. We must address each of these to validate APT for organic molecular materials.

In APT, mass resolution is typically characterized by the mass resolving power (MRP) which is given by:[63]

$$MRP = \frac{m}{\Delta m} \quad (3.1)$$

where  $\Delta m$  is the full-width at half-maximum of the peak at mass  $m$ . We have demonstrated MRPs of  $> 1000$  using a flight path length of 160 mm. Figure 3.6 shows part of a mass spectrum collected on a sample of  $C_{60}$  (structure shown in Figure 3.1 (5)) in which the isotopic peaks are clearly resolved; based on the peaks shown, this spectrum has a mass resolving power ( $m/\Delta m$ ) of about 1000 at 720 Da. This high MRP allows definitive identification of the molecular constituents of a sample by comparing the spectrum to the expected isotopic distribution.

Figure 3.7 shows the mass spectrum of a blended film of 6 vol %  $Ir(ppy)_3$  in CBP (purified by thermal gradient sublimation) (their molecular structures are shown in Figure 3.1 (2) & (3)). There is a small but clearly resolvable peak at 319 Da (marked BPC); that we can observe this peak at all is a clear advantage of APT in organic systems, as it comprises only  $\sim 0.5\%$  of the total film. This peak is near the mass of CBP missing one carbazole group, and therefore might be thought to arise from the fragmentation of the molecule during the atom probe evaporation process; however, the high MRP of APT allows us to discern that this peak is 1 Da too heavy for a fragment with a dangling bond, indicating that there is an extra hydrogen, most likely at the 4' position of the biphenyl group. This hydrogen suggests this peak is the known impurity 4-(N-carbazolyl)biphenyl (BPC)[80] in the material either left over from its synthesis or created during film deposition, not a fragment formed during the field evaporation process; we note that the nearby  $Ir(ppy)_3^{++}$  peak is at the expected mass, confirming that the transformation from time-of-flight (TOF) to mass-to-charge is accurate. Therefore, if any fragmentation is occurring, such as the much smaller peaks in the spectrum, they comprise only a small fraction ( $< 1\%$ ) of the data. Furthermore, a run of a blended film

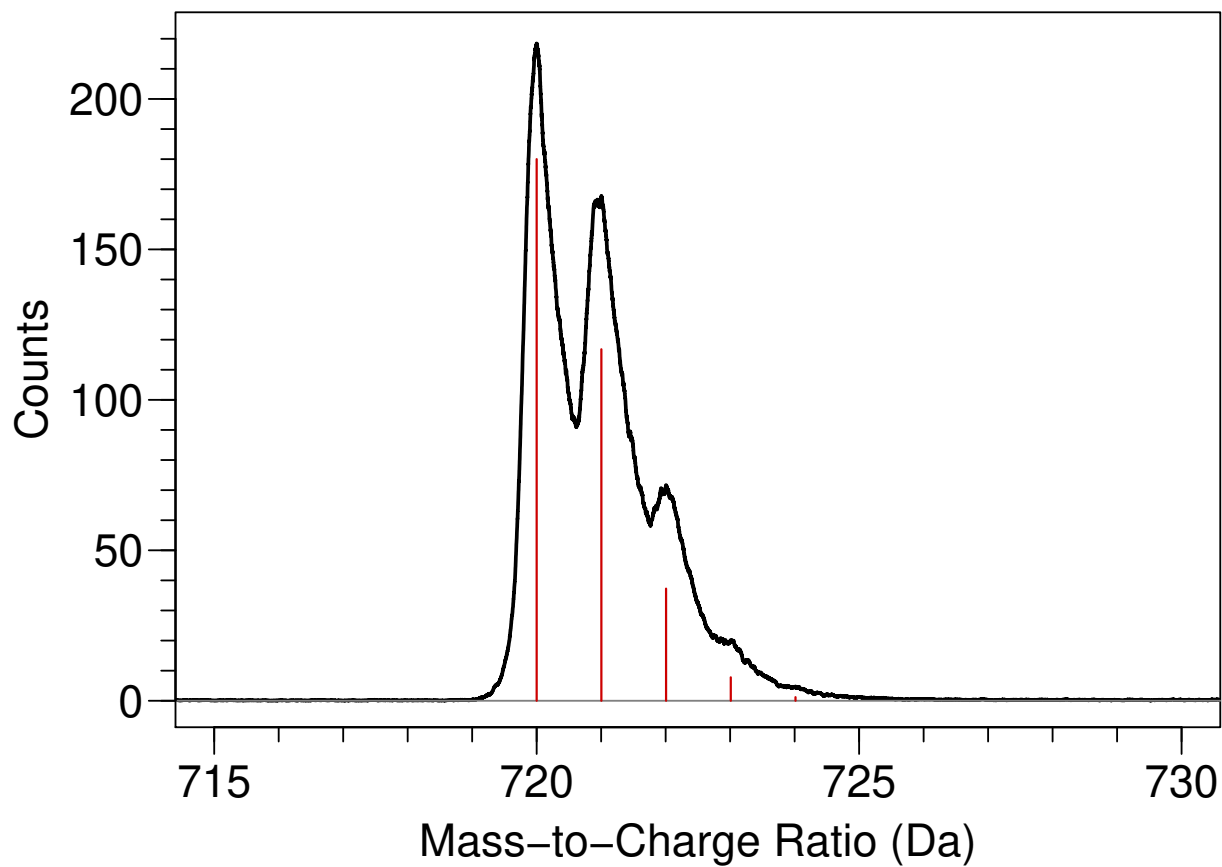


Figure 3.6: Mass spectrum of  $C_{60}^+$  showing isotopic peaks; the red lines are its expected isotopic distribution. Based on the peak separation shown here, this spectrum has a mass resolving power ( $m/\Delta m$ ) of about 1000 at 720 Da. Adapted with permission from *Chem. Mater.*, 2019, **31** (7), pp 2241-2247.[54] © 2019 American Chemical Society.

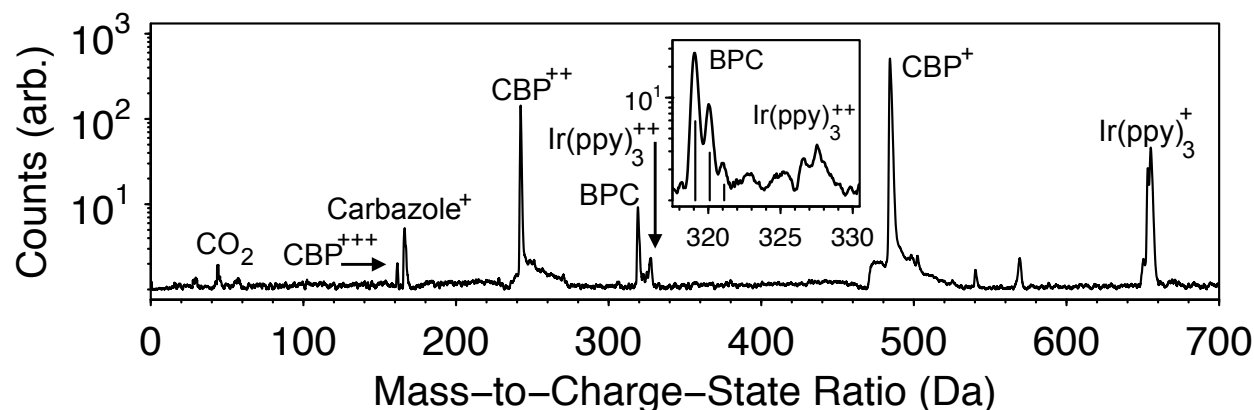


Figure 3.7: Mass spectrum of a blended film of 6 vol % Ir(ppy)<sub>3</sub> in CBP purified by thermal gradient sublimation; (inset) Region of the impurity 4-(N-carbazolyl)biphenyl (BPC) showing a clear offset of 1 Da from the expected fragment location, while the Ir(ppy)<sub>3</sub><sup>++</sup> peak is at its expected mass; the vertical lines in the inset show the expected isotopic positions of the impurity. Adapted with permission from *Chem. Mater.*, 2019, **31** (7), pp 2241-2247.[54] © 2019 American Chemical Society.

of 6 vol % Ir(ppy)<sub>3</sub> in *as-received* CBP (Figure 3.8) shows this impurity comprising about 5 % of the film (with other small peaks similarly increased), further supporting the impurity interpretation of these peaks. Given the noise floor observed in these spectra, we estimate our sensitivity to be approximately 50 ppm.

For the blended film of 6 vol % Ir(ppy)<sub>3</sub> in CBP purified by thermal gradient sublimation, there are three pieces of evidence that support assignment of the peak at 319 Da as an impurity over a fragment. First is the mass detected in the inset of Figure 3.7 indicating the presence of H at the possible fragmentation location. Second is a correlation histogram of the data showing no evidence of fragmentation of the doubly ionized CBP into that peak (Figure 3.9). Third is the relative component of the peak in the *as-received* material (5 %) (Figure 3.8) is an order of magnitude higher as compared to the purified (0.5 %) (Figure 3.7). In the film with *as-received* CBP, with much a higher signal from this impurity peak, there is still no evidence of fragmentation in a correlation histogram (Figure 3.10).

APT provides more data than just spatial position and mass, and this ancillary information can reveal more about what has been observed. Because of both the dynamic

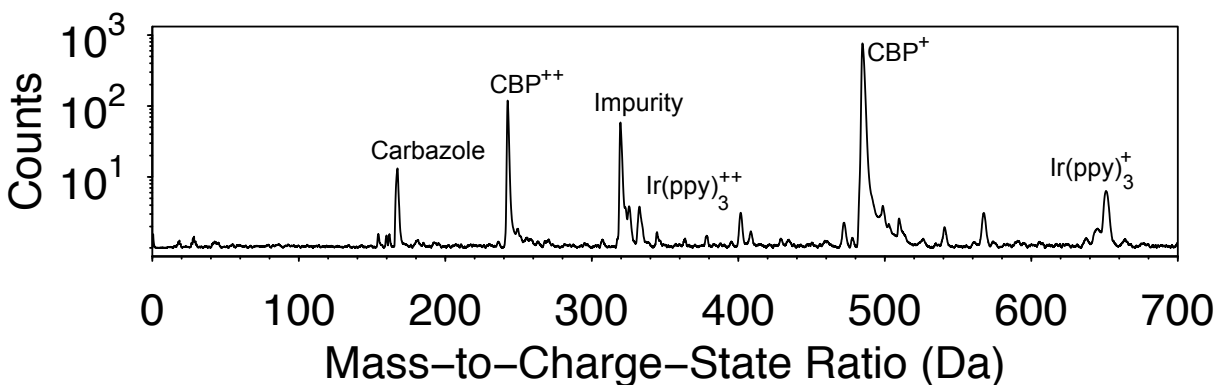


Figure 3.8: Mass spectrum of 6 vol%  $\text{Ir}(\text{ppy})_3$  in *as-received* CBP; the impurity at 319 Da is 5% as compared to 0.5% in the CBP purified by thermal gradient sublimation used in the 6 vol%  $\text{Ir}(\text{ppy})_3$ :CBP blend (Figure 3.7). Adapted with permission from *Chem. Mater.*, 2019, **31** (7), pp 2241-2247.[54] © 2019 American Chemical Society.

distribution of the electric field on the sample’s surface and the stochastic nature of field evaporation events, multiple ions can evaporate during a single pulse.[77] This is sometimes reduced through the selection of run parameters, but these multiple hit events can enhance our interpretation of the data (see Chapter 2). Two dimensional correlation histograms of double hit events during APT runs (Figure 3.10 & Figure 3.9) show no evidence of molecular fragmentation during post-ionization of the  $\text{Ir}(\text{ppy})_3$ :CBP sample, strengthening our rejection of significant fragmentation.[76] We note that similar results are seen for other materials, such as  $\text{Alq}_3$  and even SimCP2, which is one of the larger thermally evaporable small molecules (*i.e.* 977 Da; structure shown in Figure 3.1 (4)).

Because the needle-like shape of the specimen acts as the optic and we use a much larger radius of curvature for our sample than typical APT specimens, it is critical to characterize our spatial resolution. To test our spatial resolution, we prepared a film of  $\text{C}_{60}$  on DIP, which templates  $\text{C}_{60}$  with the (111) plane parallel to the substrate and enhances crystallinity.[81] The crystalline structure provides an internal measure of the spatial resolution of APT for our specimens, which has been the standard method of estimating resolution among the APT community.[82]

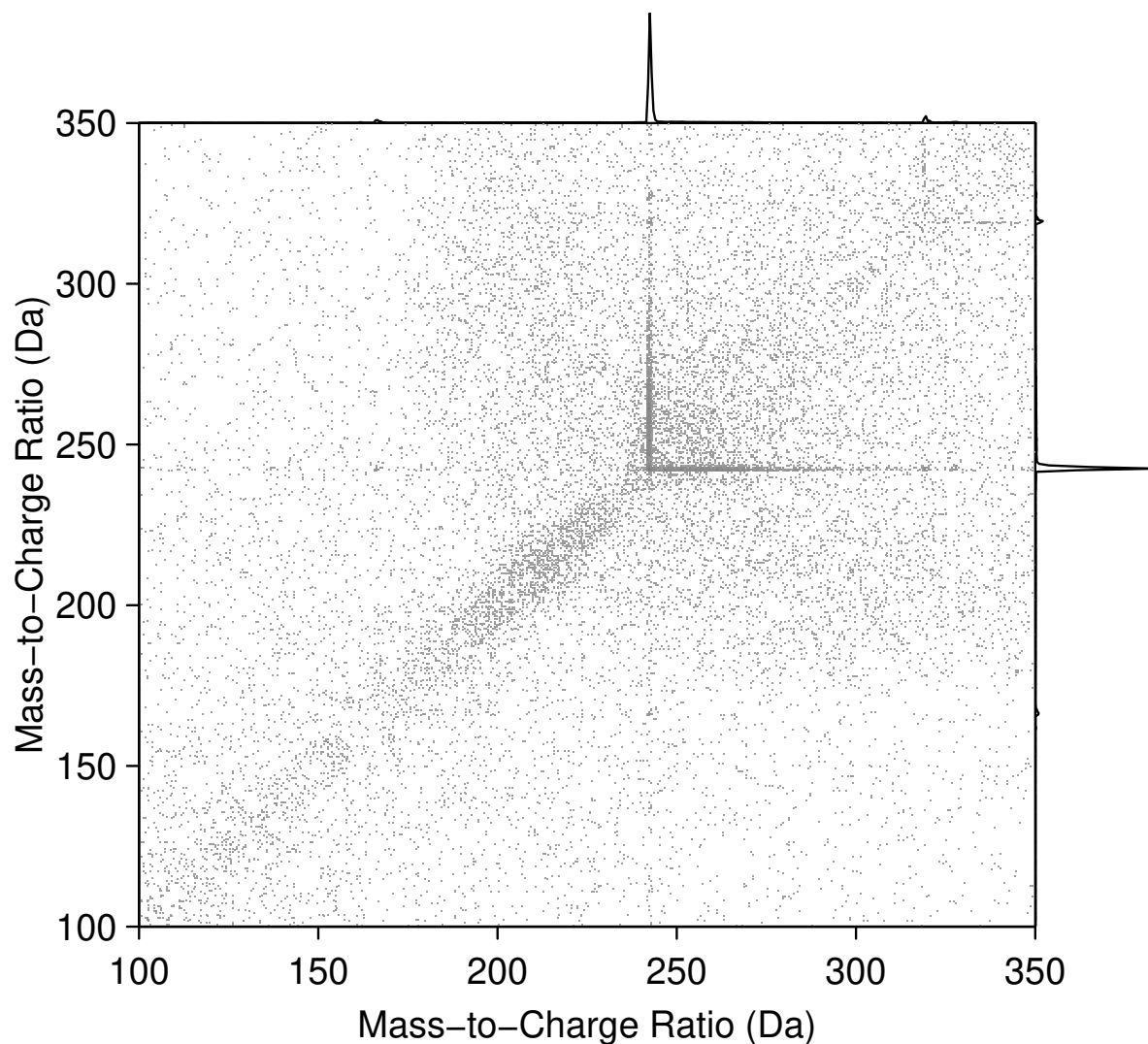


Figure 3.9: A correlation histogram of a blended film of 6 vol% Ir(ppy)<sub>3</sub> in CBP (purified by thermal gradient sublimation) focused on the CBP<sup>++</sup> peak, which shows no evidence of fragmentation of the CBP into the unexpected peaks. Adapted with permission from *Chem. Mater.*, 2019, **31** (7), pp 2241-2247.[54] © 2019 American Chemical Society.

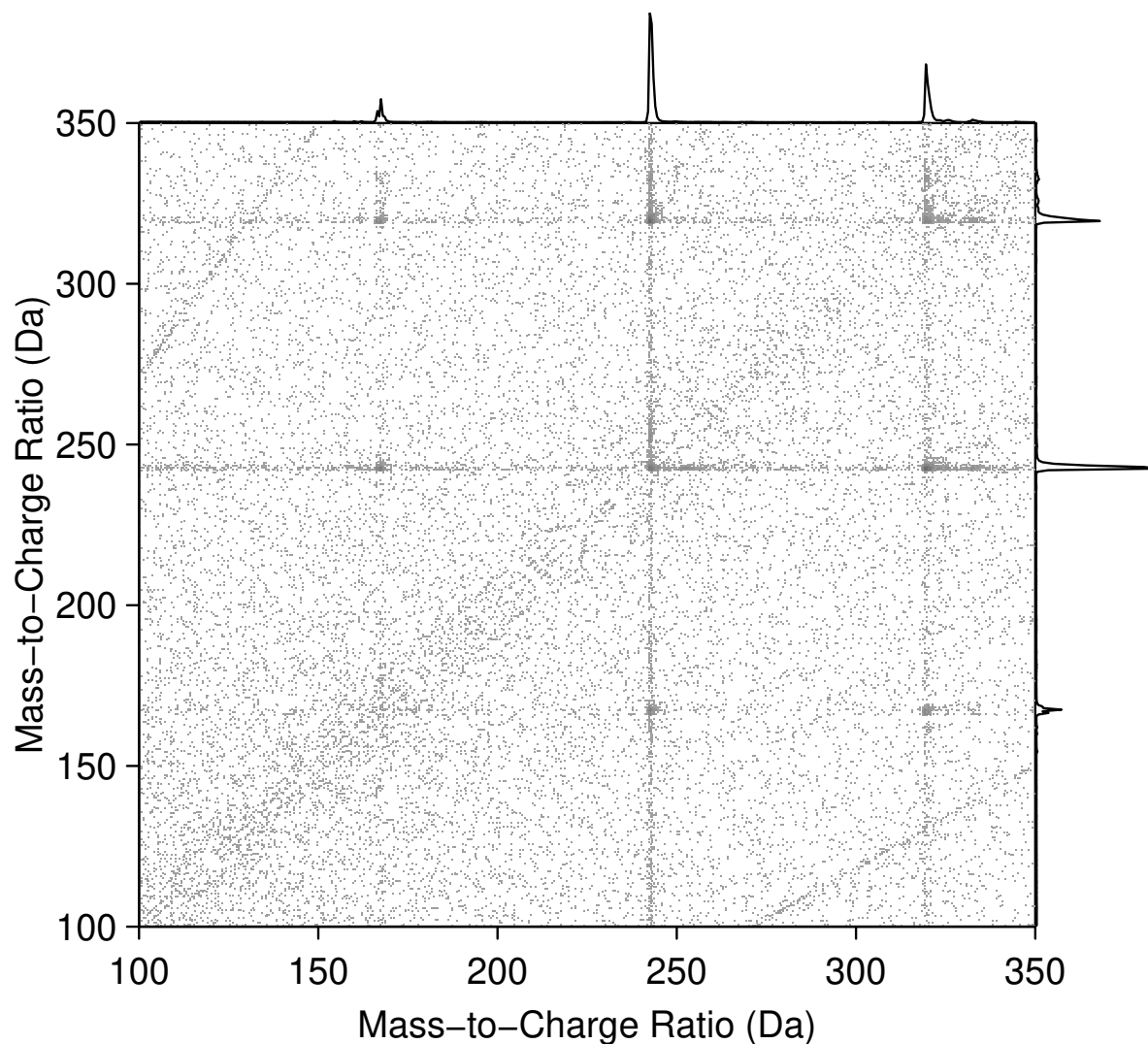


Figure 3.10: A correlation histogram of the as-received CBP focused on the  $\text{CBP}^{++}$  peak at 242 Da, which shows no evidence of fragmentation of the CBP into the unexpected peaks. Adapted with permission from *Chem. Mater.*, 2019, **31** (7), pp 2241-2247.[54] © 2019 American Chemical Society.

To verify that our APT sample was crystallized with (111) texture, we performed x-ray diffraction (XRD) on a co-deposited witness sample (Figure 3.11). XRD data was collected on a Panalytical PW3040 X-ray diffractometer using Cu-K $\alpha$  radiation in the Bragg-Brentano geometry with five Soller slits on the incident and receiving sides over 5 to 30° using a 0.01° step with 5 s integration. The peaks at 10.8 and 21.7° correspond to an inter-planar spacing of 0.817 nm—matching the (111) plane spacing in C<sub>60</sub>—and no other peaks are present, which suggests that the C<sub>60</sub> is indeed (111) textured. The peak intensity is much higher than in non-templated C<sub>60</sub>, suggesting that the crystallinity of the C<sub>60</sub> is enhanced, as demonstrated by Hinderhofer et al. [81].

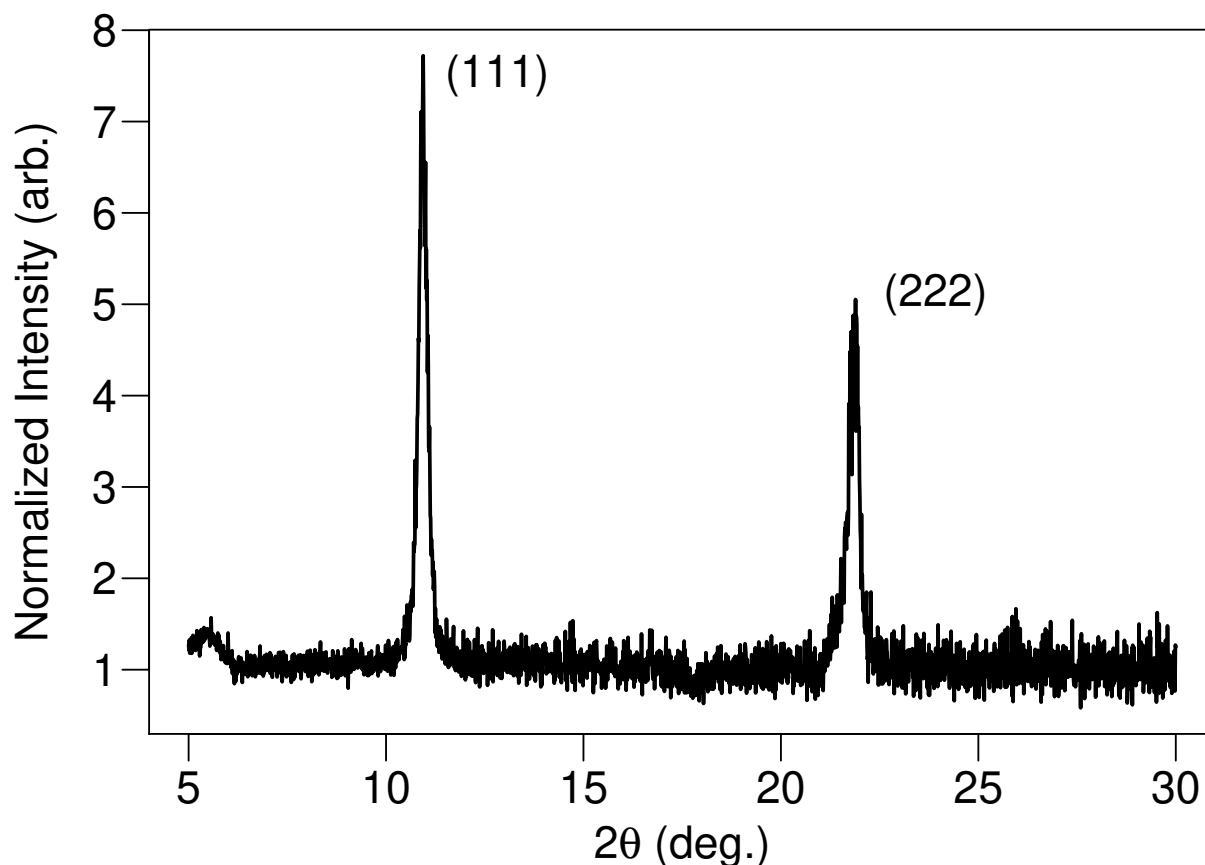


Figure 3.11: An x-ray diffraction (Cu-K $\alpha$ ) measurement of the diindenoperylene (DIP)/C<sub>60</sub> film showing it is textured with the (111) plane parallel to the substrate. Adapted with permission from *Chem. Mater.*, 2019, **31** (7), pp 2241-2247.[54] © 2019 American Chemical Society.

Figure 3.12 shows the film’s z-axis spatial distribution map (SDM)—a common analysis method for crystalline APT data that measures the distribution of z-axis components of the vectors between points in a neighborhood; the components can be combined radially to yield the radial distribution function (see Chapter 2). [42] We used a neighborhood of diameter 2.4 nm on the detector, corresponding to a sampled volume of  $\sim 2600 \text{ nm}^3$ ; formally, the resolution of the reconstruction is only well-defined in this region, but for the following discussion we extrapolate to the entire detected region. Fitting to a model of evenly spaced Gaussian functions with equal standard deviations allows us to extract information about our resolution. The regular spacing of the peaks is  $0.817 \pm 0.002 \text{ nm}$  with this reconstruction using the model fit, which corresponds to the expected (111) lattice planes of the oriented  $\text{C}_{60}$  at 0.817 nm measured with XRD on the co-deposited witness.[83] The width of the peaks indicates that the spatial resolution of this sample—which we define as the standard deviation of the fitted Gaussians—is  $0.313 \pm 0.003 \text{ nm}$  in the z-direction, or  $\sim 0.3 \text{ nm}$  taking other uncertainties into account. We note that this is not a physical limit of the resolution for the technique—which has been shown to achieve z-resolutions of  $< 20 \text{ pm}$ [82]—but what was achieved for this particular sample.

Given this known dimension in z, we can adjust the reconstruction parameters to return the expected density of the crystal. This reconstruction allows for estimation of the field of view, which for this sample is around 760 nm; as there are about 800 pixels across the detector,[65] our x-y resolution is limited to about 1 nm but could be improved with different sample geometries (*e.g.* decreasing the shank angle of the tip) or increasing the detector path length.

The high chemical discrimination ( $< 1 \text{ Da}$ ), spatial resolution ( $\sim 0.3 \text{ nm}$  in z and  $\sim 1 \text{ nm}$  in x-y), and analytic sensitivity ( $\sim 50 \text{ ppm}$ ) demonstrated here for APT of small-molecule organic semiconducting materials open up avenues for scientific inquiries in these systems that were previously extremely difficult.

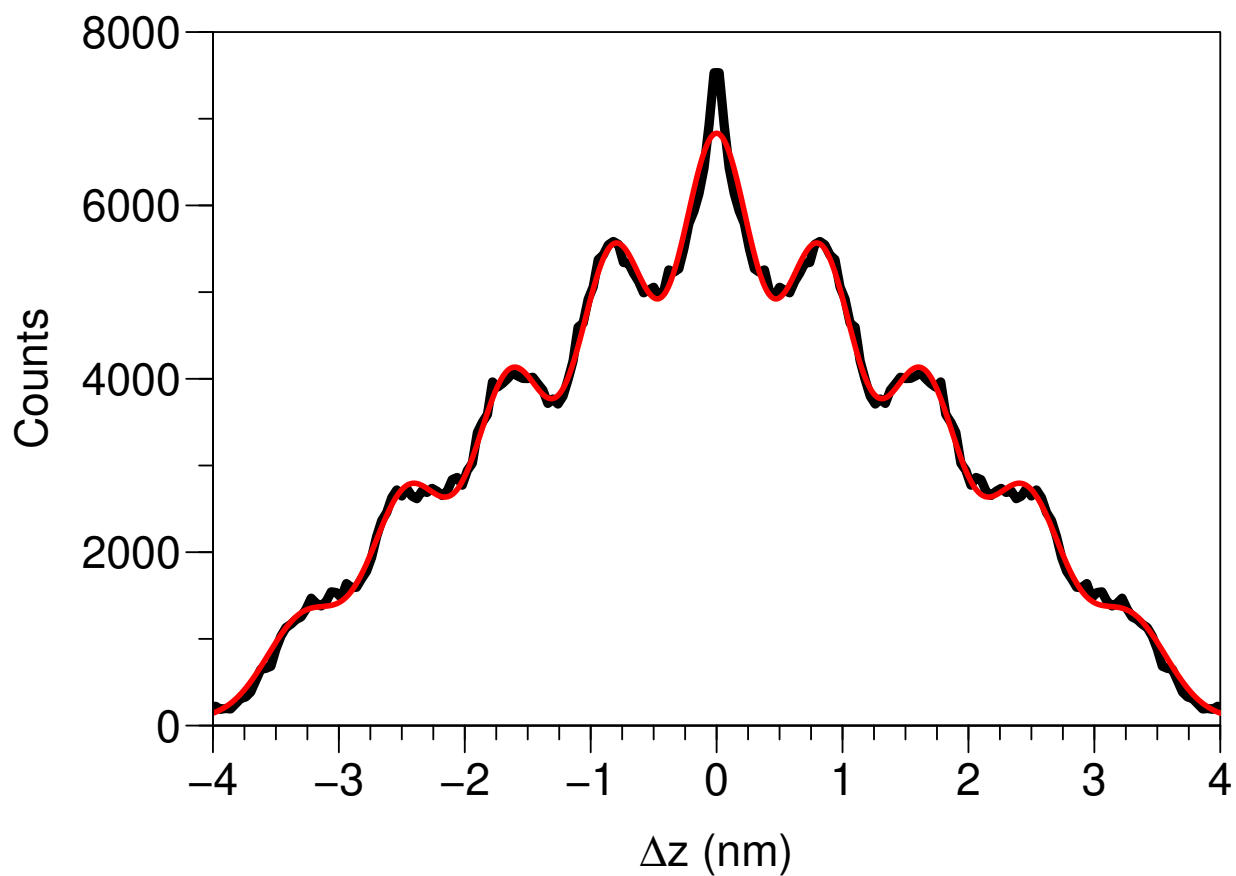


Figure 3.12: Spatial distribution map (SDM) of  $C_{60}$  templated on DIP showing crystal lattice planes in the  $z$  direction. The sampled volume is  $\sim 2600 \text{ nm}^3$ . A fit to the peaks (red) indicates the spatial resolution of this sample in the  $z$  dimension is  $\sim 0.3 \text{ nm}$ . Adapted with permission from *Chem. Mater.*, 2019, **31** (7), pp 2241-2247.[54] © 2019 American Chemical Society.

## CHAPTER 4

### SCIENTIFIC DISCOVERIES

*APT is valuable for the study of small-molecule semiconducting materials, providing three-dimensional chemical information at the nanometer scale using molecular mass to distinguish chemical species.*

–Proudian et al. [1]

To this point, we have developed the necessary background and validation for atom probe tomography (APT) of small-molecule organic semiconducting systems. This effort now permits us to explore the vast field of scientific questions accessible *via* APT. Here, we discuss three areas that demonstrate the power of APT to uncover structure-property relationships in organic systems that have proven extremely difficult to probe using existing techniques: (1) the interface of a model organic photovoltaic (OPV) system in which we show a chemical reaction occurs at the heterointerface;<sup>[1]</sup> (2) the bulk structure of a model organic light-emitting diode (OLED) system in which we show molecular segregation occurs,<sup>[54]</sup> and (3) the degradation of an OLED material under exposure to ultraviolet (UV) light. **Again, the following draws upon Proudian et al. [1] and Proudian et al. [54].**

#### 4.1 Interface

In 2016, we used APT to investigate the behavior of the bilayer fullerene/acene small-molecule OPV system—one of the most studied models for testing our understanding of the crucial heterojunction interface for OPVs.<sup>[1]</sup> APT revealed that the fullerene and acene molecules chemically react at the heterojunction interface, creating a partial monolayer of a Diels-Alder cycloadduct (DAc) species that standard processing techniques cannot eliminate. This spatially resolved chemical resolution helps explain changes in device performance due to the presence of the DAc.

A fullerene molecule can make its closest contact with the edge, face, or end of an acene molecule, or any position between these extremes. Models of acene/ $C_{60}$  contact configurations predict that the intermolecular coupling, which determines charge transfer (CT) state recombination and dissociation rates, is significantly different for each configuration;[84] furthermore, face-on interfaces are likely morphologically unstable with a high probability of the acene and fullerene mixing.[85] Meanwhile, experimental work has struggled to directly confirm the effects of interface orientation on device parameters.[86] At the same time, efforts to understand how steric hindrance affects device parameters such as open circuit voltage ( $V_{OC}$ ) in tetracene (Tc)/ $C_{60}$  and rubrene/ $C_{60}$  based devices remain an active area of study.[87]

Part of the reason for the difficulty in experimentally reproducing the model results is that the high electron affinity of the fullerene cage makes it reactive with electron-rich acene molecules through Diels-Alder cycloaddition.[88–91] This reaction is commonly used for functionalization of  $C_{60}$  with polycyclic aromatic hydrocarbons.[91–94] Of particular relevance is the well understood [4+2] cycloaddition of  $C_{60}$  to short linear acenes (*i.e.* anthracene, tetracene and pentacene) in solution.[90, 91, 94–101] The reaction of Tc and  $C_{60}$  produces a DAc, which has been shown to occur in the solid state during vibration milling,[102] and is thermally stable up to 300 °C.[90] This reaction is most likely to proceed when the  $\pi$ -system of the acene is tangent to the fullerene, obscuring the expected effects of interface orientation.[103] The presence of a DAc at acene-fullerene interfaces was predicted by Anthony in 2008,[104] but due to the difficulty of detection, experimental evidence for a Diels-Alder cycloaddition reaction between pentacene and  $C_{60}$  bilayers was not demonstrated until 2016.[105] Using APT and Fourier transform infrared spectroscopy (FTIR) spectroscopy, we unequivocally show that Tc/ $C_{60}$  interfaces undergo a Diels-Alder cycloaddition reaction creating DAc species, even in the typical end-on interface configuration most commonly found in devices.[105, 106]

Mass spectra collected from APT are shown in Figure 4.1 for a bilayer sample of a 40 nm layer of  $C_{60}$  followed by a 60 nm layer of Tc and a co-deposited sample of Tc: $C_{60}$  in

a 1:1 volume blend with a total layer thickness of 100 nm. Both mass spectra contain peaks corresponding to the masses of Tc,  $C_{60}$ , and the covalently bonded DAC; Table 4.1 provides an extended list of peak identifications. The peak at 948 Da, the sum of the masses of  $C_{60}$  and Tc, indicates that the DAC species is present in our samples. Bilayer samples have only  $\sim 0.36\%$  of the total ion count detected in APT are DAC molecules, making the absorption signal difficult to confidently discern using established methods (*e.g.* FTIR). To increase the interfacial area and number of DAC molecules present, the Tc and  $C_{60}$  were co-deposited (1:1 by volume), increasing the DAC concentration to  $\sim 11\%$  of the total ion count. FTIR measurements on the co-deposited film confirm the presence of vibrational modes previously attributed to the DAC:[1] the appearance of a strong absorption band at  $700\text{ cm}^{-1}$ , a weak band at  $804\text{ cm}^{-1}$ , and a shift in the band at  $750\text{ cm}^{-1}$  all correspond to aromatic out-of-plane bending modes confirm the presence of the DAC species.[90]

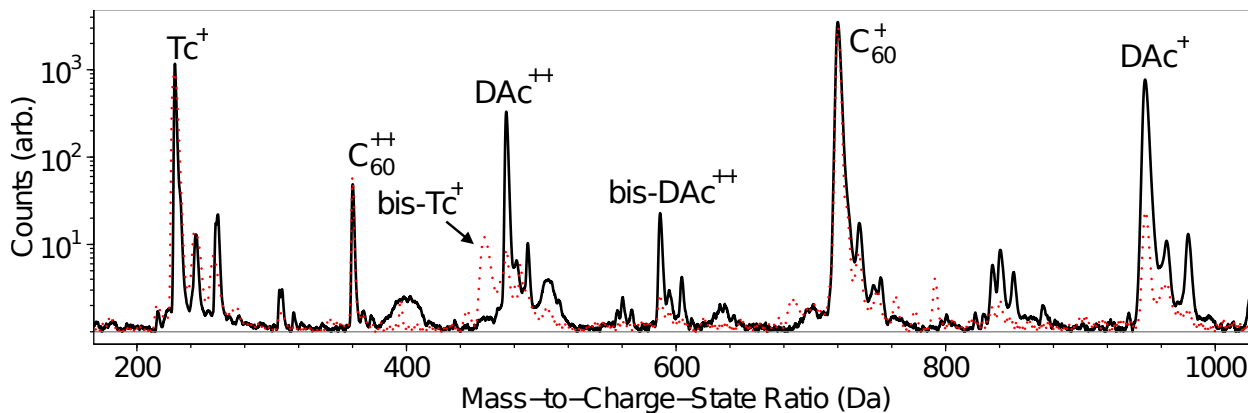


Figure 4.1: Mass spectra for the co-deposited (solid black) and bilayer (dotted red) samples. Major peaks are labeled with molecular species and charge state: tetracene (Tc), Diels-Alder cycloadduct (DAC), tetracene dimer (bis-Tc), and a  $C_{60}$  with two tetracene adducts (bis-DAC); an extended list of peaks is provided in Table 4.1. In the blended sample the concentration of DAC is  $\sim 11\%$  of the total ion count, while in the bilayer sample it is only  $\sim 0.36\%$ . Even at this low concentration in the bilayer sample, the DAC peak is clearly visible. Adapted with permission from *Nano Lett.*, 2016, **16** (10), pp 6086–6091.[1] © 2016 American Chemical Society.

Knowing the existence of the DAC and its peak location in the co-deposited sample allows us to look for and extract it from a measurement of a bilayer sample as well. FTIR

Table 4.1: Masses and associated compounds for the APT mass spectrum shown in Figure 4.1, where bis-Tc is a covalently bonded Tc dimer, C<sub>120</sub>-DAc is a covalent dimer of C<sub>60</sub> with a single Tc adduct, and bis-DAc is a C<sub>60</sub> with two Tc adducts.

Mass-to-Charge Ratio (Da)	Ion Formula	Compound
228	C <sub>18</sub> H <sub>12</sub> <sup>+</sup>	Tc
224	C <sub>18</sub> H <sub>12</sub> O <sup>+</sup>	Tc oxide
260	C <sub>18</sub> H <sub>12</sub> O <sub>2</sub> <sup>+</sup>	Tc oxide
316	C <sub>78</sub> H <sub>12</sub> <sup>+++</sup>	DAc
360	C <sub>60</sub> <sup>++</sup>	C <sub>60</sub>
368	C <sub>60</sub> O <sup>++</sup>	C <sub>60</sub> oxide
376	C <sub>60</sub> O <sub>2</sub> <sup>++</sup>	C <sub>60</sub> oxide
392	C <sub>96</sub> H <sub>24</sub> <sup>+++</sup>	bis-DAc
456	C <sub>36</sub> H <sub>24</sub> <sup>+</sup>	bis-Tc
474	C <sub>78</sub> H <sub>12</sub> <sup>+</sup>	DAc
482	C <sub>78</sub> H <sub>12</sub> O <sup>++</sup>	DAc oxide
490	C <sub>78</sub> H <sub>12</sub> O <sub>2</sub> <sup>++</sup>	DAc oxide
556	C <sub>138</sub> H <sub>12</sub> <sup>+++</sup>	C <sub>120</sub> -DAc
559	C <sub>138</sub> H <sub>12</sub> O <sup>+++</sup>	C <sub>120</sub> -DAc oxide
561	C <sub>138</sub> H <sub>12</sub> O <sub>2</sub> <sup>+++</sup>	C <sub>120</sub> -DAc oxide
588	C <sub>96</sub> H <sub>24</sub> <sup>++</sup>	bis-DAc
720	C <sub>60</sub> <sup>+</sup>	C <sub>60</sub>
736	C <sub>60</sub> O <sup>+</sup>	C <sub>60</sub> oxide
754	C <sub>60</sub> O <sub>2</sub> <sup>+</sup>	C <sub>60</sub> oxide
834	C <sub>138</sub> H <sub>12</sub> <sup>++</sup>	C <sub>120</sub> -DAc
842	C <sub>138</sub> H <sub>12</sub> O <sup>++</sup>	C <sub>120</sub> -DAc oxide
850	C <sub>138</sub> H <sub>12</sub> O <sub>2</sub> <sup>++</sup>	C <sub>120</sub> -DAc oxide
948	C <sub>78</sub> H <sub>12</sub> <sup>+</sup>	DAc
964	C <sub>78</sub> H <sub>12</sub> O <sup>+</sup>	DAc oxide
980	C <sub>78</sub> H <sub>12</sub> O <sub>2</sub> <sup>+</sup>	DAc oxide

measurements on bilayer Tc/C<sub>60</sub> samples, both as-deposited and annealed at 75, 100, and 125 °C, show the presence of the DAc, albeit at the edge of the detection limit (Figure 4.2). The increased magnitude of the strength of the vibrational mode at 700 cm<sup>-1</sup> (see Figure 4.2, inset) indicates the amount of DAc increases on annealing, as does the continued shift of the band at 750 cm<sup>-1</sup>.

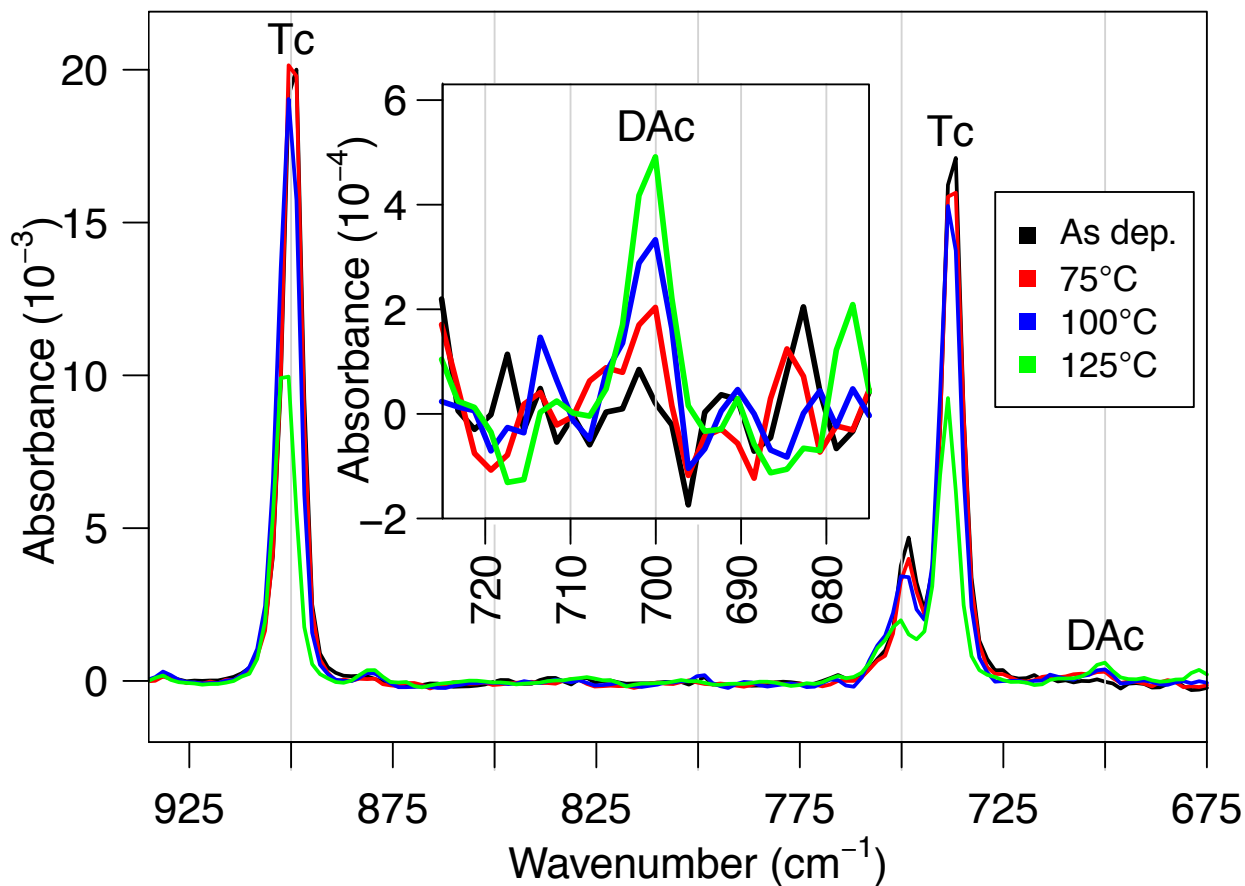


Figure 4.2: FTIR data demonstrating a progressive increase in the intensity of the DAc vibrational mode at 700 cm<sup>-1</sup> (inset) with increasing annealing temperature for bilayer samples (Si / 50 nm Tc / 50 nm C<sub>60</sub>); a new automatic baseline was taken from 675 to 725 cm<sup>-1</sup> for the inset. In the as-deposited film (black), the vibrational mode is indistinguishable from the noise, demonstrating the value of APT for primary species identification. Adapted with permission from *Nano Lett.*, 2016, **16** (10), pp 6086–6091.[1] © 2016 American Chemical Society.

Detection of the low concentration of the DAc in the bilayer sample demonstrates the impressive sensitivity of APT to observe chemical changes and impurities in molecular organic

systems. In the as-deposited FTIR sample of Figure 4.2, the main DAc peak at  $700\text{ cm}^{-1}$  is indistinguishable from the noise. Compare this to the clear DAc signal in the mass spectrum of the bilayer sample measured in APT shown in Figure 4.1: while other methods can be used for subsequent analysis and confirmation, it is only possible to identify the DAc in the first place because of APT’s high sensitivity.

While APT’s high chemical sensitivity helps direct the confirmation of the chemical reaction resulting in the DAc, its spatial information helps direct our explanation of device changes. The concentration profile of the bilayer sample in Figure 4.3a shows that DAc is confined to the interface, and the distribution of the DAc in the plane of the interface (Figure 4.3b) has no discernible structure; in fact, the low concentration means the DAc is a sub-monolayer right at the interface, which is clear from the APT reconstruction.

Because the DAc has a lowest unoccupied molecular orbital (LUMO) energy  $\sim 0.16\text{ eV}$  shallower than  $\text{C}_{60}$ , the presence of the DAc at the heterojunction interface should affect device properties.[102] To test the effects of the DAc on device parameters, we purposefully introduced an “interlayer” of DAc by co-depositing a  $\text{Tc}:\text{C}_{60}$  blend at the interface. The data in Figure 4.4 demonstrate that the interfacial reaction does indeed change device properties: the devices with the co-deposited interlayer show higher  $V_{OC}$  than the bilayer devices. Furthermore, the increase of  $V_{OC}$  with annealing temperature in all devices corresponds to an increase in the DAc as measured by FTIR. This information, combined with a temperature series of external quantum efficiency and  $V_{OC}$  measurements,[1] allows us to determine that—because face-on  $\text{Tc}/\text{C}_{60}$  interfaces have the smallest CT-exciton energy[107] and are the most reactive[103]—these sites should form the DAc first upon annealing, removing the deepest traps sites from the density of states at the heterointerface. This reduces the average reorganization energy for CT-exciton formation, consequently increasing  $V_{OC}$ .

This problem takes advantage of APT’s strengths: there is no elemental composition change for this species, and its concentration and location in the film are critically important to understanding its impact on device performance, making it extremely challenging

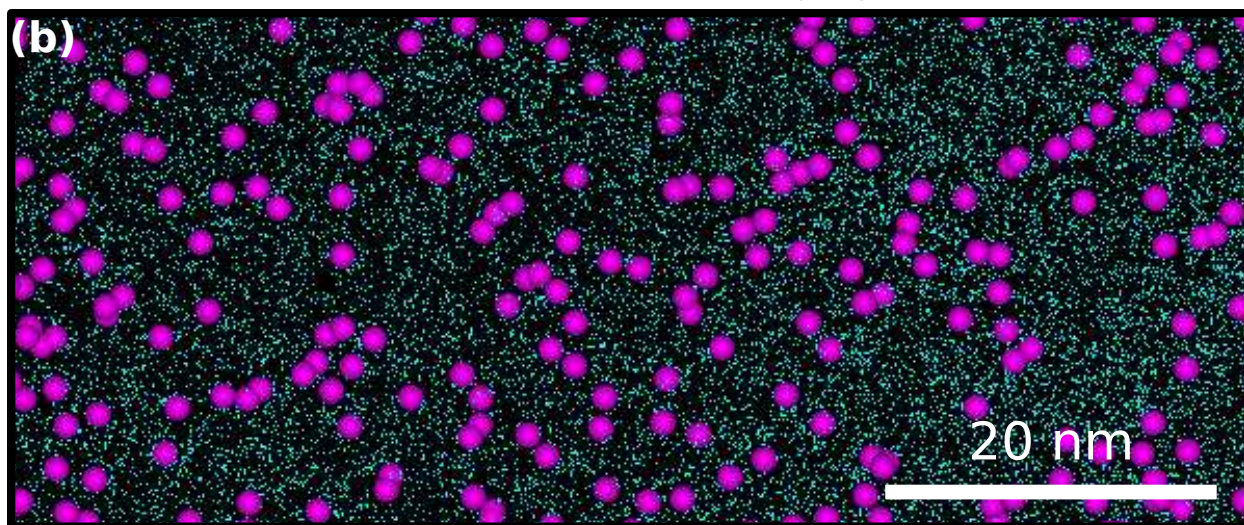
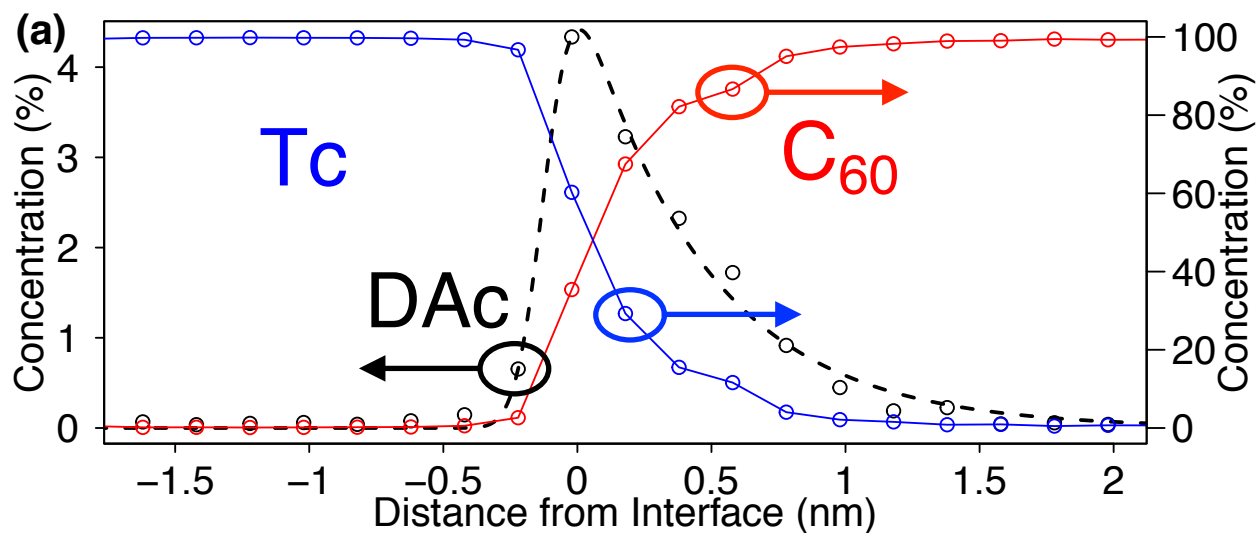


Figure 4.3: (a) Molecular concentration profile near the interface of the  $C_{60}$ -Tc planar heterojunction. The concentration of the DAC is confined to the interface. (b) Positions of DAC (purple spheres) in the plane of the  $C_{60}$ /Tc interface viewed from the  $C_{60}$  side (Tc shown as teal points). There is no discernible structure to the positions of DAC in this plane. Adapted with permission from *Nano Lett.*, 2016, **16** (10), pp 6086–6091.[1] © 2016 American Chemical Society.

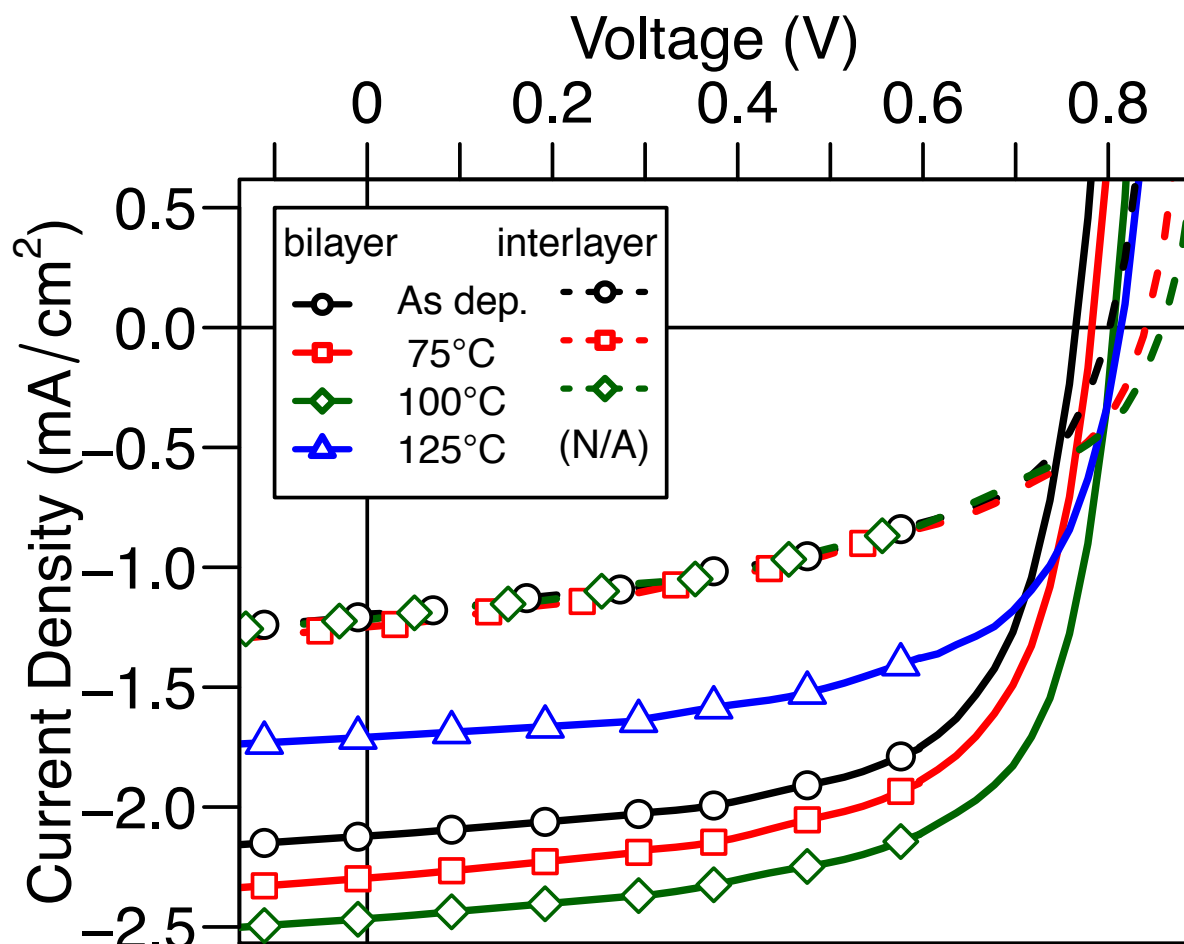


Figure 4.4: Representative current density-voltage ( $J$ - $V$ ) curves for Tc/C<sub>60</sub> bilayer devices under 1 sun illumination (AM1.5), tested as-deposited and after annealing at 75, 100, and 125 °C for 30 min (solid lines). Equivalent devices with a 10 nm Tc:C<sub>60</sub> interlayer are also shown in dashed lines with symbols and colors that correspond to annealing conditions for the bilayer devices. The devices with the co-deposited interlayer show higher  $V_{OC}$  than the bilayer devices. The increase of  $V_{OC}$  with annealing temperature in all devices corresponds to an increase in the DAc as measured by FTIR. Adapted with permission from *Nano Lett.*, 2016, **16** (10), pp 6086–6091.[1] © 2016 American Chemical Society.

to resolve with other techniques. The development of this analysis, and the explanation that resulted, was only possible because of the unique capabilities of APT. Measuring the clear structure-property relations of an organic system moves the field closer to closing the experiment-theory loop.

## 4.2 Bulk

In 2019, we used APT to look at the structure of a blend of tris[2-phenylpyridinato-C<sub>2</sub>,N]iridium(III) (Ir(ppy)<sub>3</sub>) in 4,4'-bis(N-carbazolyl)-1,1'-biphenyl (CBP)—one of the most commonly studied OLED emissive layers.[54] APT revealed that Ir(ppy)<sub>3</sub> is not randomly distributed in the CBP host, tending to aggregate instead. This information helps direct studies of these morphologies as they relate to both devices and device simulations.

In fluorescent and phosphorescent systems such as OLEDs, high enough local concentrations of the emitter molecule can cause concentration quenching—an issue where a sufficient dopant concentration allows for rapid non-radiative relaxation to the ground state, reducing efficiency.[108, 109] The first report of concentration quenching in OLEDs was by Tang et al. [110] two years after their seminal paper describing efficient organic electroluminescence.[57] Additionally, changes in the overall concentration of the OLED emitter guest strongly affect rates of triplet-triplet annihilation (TTA) and triplet-polaron quenching (TPQ).[32, 111, 112] These concentration effects impact both efficiency, peak emission wavelength, and lifetime, and are compounded for systems in which the guest emitter molecule aggregates.[32]

The heavily-studied, archetypal phosphorescent OLED system of CBP:Ir(ppy)<sub>3</sub> is suspected of this emitter aggregation, increasing self-quenching, exciton-exciton and exciton-polaron interaction, and device degradation.[32, 113–116] Measuring aggregation in OLED active layers is a natural problem for APT, which can easily discriminate and locate each molecule with high precision. To study aggregation, we deposited a blended film of 6 vol% Ir(ppy)<sub>3</sub> in CBP—a typical blend ratio for this system;[116] the measured bulk composition of the blend through APT is 5.8 ion% Ir(ppy)<sub>3</sub>. We note that while these percentages differ in their calculation (vol% versus ion%), the molecules are close in size and the variation is

within the error of the crystal monitor calibration.

To formally characterize clustering of Ir(ppy)<sub>3</sub> in the sample, we use the three-dimensional K-function ( $K_3$ ) on Ir(ppy)<sub>3</sub> marked points (see Chapter 2). This is necessary because inspecting the data set by eye does not readily distinguish lower levels of dopant clustering: a region of the reconstruction from two perspectives is shown in Figure 4.5, but little can be determined from this rendering. Using the common method of looking at heat map projections along these perspectives (Figure 4.6a,b) for “hot spots” shows some variation; however, this does not indicate the significance of the clustering because it relies on subjectively interpreting the data, so a more rigorous test must be used.

Acceptance interval envelopes were generated for the measured K-function (Figure 4.6c) by randomly relabeling the molecular identities of the measured CBP and Ir(ppy)<sub>3</sub> locations 50,000 times and calculating  $K_3(r)$  of the relabeled Ir(ppy)<sub>3</sub> patterns. Deviations above this envelope indicate statistically significant non-random clustering of the observed Ir(ppy)<sub>3</sub> at those distances.

To stabilize the variance of the envelopes, we use the square root of the K-function; this transformation does not change any of the underlying conclusions drawn about the observed data, and is commonly used in the analysis of point patterns.[73, 117] To make interpretation of the data easier, we also subtract the median value of the envelope, centering the plot about zero. From the transformed K-function and envelopes shown in Figure 4.6c, we observe significant (deviation outside a 99.9% acceptance interval) clustering of the Ir(ppy)<sub>3</sub> in the range of about 5 to 12 nm. This corroborates earlier work using HAADF-STEM that suggested clustering of Ir(ppy)<sub>3</sub> in 4,4',4''-tris(N-carbazolyl)-triphenylamine (TCTA),[32] but adds quantitative length scales in three dimensions that allow for better models of mixing and charge transport. Furthermore, this K-function analysis of APT data can be extended to general small-molecule organic systems, as it does not require a high z-contrast atom such as the Ir core in Ir(ppy)<sub>3</sub>. The effect of the observed clustering on device properties as well as further morphological analysis will be explored in future publications.

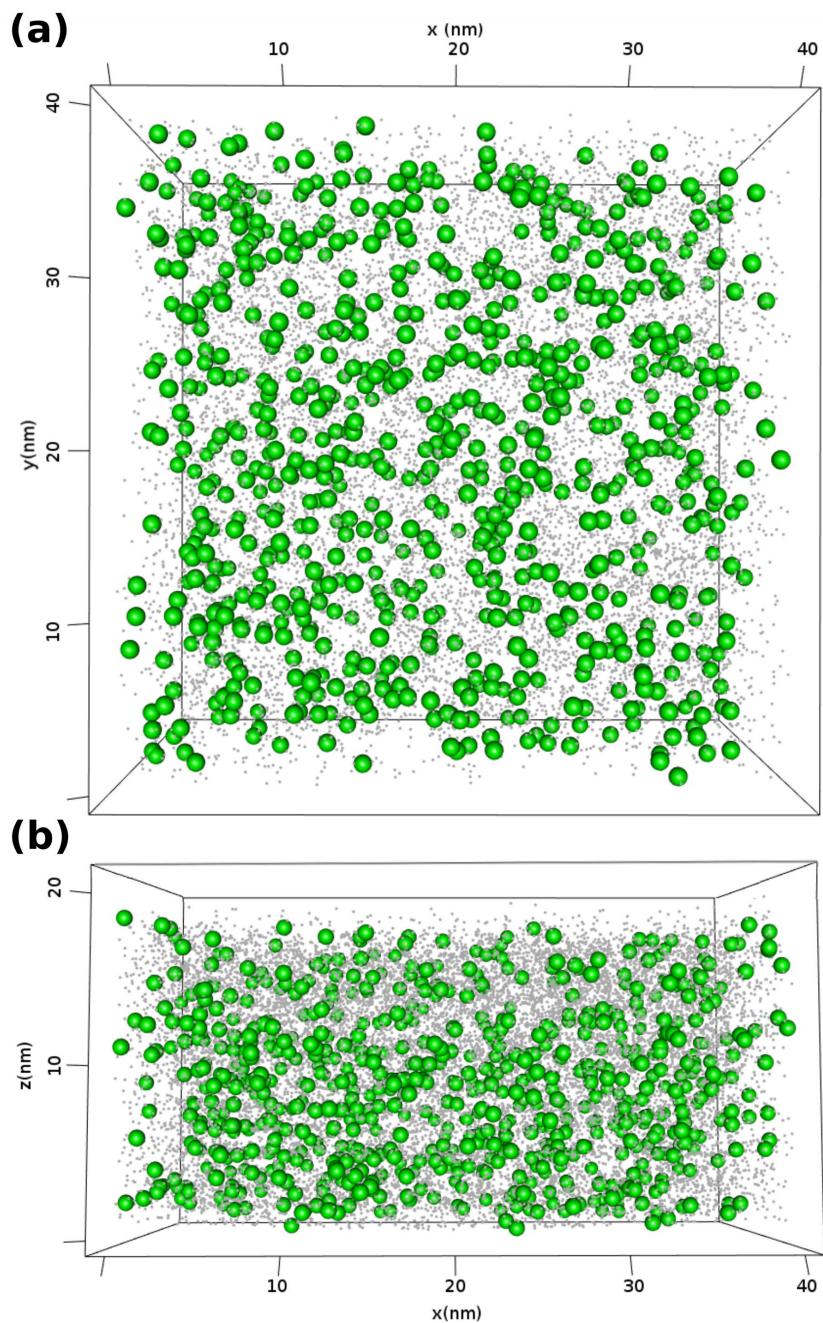


Figure 4.5: A three-dimensional plot of the points used to generate the  $K_3$  cluster analysis shown in Figure 4.6c from the perspective of the heat maps in Figure 4.6a,b. The black dots are 4,4'-bis(N-carbazolyl)-1,1'-biphenyl (CBP) while the green spheres are tris[2-phenylpyridinato-C2,N]iridium(III) ( $\text{Ir}(\text{ppy})_3$ ). There is no obvious structure to the  $\text{Ir}(\text{ppy})_3$ , but a more rigorous test (*e.g.*  $K_3$ ) is required to determine whether they are randomly distributed in the CBP matrix. Adapted with permission from *Chem. Mater.*, 2019, **31** (7), pp 2241-2247.[54] © 2019 American Chemical Society.

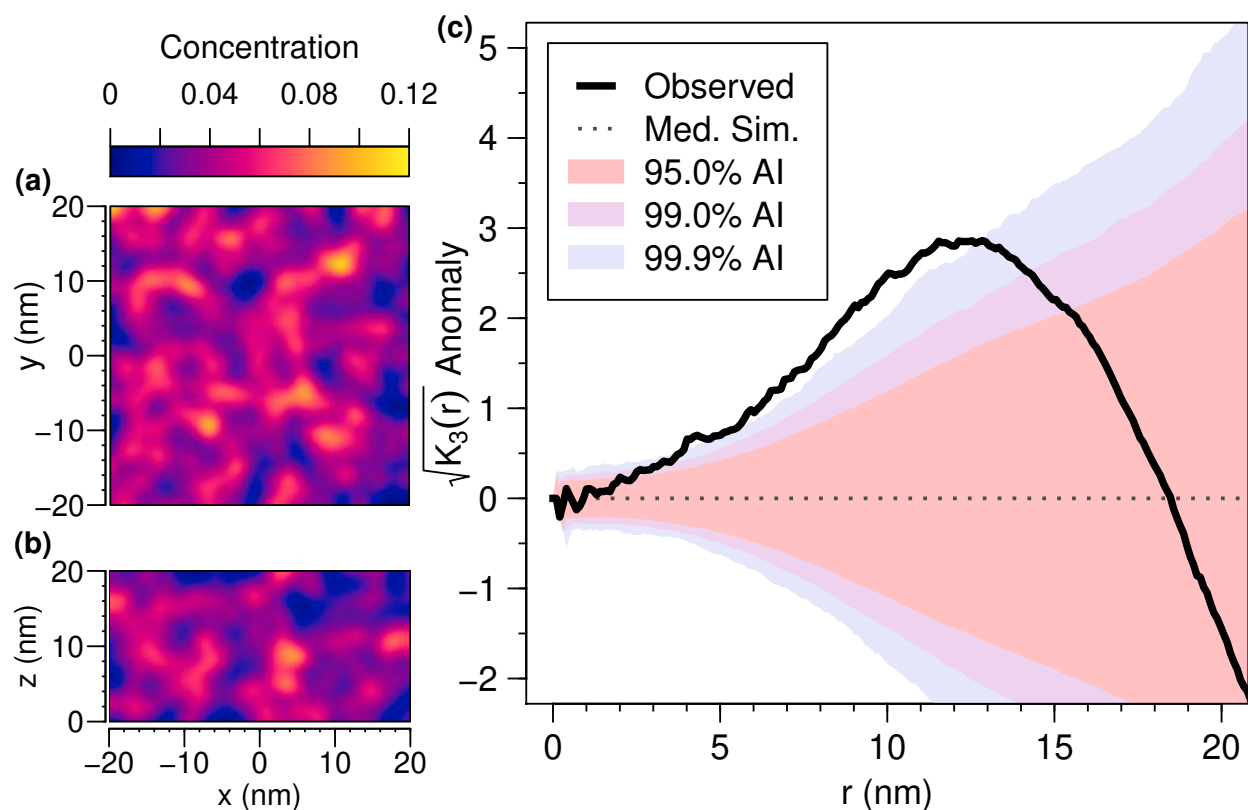


Figure 4.6: Heat maps showing the concentration (fraction) of Ir(ppy)<sub>3</sub> in a  $40 \times 40 \times 20$  nm box projected onto (a) the x-y plane and (b) the x-z plane. Three-dimensional renderings of the volume projected are shown in Figure 4.5a,b. (c) Transformed K-function anomaly for Ir(ppy)<sub>3</sub> in this box along with simulation envelopes. The excursion of the observed K-function above the envelopes indicates significant (deviation outside a 99.9% acceptance interval) clustering of the Ir(ppy)<sub>3</sub> in the range of about 5 to 12 nm. Adapted with permission from *Chem. Mater.*, 2019, **31** (7), pp 2241-2247.[54] © 2019 American Chemical Society.

### 4.3 Degradation

Understanding the degradation of OLEDs is a key area of research and development crucial to their continued commercial success. Displays, which comprise the majority of the OLED market, are particularly susceptible to degradation because the rate varies with emission wavelength; as might be expected, devices that emit higher energy photons tend to degrade more quickly.[62, 118] There are a variety of mechanisms that can lead to degradation of organic semiconductors, both intrinsic and extrinsic, each with their own physics and signatures.[17, 20, 21, 62]

While extrinsic mechanisms are at this point mostly the realm of the process engineer, intrinsic mechanisms can reveal a lot about the fundamental nature of the molecular system.[62] Two intrinsic mechanisms of importance to phosphorescent OLED systems are TPQ and TTA; each of these can dump enough energy into the molecule on which they occur that it can break bonds, leading to chemical changes in the material.[62, 118, 119] In addition, unimolecular degradation—where a single exciton decay can chemically alter a molecule—can be a contributing factor in higher energy OLED emitters.[118] These fragments or adducts can act as traps or recombination sites, reducing efficiency or changing the emission profile.[118, 120, 121]

Knowing the identity of degradation products is valuable, but their environment must also be considered. If the material is in a meta-stable state, morphological changes can cause performance degradation in their own right; by adding sufficient numbers of excitons, enough energy can cause molecular positions to relax and alter the transport and recombination properties of the system.[10, 19, 20, 122] For chemical changes, the environment of the affected molecule is critical to understand its impact on the device, as the reactions can have multiple steps to get to a stable (irreversible) product,[62, 123, 124] or have the reaction driven by the presence of another molecule.[121]

There are a number of ways to inject excitons into an OLED to study how it degrades. While the most obvious is device operation, this adds more complexity to the system by en-

abling all potential degradation pathways, which makes it challenging to determine precisely what mechanisms are at work. Light exposure works to inject excitons as well, provided the photons are sufficiently energetic; this method has the advantage that it does not require a full device stack, allowing a component material to be isolated.[122] Because TPQ requires current injection to generate the polaron, light exposure avoids this degradation channel, reducing the mechanisms to only TTA and unimolecular degradation pathways.[118] This enables focused study on these processes, which helps deconvolve degradation signatures in electrically operated devices.[23, 118, 119, 121]

For investigating pure photodegradation—either TTA or unimolecular degradation—APT has a natural advantage because it can do the measurement and exposure *in situ* under ultra high vacuum (UHV) by using the UV laser pulses for evaporation to expose the sample as well. This isolates the exciton degradation pathway by avoiding extrinsic sources of degradation (*i.e.* without worrying about water or oxygen). Furthermore, the pulses are already well-controlled, meaning that the exciton density (*i.e.* pulse energy) and total dose are separately adjustable and stable. This allows us to determine threshold exciton densities for degradation as well as equilibrium concentrations; De Moraes et al., *e.g.*, found that certain reactions were dependent on current density, while others depended on total current, which is analogous to the dose/pulse energy control we have with APT.[18]

The Local Electrode Atom Probe<sup>TM</sup> 4000X Si (LEAP) can sweep pulse energies through  $1 \times 10^{-3}$  to  $1 \times 10^3$  pJ using a Spectra-Physics Vanguard 355-350 laser, which can pulse at repetition rates of up to 80 MHz at a wavelength of 355 nm.[65] Though the beam has a known gaussian profile with a diameter of  $3 \mu\text{m}$  ( $4\sigma$ ), the sample exposure cross-section is not known, so absolute values for excitons in the sample can only be loosely estimated;[65] regardless, the LEAP should easily be able to access the exciton densities at which TTA is expected.[125] Additionally, the relative changes in exciton density should be fairly accurate, which allows us to establish a hierarchy of degradation products.

To begin, we examined films of neat Ir(ppy)<sub>3</sub>, a prototypical green phosphorescent OLED emitter molecule which we have previously studied.[54] We prepared thin films of Ir(ppy)<sub>3</sub> using vacuum thermal evaporation at room temperature, using rates of 1 Å s<sup>-1</sup> to a thickness of 100 nm; the film thickness and doping ratios were controlled by the deposition rate, monitored by a quartz crystal oscillator. These films were deposited on Si tips with a nominal 250 nm radius of curvature.

For APT analysis, all samples were measured at 25 K with a laser pulse energy of 8 pJ running at 250 kHz. Each run collected data for 500 × 10<sup>3</sup> ions. For UV dosing, the samples were exposed under minimal bias (*i.e.* 500 V, the minimum voltage for operating the LEAP) at 10 MHz.

The preliminary degradation series sweeps through 10 to 40 pJ in 10 pJ steps maintaining constant dose (*i.e.* pJ · s = *const.*). These energies were chosen because the standard pulse energy established in Chapter 3 sits at the low end of this range. Each pulse energy was exposed twice to help distinguish products that depended on dose from those that depended on exciton density; the dosing series is given explicitly in Table 4.2. Figure 4.7a shows the mass spectra collected from this series. There are clear changes in some peaks as the dose and energy increases.

Table 4.2: The doses applied for the UV degradation series. Each exposure was performed under minimal bias (*i.e.* 500 V, the minimum voltage for operating the LEAP) at 10 MHz.

<b>Time (min)</b>	<b>Pulse Energy (pJ)</b>	<b>Normalized Dose (arb.)</b>
0.0	0	0
6.0	10	1
6.0	10	2
3.0	20	3
3.0	20	4
2.0	30	5
2.0	30	6
1.5	40	7
1.5	40	8

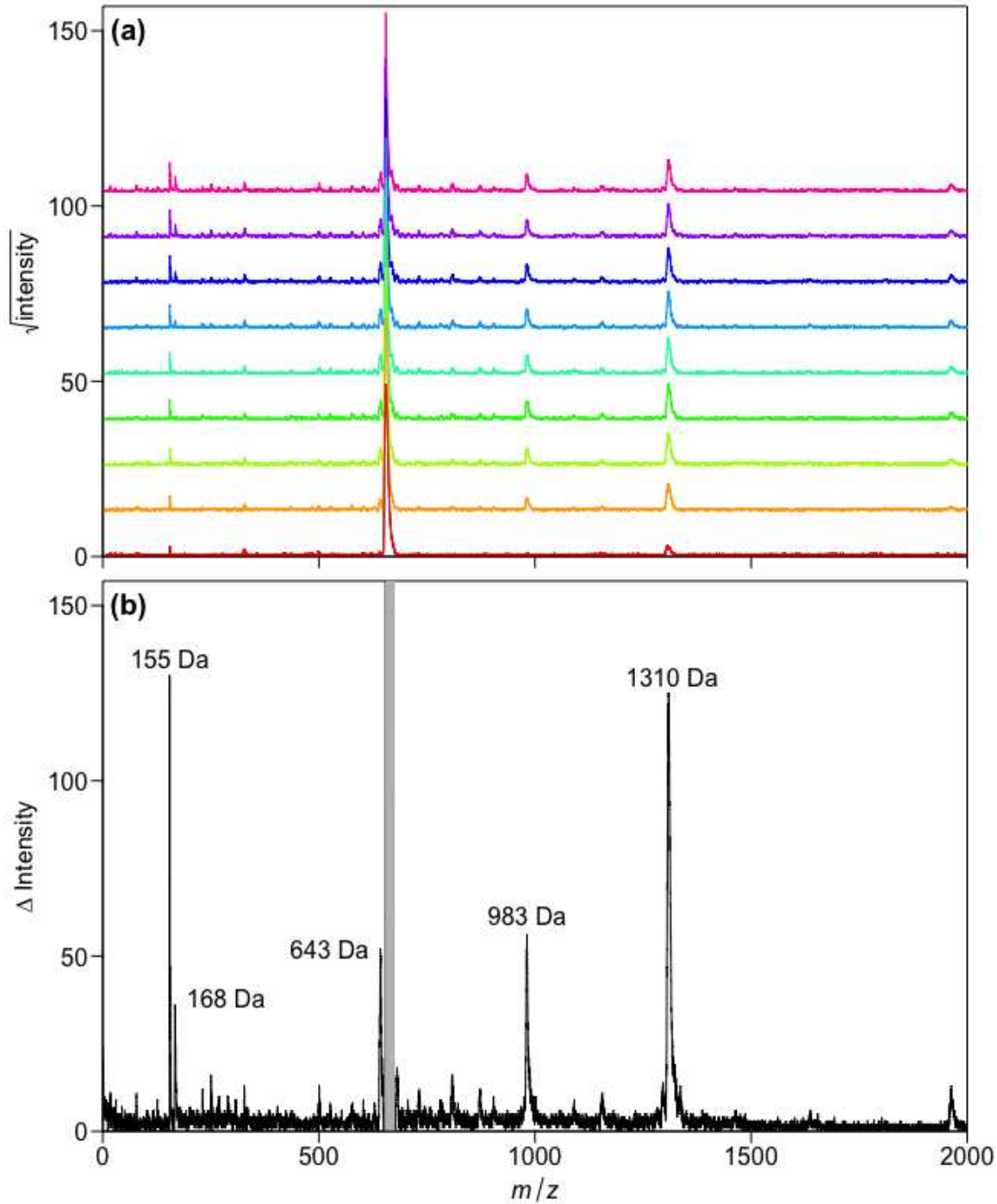


Figure 4.7: (a) Mass spectra of the degradation series. The dose increases vertically. (b) The change in intensity of the mass spectra between the first and last spectrum; the grey bar cuts an artifact from taking the difference between the large main Ir(ppy)<sub>3</sub> peaks. Five peaks stand out as changing significantly between the pre- and post-exposure mass spectra: 155, 168, 643, 983, and 1310 Da.

To highlight the differences between the exposures, Figure 4.7b shows the difference between the first and last spectrum. This difference shows five major peaks that appear as the sample is exposed to the laser, which are at approximately 155, 168, 643, 983, and 1310 Da. Certain of these masses are easily identified: 155 Da is 2-phenylpyridine (ppy), 983 Da is tris-Ir(ppy)<sub>3</sub><sup>++</sup> (the peak at 1966 Da in Figure 4.7b is tris-Ir(ppy)<sub>3</sub><sup>+</sup>), and 1310 Da is bis-Ir(ppy)<sub>3</sub><sup>+</sup>. However, the peaks at 168 and 643 Da are not readily identifiable.

To measure changes in composition, each peak must be ranged. This is slightly trickier than it might seem because choices for ranging can vary significantly, changing measured ion concentrations.[65] Because time-of-flight (TOF) adjustments to APT data do not perfectly calibrate the spectrum across all masses, a single set of ranges for all the data sets can lead to compositional inconsistencies. For these data sets, each peak was ranged individually, using a range cut off of 1/5 of maximum peak intensity. This uniformly applied criterion improves the consistency of analysis.

Figure 4.8a,b shows how these five peaks change with the total dose: (a) shows the concentration of the ion in the sample, and (b) shows the fractional change in the ion concentration relative to the unexposed spectrum. In Figure 4.8a, the unknown peak at 643 Da very closely tracks the tris-Ir(ppy)<sub>3</sub><sup>++</sup> peak; in fact, a linear fit of their sample concentrations (Figure 4.9) shows that the concentrations are the same to within the fitting error ( $0.965 \pm 0.073$ ,  $R^2 = 0.962$ ). This strong relationship suggests that these two ions arise from the same process.

In Figure 4.8b, the 168 Da ion has a very different behavior as compared to the others, increasing dramatically after four normalized doses. This can be explained by looking at the fractional change in concentration with energy as shown in Figure 4.10. This clearly shows that the 168 Da ion has a threshold pulse energy for formation between 20 and 30 pJ. The other ions, however, do not show any evidence of a threshold.

The apparent lack of threshold energy for most of the identified ions in the series requires that we use lower pulse energies to look for the threshold; however, the pulse energy for

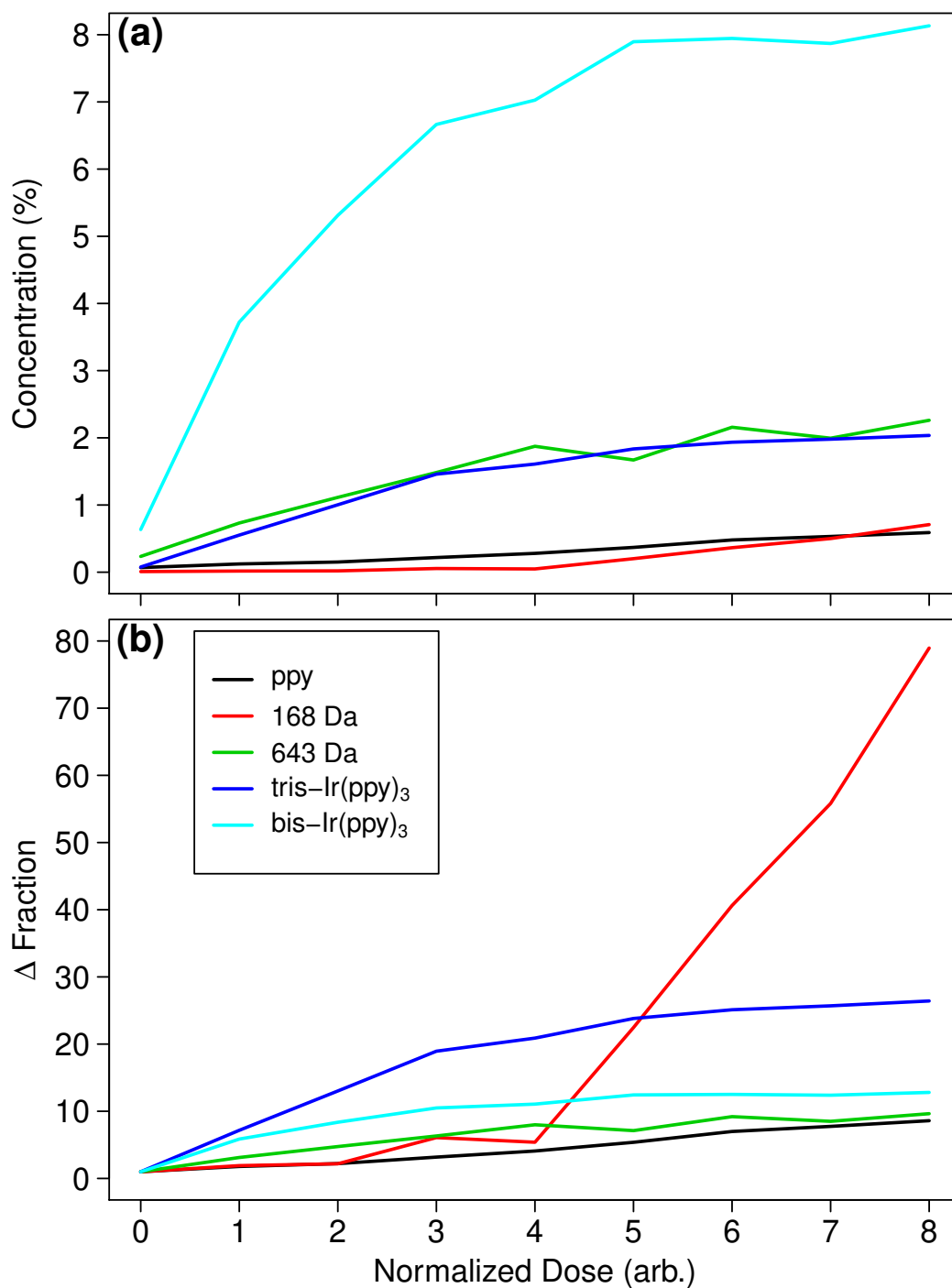


Figure 4.8: (a) Change in concentration of the five species with the dose ( $\text{pJ} \cdot \text{s}$ ). Because all spectra are collected on the same sample, the pulse energy changes as dose increases as well. The concentration of the ion at 643 Da tracks closely with the concentration of  $\text{tris-Ir(ppy)}_3$ . (b) Fractional change in concentration of the five species. The ion at 168 Da (red) shows odd behavior compared to the others; this can be explained by a threshold exposure energy as shown in Figure 4.10.

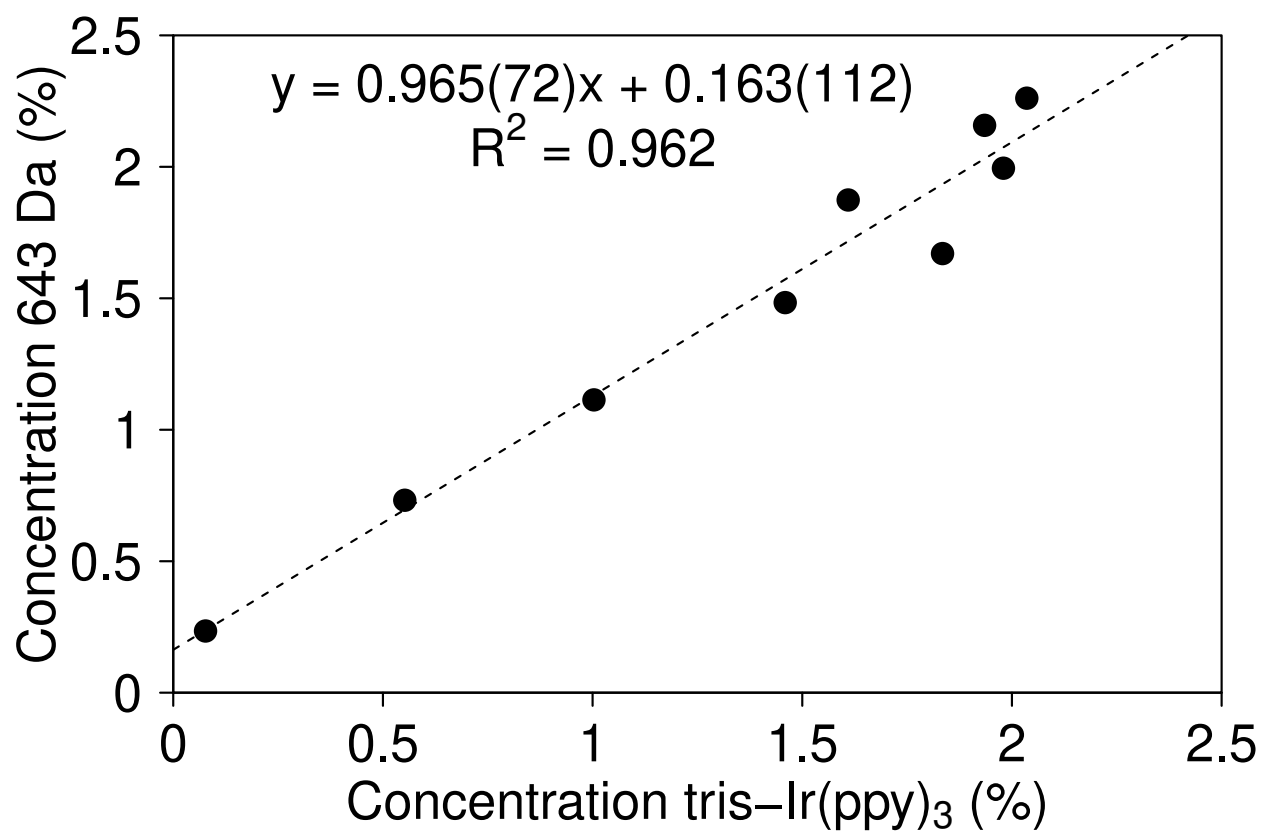


Figure 4.9: Correlation between the concentration of the tris-Ir(ppy)<sub>3</sub><sup>++</sup> peak and the unknown ion at 643 Da. They vary in a 1:1 fashion to within the error of the fit ( $0.965 \pm 0.073$ ,  $R^2 = 0.962$ ), suggesting that these two ions arise from the same process.

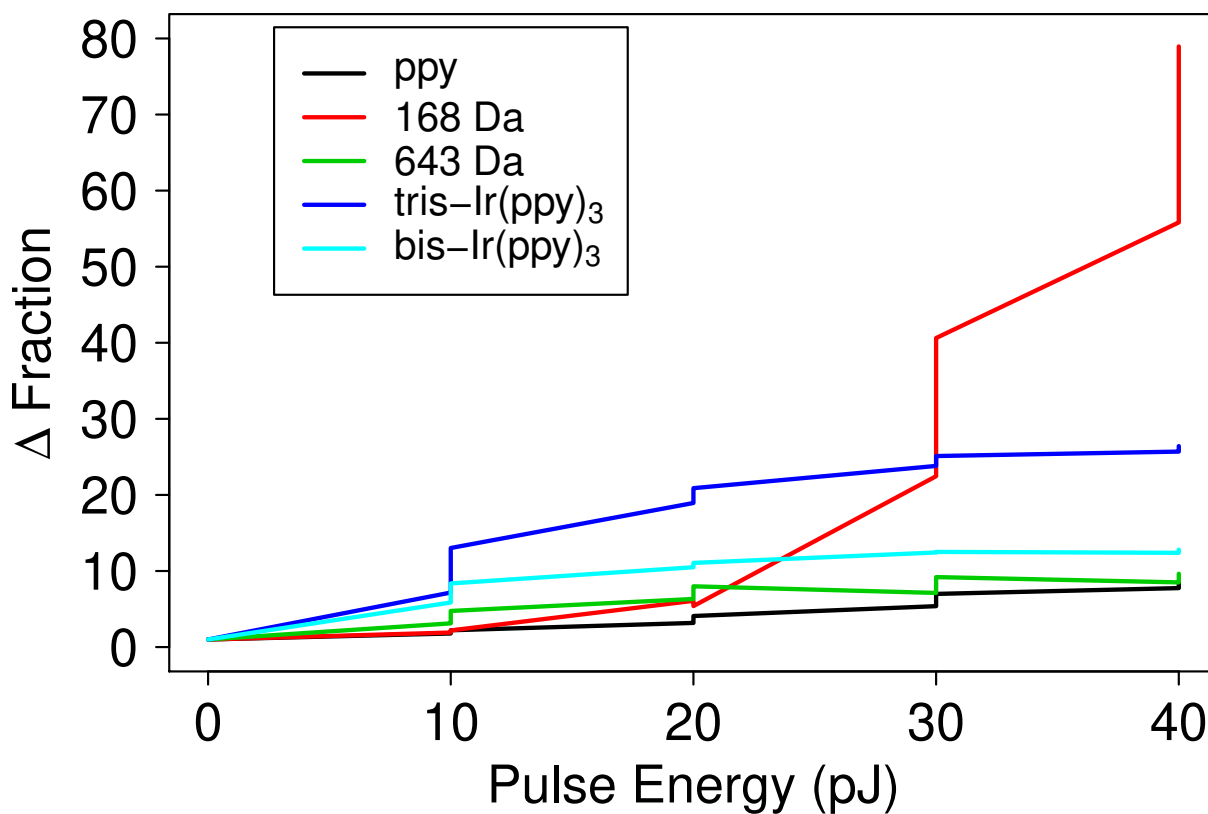


Figure 4.10: Fractional change in concentration of the five species. This clarifies the different behavior of the ion at 168 Da seen in Figure 4.8: the ion only appears at a threshold pulse energy between 20 and 30 pJ. None of the other ions appear to exhibit such a threshold at the energies tested.

the preceding APT analysis was 8 pJ, meaning that the analysis energy could be above the threshold for these ions to appear and has the potential to influence the results. As pulse energy is changed, it impacts both mass resolving power (MRP) and spectral sensitivity, so selecting a new pulse energy for APT analysis must be balanced with other considerations.[65]

Figure 4.11a shows how the MRP varies as a function of pulse energy; these values were determined by fitting a series of gaussians with equal standard deviations to the primary Ir(ppy)<sub>3</sub> peak. This shows that the MRP improves as the analysis pulse energy is decreased to a point, then hits a floor at  $\sim 1$  pJ. Counter to this, Figure 4.11b shows how the spectral noise (estimated from an integrated visualization and analysis software (IVAS) algorithm) varies in the opposite way with with the pulse energy: to minimize noise, a higher pulse energy should be chosen. To balance the two competing requirements of MRP and spectral sensitivity, we select an analysis pulse energy of 1 pJ to look for threshold energies (*i.e.* exciton densities) for the observed products not exhibiting the clear energy threshold of the ion at 168 Da; the MRP and noise character of this pulse energy is shown by the points circled in green in Figure 4.11b.

Figure 4.12 shows the difference between two unexposed samples, one run at the 10 pJ (“high”; black) pulse energy and the other at the 1 pJ (“low”; red) pulse energy. The noise and MRP in the low energy spectrum changes as expected from Figure 4.11b. Additionally, due to the change in evaporation conditions, the low energy spectrum has about an order of magnitude larger Ir(ppy)<sub>3</sub><sup>++</sup> component as compared to the high energy spectrum. Overall, the low energy spectrum has fewer features than the high energy one; in particular, there is no sign of the bis- or tris-Ir(ppy)<sub>3</sub> at the lower pulse energy. The ppy peak, however, is still present at approximately the same concentration, after accounting for the noise difference between the two run conditions. This suggests that the lower pulse energy is below the threshold energy for the peaks besides ppy identified in the degradation series of Figure 4.7.

Because the unexposed APT spectrum collected at 1 pJ does not show as many potential degradation products, the sample was then exposed at 1 pJ for 6.4 min at a pulse repetition

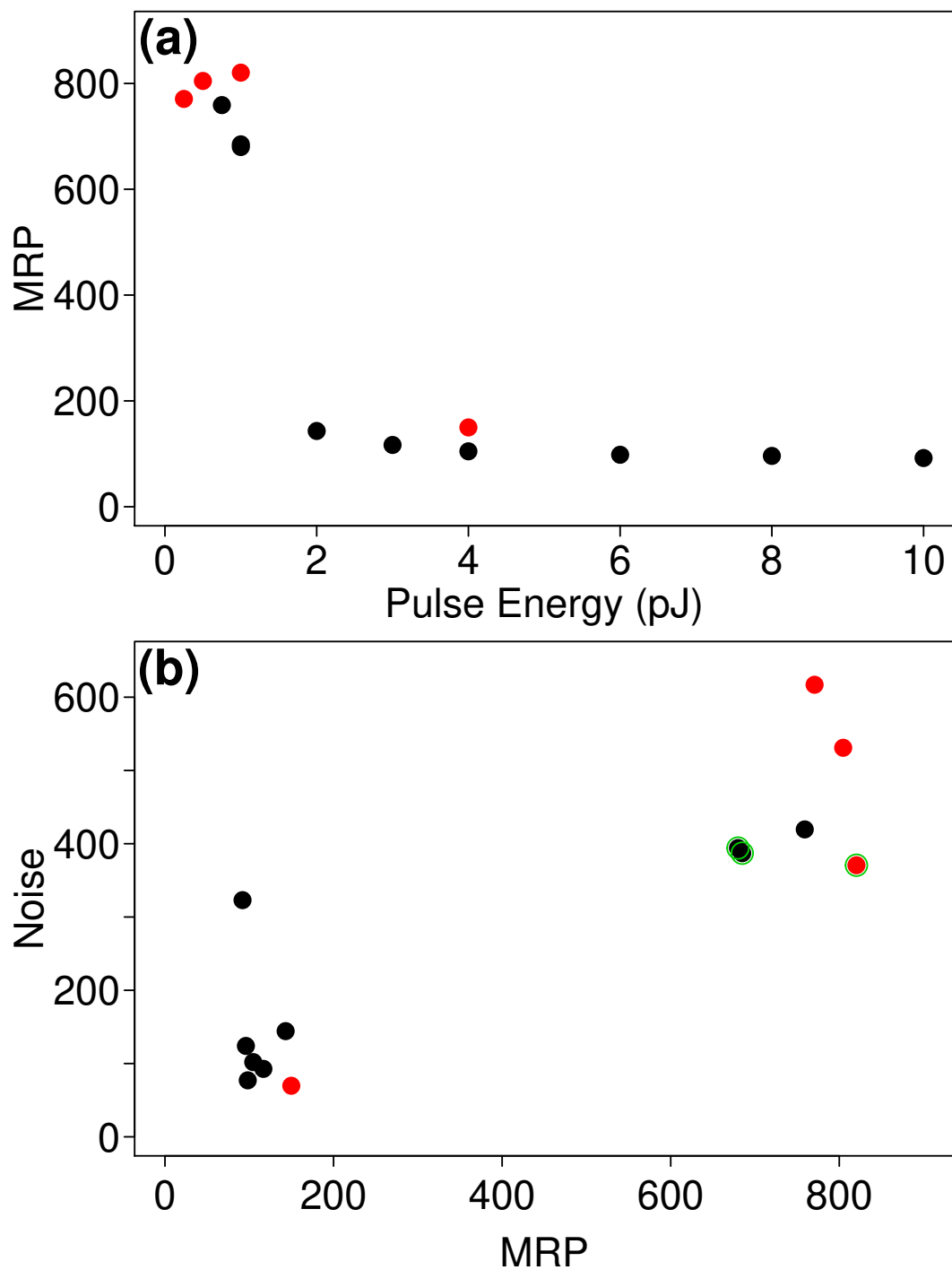


Figure 4.11: (a) MRP of the APT spectra as a function of pulse energy, calculated by gaussian fits to the primary Ir(ppy)<sub>3</sub> peak. As pulse energy decreases, MRP improves up to ~ 1 pJ, and is flat afterward. (b) Spectral noise versus MRP for the APT runs at different pulse energies. There is a clear trade-off between the two.

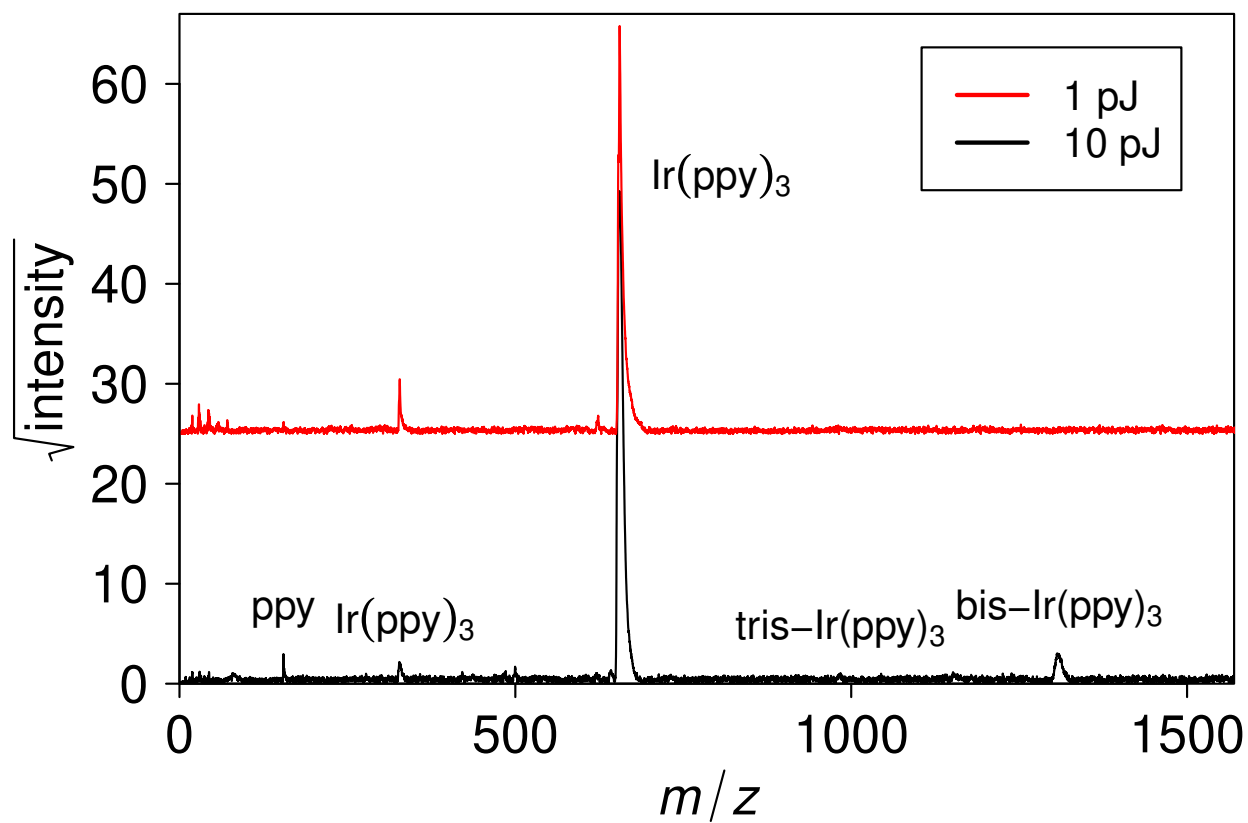


Figure 4.12: Change between unexposed samples analyzed at 10 pJ (black) and 1 pJ (red). The 1 pJ spectrum shows fewer peaks, though the ppy peak at 155 Da is still present at approximately the same concentration in both.

rate of 40 MHz; the total dose is about half that of the first exposure in Figure 4.7a. Figure 4.13a compares the APT mass spectra before and after this exposure. No new peaks are obvious, and the region above the mass of the  $\text{Ir}(\text{ppy})_3^+$  peak appears essentially featureless in both. Comparing this to the high pulse energy case, at this dose we would expect to see a bis- $\text{Ir}(\text{ppy})_3$  peak at  $\sim 1\%$  concentration (*cf.* Figure 4.8a). Instead, taking a difference between these two spectra (Figure 4.13b) reveals that there is essentially no change between these two spectra other than an approximately two-fold increase in ppy, which is consistent with its change with dose in the high energy series (*cf.* Figure 4.8b).

In fact, the most notable feature of Figure 4.13b is how high the noise is: it is considerably elevated across all masses in the exposed sample. Looking at the two data sets, the  $\text{Ir}(\text{ppy})_3^+$  peak comprises only 32 and 29% of the total ions collected for the unexposed and exposed runs, respectively. Compare this to the unexposed sample measured at high pulse energy, which has this peak totaling 75% of the total ion count.

Clearly, more work is needed to optimize and control for all the variables in these experiments, but the results are promising. While not all of the major peaks that arise from UV exposure were identified, correlations with known peaks suggest other ways of teasing out the information such as higher MRP through a longer flight path (*i.e.* 160 mm) or spatial correlation on a larger data set. In addition, we have demonstrated the capability to identify an approximate threshold exciton density of 20 to 30 pJ for the (as yet unknown) peak at 168 Da, and were able to adjust the run conditions to drop below the threshold of most of the others. While the lower analysis pulse energy is not yet optimized, the data quality is still good enough to conclude that most of the investigated peaks are unlikely to have an appreciable concentration in an unexposed film; the starting concentration of the ppy peak (if any), however, is still unclear. These results already provide new information to the OLED community, which has had challenges analyzing chemical composition and degradation products.[62, 80] By extending these studies to materials systems (*e.g.*  $\text{Ir}(\text{ppy})_3\text{:CBP}$ ), the locations of these products and their molecular environment can help uncover particular

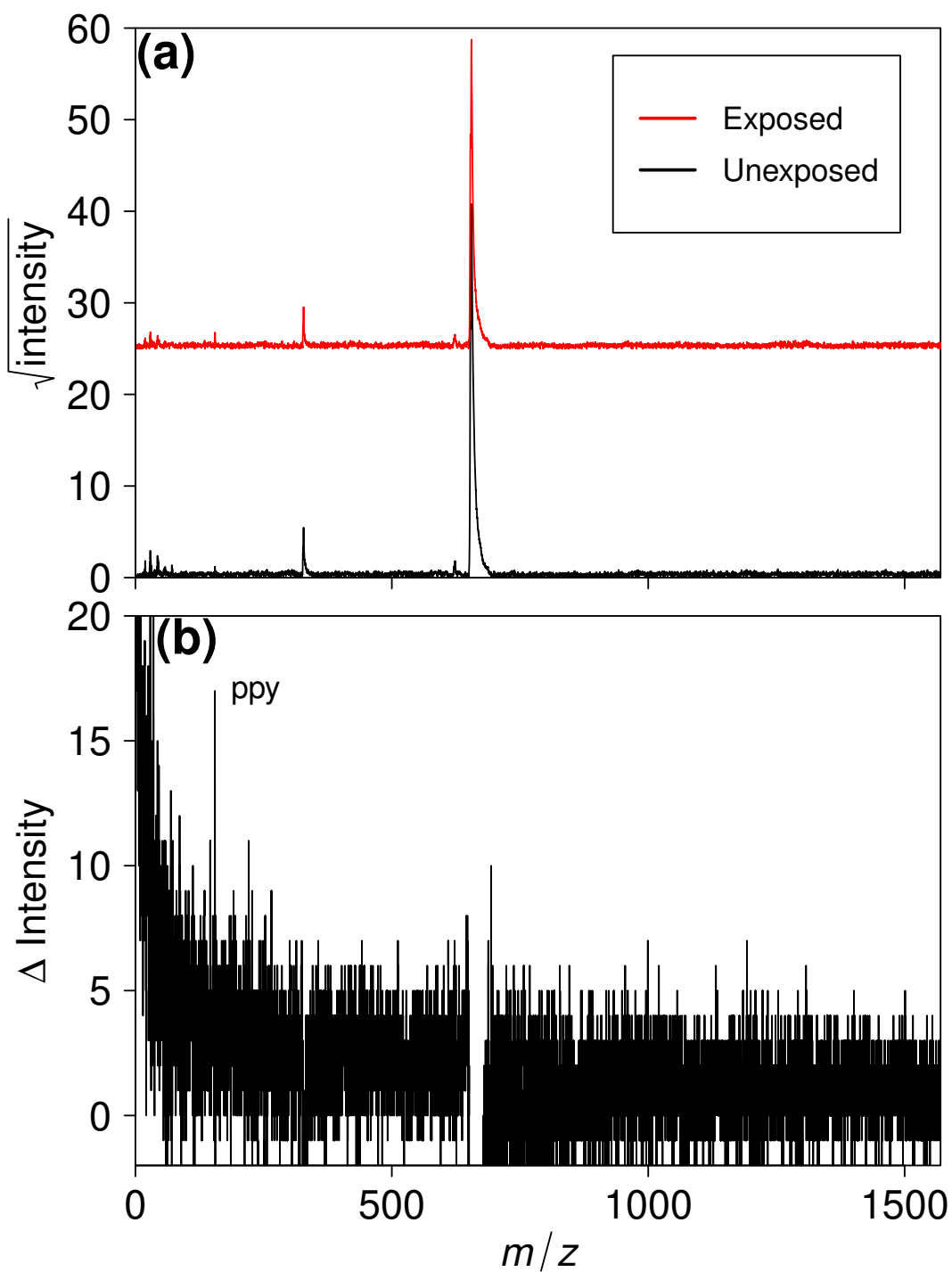


Figure 4.13: (a) Mass spectra of the unexposed (black) and UV exposed (red) samples. Other than the ppy peak at 155 Da, none of the other ions from the higher energy series (Figure 4.7) are apparent. The amount of ppy approximately doubles. (b) The change in intensity of the mass spectra between the first and last spectrum; only the ppy peak appears to have increased after the dose.

degradation pathways.

APT provides a wealth of information about small-molecule organic semiconducting systems that enable new scientific insights. Whether through high resolution spatial information about critical device locations or progressive experiments to investigate intrinsic processes in materials, APT is an invaluable new tool for the organic semiconductor community. With continued development these results can be improved upon, permitting even more discoveries with the help of APT.

## CHAPTER 5

### RECONSTRUCTION

*We are often interested in micro-structural features such as precipitates, interfaces, voids and grain boundaries, and it is exactly these chemical or structural heterogeneities that most strongly affect the sequence in which atoms are field evaporated in atom probe tomography.*

–Larson et al. [126]

A unique advantage of atom probe tomography (APT) is its ability to provide precise mass information (*i.e.*  $< 1$  Da) over volumes of thousands of cubic nanometers with a three-dimensional spatial resolution of  $< 1$  nm.[40] This ability depends critically on the reconstruction process used to convert the raw data into its final form for analysis: the method must be accurate yet fast enough to work on a typical APT dataset containing millions of ions.[65] Here, we develop a method that works over complete APT data sets and provides a measure of the uncertainty in the reconstruction and any analyses derived from it.

Currently, the vast majority of reconstructions fundamentally rely on the point-projection work of Bas *et al.*[43] This method is fast, but suffers from spatial resolution inaccuracies such as ions being placed unphysically close or unphysical voids or variations in the sample shape because of its assumptions about both the sample geometry and ion trajectories.[65, 72, 127, 128] Other approaches have been suggested that greatly improve the accuracy of reconstruction, but either require substantial computational cost[129] or additional measurements of the sample.[130–132] Furthermore, high accuracy reconstructions use the crystal structure of the material being imaged as an internal fiducial, which only works on systems with a high degree of crystallinity.[133–136] Correlative transmission electron microscopy (TEM) imaging of the sample before (and after) atom probe analysis can bound the global

reconstruction volume even without a crystalline sample;[130, 131] however, this excludes those systems that are sensitive to electron radiation.[54]

In all these methods, considerable attention has been paid to the higher resolution z dimension of reconstruction—which is capable of resolving lattice planes in crystalline samples[63, 137]—while markedly less work has been done on the xy dimension of the reconstruction. As the resolution of the technique is known to be worse in xy due to, *e.g.*, trajectory aberrations,[63, 138, 139] the uncertainty in the lateral dimension of the reconstruction merits further attention.[42, 63, 136] When xy correction has been done, it is in the context of a known crystal structure onto which the points may be coerced.[63, 133, 135] However, when working on amorphous and nanocrystalline systems other methods for adjusting xy point position are necessary to realize APT’s full potential.[1, 54, 140]

Furthermore, current reconstruction techniques and analyses derived from them do not have an associated uncertainty; reconstruction methods usually generate only a single, user-directed reconstruction that can be laborious to compare to another created from a different set of inputs. As a result, APT experiments generally base conclusions off of a single reconstruction without stating a statistical confidence.[136] Ideally, claims based on atom probe data should have some form of explicit uncertainty associated with them to help evaluate the significance of the result. Stating this uncertainty is particularly important because many sets of parameters can generate reconstructions that satisfy the constraints typically known by researchers. Work has been done to characterize the spatial accuracy of a reconstruction, but it is limited by the existence of significant independent knowledge of the sample (*e.g.* crystal structure).[136]

In this chapter, we develop a reconstruction method that provides a solution envelope, increasing confidence in the conclusions drawn from the data regardless of the exact solution. This method does so without needing measurements of the sample other than APT. We explicitly account for the lower x-y resolution by shifting points in x & y, which incorporates this uncertainty into subsequent analyses. This adjustment is determined by solving the well-

studied Assignment and Exact Cover Problems for slices of data in detector space;[141, 142] this process can also constrain the reconstruction to maintain density and minimum particle spacing. We may then use the resultant solution sets to determine the robustness of the morphological signal as compared to a null hypothesis of random labeling using the tools of spatial statistics. We evaluate this method using simulated APT data containing small ( $\sim 0.7$  nm diameter) clusters of B in a random close packed (RCP) matrix of Si, showing that it recovers the clustering signal better than a standard reconstruction with parameters based on minimizing the positioning error relative to the input pattern. By outperforming the error-minimized standard reconstruction, this new reconstruction demonstrates its value in correcting for near-field aberrations in APT data.

### 5.1 Source-Sink Process

Our reconstruction method relies on the common assumption of well-ordered evaporation, which is valid for the vast majority of APT data and can give outstanding resolution in the  $z$  dimension.[65] Fundamentally, it systematically adjusts points in  $x$  &  $y$  within some particular slice of  $z$  to account for the  $x$ - $y$  uncertainty while obeying a physically motivated minimum point spacing. These adjustments provide the basis for generating an ensemble of reconstructions that can be used to create uncertainty envelopes for subsequent analyses.

To begin, the detector is divided into bins as shown in Figure 5.1a. Because the detector itself is gridded, this imposes no further structure on the data. We choose to bin based on a physically relevant length scale of the material (*e.g.* a bin spacing that is the projection of a 1 nm  $xy$  spacing at the apex of a 300 nm radius tip for a small-molecule organic sample where the molecule diameter is approximately 1 nm). For simplicity, we choose a square grid of bins, but any pattern that covers the region of interest on the detector will work.

To generate the slices, hits (*i.e.* detection events) within the region of interest are ordered by their sequence of detection and divided into equal slices containing the exact number of bins on the detector.

Within each slice, each bin will contain varying numbers of hits. We identify those bins with multiple hits as “sources” and those with no hits as “sinks” and determine a mapping from sources to sinks as shown in Figure 5.1b. This mapping should minimize the total movement of points, which means that our cost function for the optimization is the distance from each source to each sink. By minimizing this cost function, we find our optimal mapping; this optimization problem is known as the Assignment Problem.[141]

Directly relocating source points to sinks does not, however, account for point relocation uncertainty. Instead, we define neighborhoods of possible participants around the source-sink mapping, illustrated schematically in Figure 5.1c; because these can overlap, the individual neighborhoods must be combined to create the full interaction neighborhood for each source-sink assignment (Figure 5.1d). We then define the possible motions of each point within the neighborhood, which ensures that no point in the neighborhood is moving non-locally and its movement is constrained. With the neighborhoods and local motions defined, we enumerate all the configurations of the points such that there is one and only one point per bin. Such a problem is known as an Exact Cover Problem.[142] The set of configurations thus obtained can be used to create an envelope for analysis to quantify uncertainty.

This source-sink reconstruction procedure requires significantly more computation than the standard reconstruction method. However, there are a number of ways to reduce the effort required.

Because of the large number of assignments that must be made, we take advantage of a GPU-optimized Assignment Problem implementation to drastically speed up this process.[143] The Exact Cover step, while not itself parallel, is repeated over many neighborhoods, each of which can be evaluated in parallel.

In addition to improving computational resources, improvements can be made on the inputs to reduce load. Because the number of ion species is small relative to the number of hits in an APT data set, a significant computational efficiency gain can be realized by eliminating configurations with the same identity in all locations. This reduces the search

**(a)**

1	1	1	1	1	1	1
2	1	1	0	1	2	0
1	0	1	1	1	2	1
1	1	1	1	1	0	1
1	2	0	1	0	3	1
1	0	1	1	1	0	1
1	1	2	1	1	1	2

**(b)**

1	1	1	1	1	1	1
2	1	1	0	1	2	0
1	0	1	1	1	2	1
1	1	1	1	1	0	1
1	2	0	1	0	3	1
1	0	1	1	1	0	1
1	1	2	1	1	1	2

**(c)**

1	1	1	1	1	1	1
2	1	1	0	1	2	0
1	0	1	1	1	2	1
1	1	1	1	1	0	1
1	2	0	1	0	3	1
1	0	1	1	1	0	1
1	1	2	1	1	1	2

**(d)**

1	1	1	1	1	1	1
2	1	1	0	1	2	0
1	0	1	1	1	2	1
1	1	1	1	1	0	1
1	2	0	1	0	3	1
1	0	1	1	1	0	1
1	1	2	1	1	1	2

Figure 5.1: Illustration of the assignment and neighborhood definition process: (a) detector hits are binned and counted; (b) assignments are made from bins with multiple hits to bins with no hits, minimizing the total distance; (c) individual neighborhoods are defined by surrounding each assignment; and (d) overlapping neighborhoods are combined to determine the final interaction neighborhood.

space exponentially, leading to a significant time savings.[142] While this simplification does technically affect the reconstruction envelopes, the impact on the interpretation is negligible.

Another way to improve the execution time of the exact cover enumerations is by limiting the size of the neighborhoods. Interaction neighborhoods defined by the source-sink assignments commonly overlap and their union should be analyzed; however, in practice this leads to prohibitively large neighborhoods to evaluate. For simplicity, we threshold the total number of configurations to prevent excessive run times; more sophisticated methods of neighborhood reduction remain an interesting avenue of exploration. Taken together, these optimizations permit this method to be used on complete APT data sets using relatively modest computational power.

Once the set of solutions has been determined in detector space, the data are reconstructed into three-dimensional sample space. The positions specified to this point are independent of the method used for reconstruction, and so we are free to select any reconstruction method we wish. For the following, we choose to proceed with the common point projection method for simplicity as it is fast and not the core result of this work.

Because detector hits are already binned on the detector, we can use these bins to modify the reconstruction slightly: instead of a simple global  $z$  increment for each point in the pattern, we can use the bins to increment point  $z$  positions within the bin based upon the point identity. This, combined with our choice of bin selection above, enforces a minimum inter-point spacing, which improves the physicality of the reconstructions.

This process results in a set of reconstructions bounded by physically informed limits. By performing analyses over this ensemble, an uncertainty naturally follows.

## 5.2 Spatial Signal and Testing

Spatial statistics is a useful toolset for analyzing APT reconstructions. It has had some use within the community, but wider adoption will allow for more advanced spatial analyses that can describe the significance of an observed effect.[54, 63, 67, 144, 145] Common functions used for analyzing point patterns are the G-function—a cumulative distribution

function of nearest neighbor distances—and the K-function—the expected number of points residing within a sphere of radius  $r$ , normalized by the pattern intensity (see Chapter 2).[73] These functions summarize the behavior of the point pattern globally (*i.e.* its average behavior at some range of length scales), which, in combination with confidence envelopes generated by Monte Carlo methods, allow for statistically significant conclusions to be drawn from analyzing a single experimental data set.[73, 79]

The first hypothesis to test is that of spatial randomness. Because there is inherently some structure to the points in an APT reconstruction, we test not for complete spatial randomness of the points themselves, but instead that the identities of the points have been randomly assigned, called the random labeling hypothesis (see Chapter 2).[73] This can be tested using Monte Carlo methods by randomly relabeling all the points in the dataset and comparing the envelope of random relabeling values to that of the actual dataset. This analysis allows us to investigate whether the dataset has spatial structure, such as clustering.

While looking at deviations outside the relabeling envelopes for a particular summary statistic (*e.g.*  $G_3$ ) is a good indicator of behavior (*e.g.* clustering), the functions also permit formal significance tests. The Diggle-Cressie-Loosmore-Ford (DCLF) test is one such test that uses the squared deviation of the function from that expected under the null hypothesis; specifically, for a summary function  $H(r)$ : [146]

$$T = \int_a^b (H(r) - H_0(r))^2 dr \quad (5.1)$$

This allows us to formally test for significant departure of the observed function ( $H$ ) from the null hypothesis ( $H_0$ ) in the range  $a \leq r \leq b$  by comparing values of the test statistic  $T$ .

### 5.3 Methods

The simulated sample uses a random close packed pattern with a point radius of  $1 \text{ \AA}$  and evaporation field values corresponding to Si and B ( $33$  and  $64 \text{ V nm}^{-1}$ ); [63] these large field differences are known to cause significant “chromatic aberration” in APT due to local magnification effects. [65, 66, 138] Clusters of B were generated in a matrix of Si using ran-

domly selected seeds and choosing each of their 9 nearest neighbors as cluster points, which gives the clusters a diameter of  $\sim 0.7$  nm. The number of clusters was chosen to make them 3% of the total sample. The sample contains 601 602 Si and 18 374 B ions in a cylinder with a radius of 7 nm and a height of 27 nm. A rendering of the cluster points is shown in Figure 5.2.

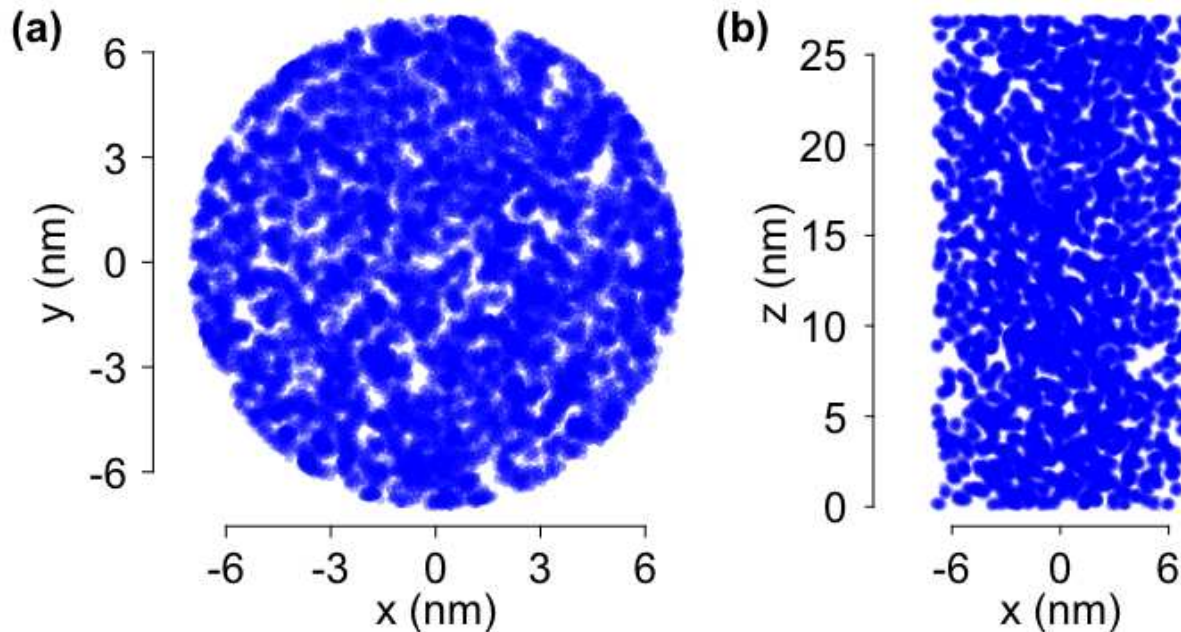


Figure 5.2: The clusters of the input pattern viewed (a) along the axis of the cylinder and (b) from the side of the cylinder. Each cluster contains 10 points—giving them a diameter of  $\sim 0.7$  nm—and they comprise 3% of the total sample.

Field evaporation was simulated using TAPSim with standard parameters for the simulation mesh, node values, and evaporation; [139] the configurations are given in Appendix A. The resultant evaporation data were then clipped to remove the first and last 100 000 events, allowing the sample to achieve its equilibrium end form and keeping out events occurring near the simulation boundary.

The standard reconstruction was chosen by reconstructing across a range of parameters (*i.e.* sample radius ( $R$ ), image compression factor (ICF), and density ( $\rho$ )) and selecting the reconstruction that minimized the position error. The minimum error reconstruction has a

median position error of 0.463 nm, with  $R = 7.5$  nm,  $ICF = 1.00$ , and  $\rho = 147$  nm<sup>-3</sup>.

For the source-sink reconstruction, the detector was binned using a bin width of 0.2 mm, which corresponds to a tip radius of 10.5 nm based on a simple point projection of the 2 Å point diameter for the simulated 10 cm flight path. This led, after assignment and neighborhoods aggregation, to 1757 neighborhoods; removing neighborhoods with only one label type reduced this number to 521 neighborhoods with a maximum size of 113 bins. Point motion was limited to “rook”-type motion, which is directly adjacent movements excluding diagonals. For the source-sink method, a configuration cutoff of 120 was used, which reduced the number of neighborhoods for the Exact Cover calculation to 452.

The source-sink reconstruction still has the free parameter of the tip radius, which determines both the reconstruction itself and the detector binning. Because these choices must be self-consistent, the reconstruction tip radius is 10.5 nm. The z-increment within a bin was defined by the particle diameter of 2 Å, and a small indicial z-increment of  $3 \times 10^{-5}$  nm was applied globally.

## 5.4 Results and Discussion

To ensure that there are minimal effects on the sample evaporation besides the field difference for clusters, we simulated two versions of the sample: one with the field difference as stated above, and one with both types set to the evaporation field of Si. Evaporation differs significantly depending on the evaporation field of the material as expected. Figure 5.3 shows how, for the simulated data, the detector heat map changes depending whether the field difference is present or not. When there is no field difference (Figure 5.3a), there are small scale intensity variations that can be attributed to the evaporation process itself. When the field difference is present (Figure 5.3b), however, larger scale fluctuations appear that are due to the local magnification around the clusters. The source-sink reconstruction aims to fix these density fluctuations in a local and unbiased manner.

By comparing the source-sink reconstructions to both the input pattern and the standard (error-minimized) reconstruction, we can determine the method’s performance. Figure 5.4

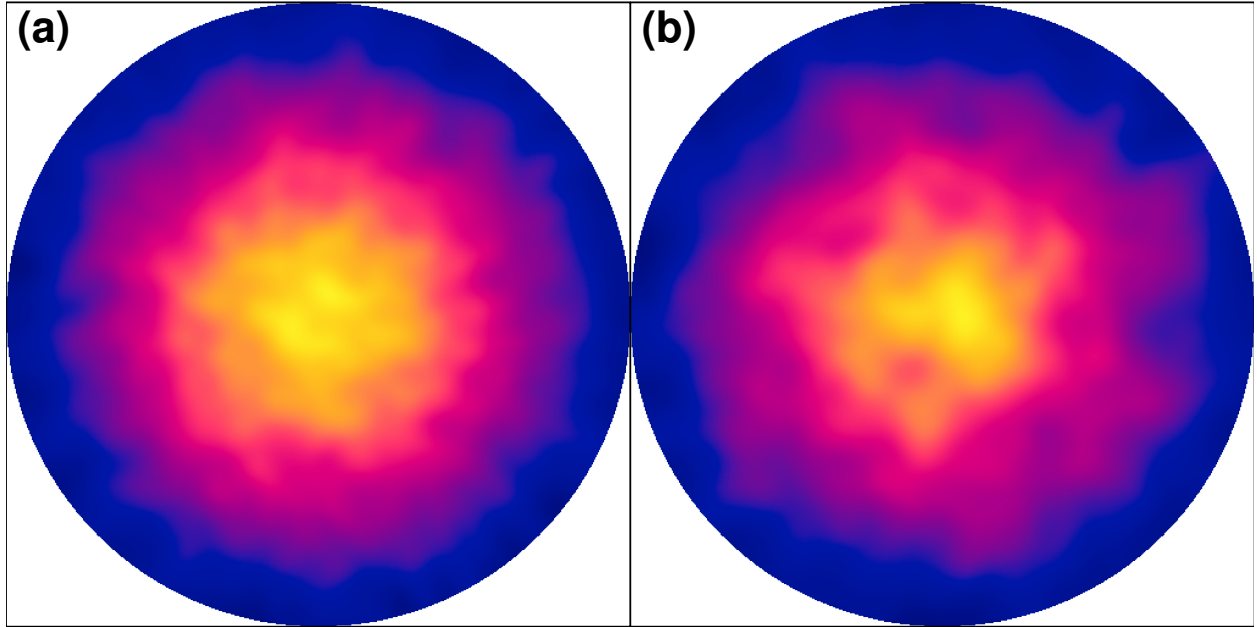


Figure 5.3: Comparison of the simulated detector heat map for (a) equal evaporation fields and (b) an approximately 2:1 field difference using the same input pattern; the diameter of each heat map is 20 cm. With the field difference the heat map is considerably more mottled.

shows the G-functions for the clustered points in the different reconstructions. Clearly, because of the strong evaporation field difference, the clustered signal in the reconstructions is much smaller than in the input pattern. However, zooming in (inset of Figure 5.4) shows that the source-sink reconstruction has a much stronger clustering signal than the standard reconstruction. In fact, even though there is some deviation of the G-function above the envelope for the standard reconstruction, the DCLF test (Equation 5.1) shows that it is not statistically significant.[79]

Figure 5.5 shows the result of the DCLF test applied along a sweep of  $r$  values. Both the input pattern and the source-sink reconstruction very quickly approach a  $p$ -value of zero past  $\sim 0.2$  nm, while the standard reconstruction  $p$ -value is always high. Applying our knowledge of the input clusters, we can enhance the sensitivity of the test by adjusting the bounds of the integral to the size of the cluster (*i.e.*  $\sim 0.2$  to  $0.7$  nm). Even in this high sensitivity case, the standard reconstruction still does not show significant clustering ( $p = 0.224$ ), while

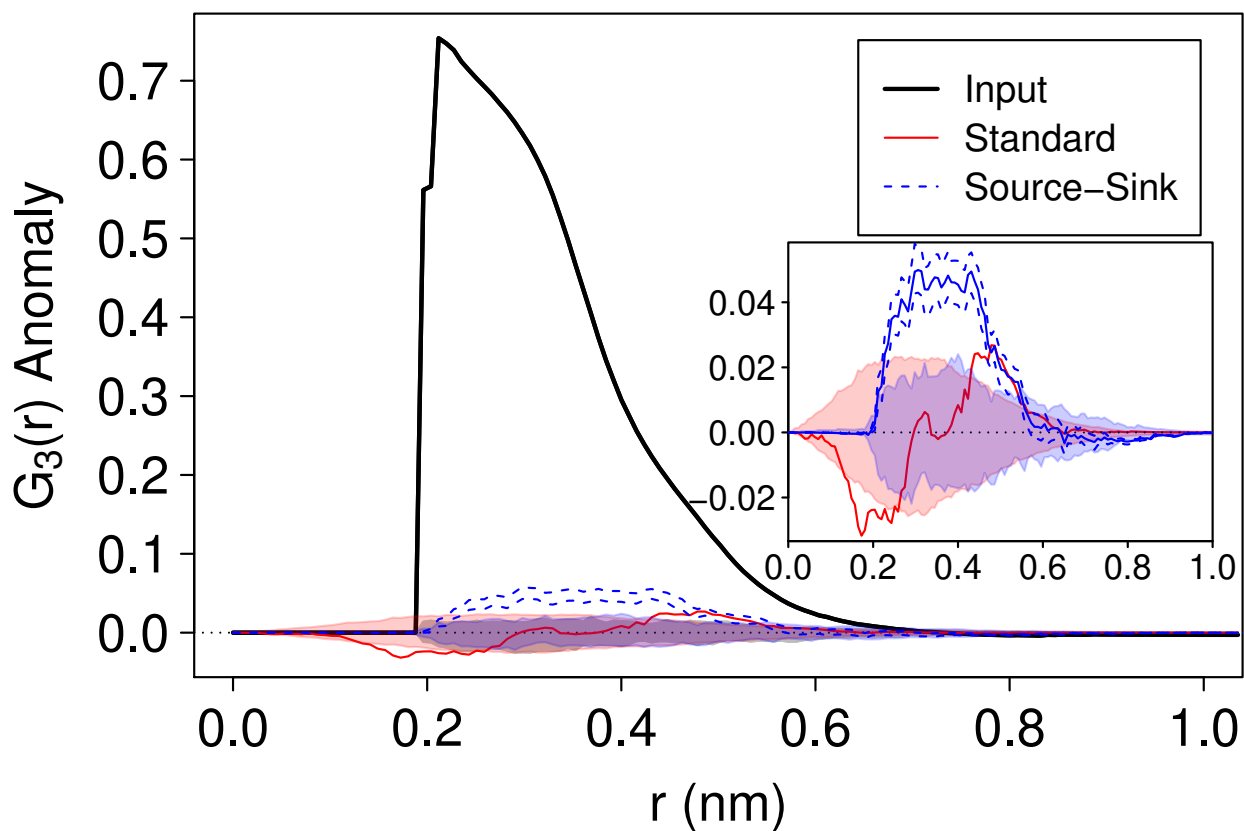


Figure 5.4: Comparison of the source-sink method (blue) to the standard method (red) of reconstruction using the G function; the black curve shows the input pattern, which has a much stronger clustering signal because of the absence of the field evaporation difference. The envelopes are 98% acceptance intervals. (*inset*) Zoomed-in region comparing the two reconstruction methods. The clustering signal is clear in the source-sink reconstruction ( $p < 0.001$ ), while it is not significant ( $p = 0.224$ ) for the standard reconstruction (see Figure 5.5).

the source-sink method has highly significant clustering ( $p < 0.001$ ).

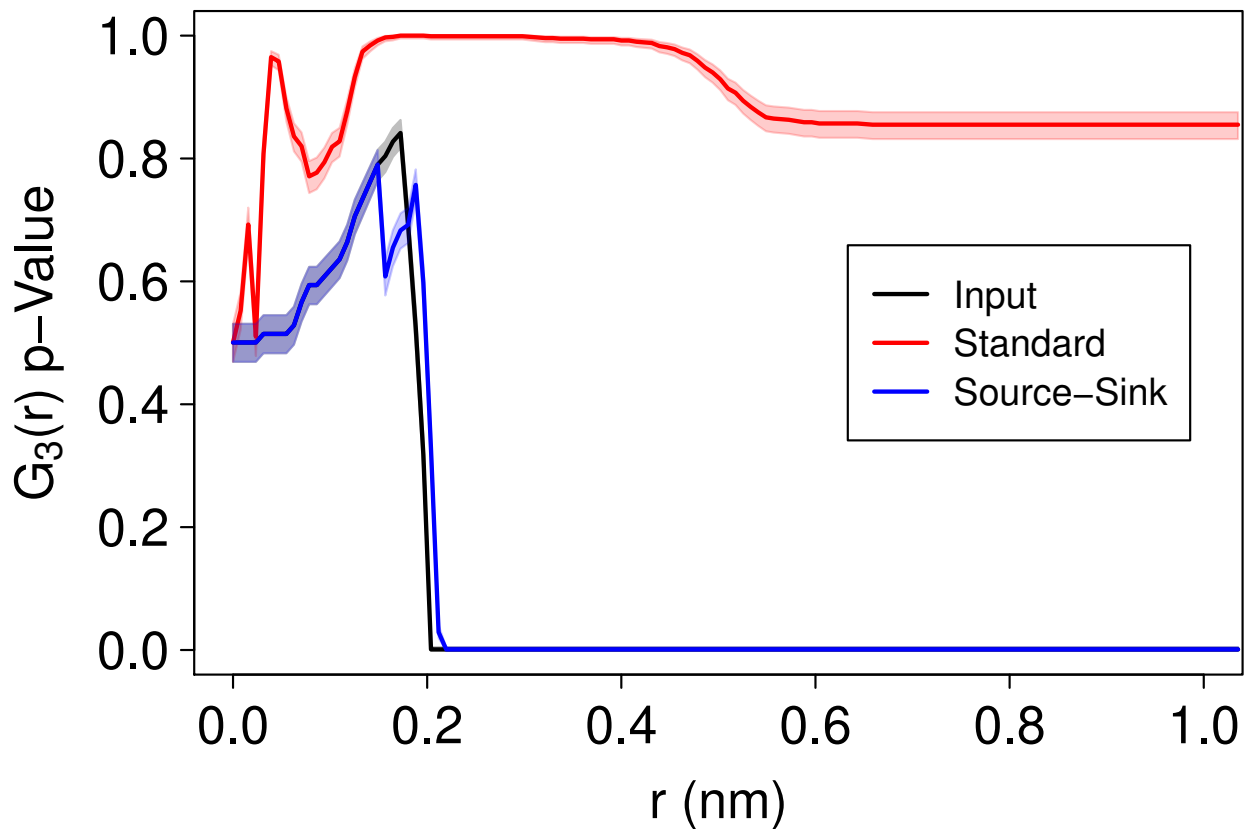


Figure 5.5: p-values based on a DCLF test (Equation 5.1) for the measured G-functions in Figure 5.4; the envelopes are 95 % confidence bands. While the standard reconstruction (red) does not show any signs of clustering ( $p = 0.224$ ), the source-sink method (blue) shows highly significant ( $p < 0.001$ ) clustering past  $\sim 0.2$  nm; this matches the expected behavior based on the input pattern (black).

The G-function only looks at nearest neighbor distances, so to look at longer range behavior we use the K-function (Figure 5.6), which summarizes the behavior of all the points within a particular distance (see Chapter 2). Here, again, the source-sink reconstruction more closely matches the input pattern signal at small distances; the standard reconstruction does show signs of clustering, but only starting around 0.6 nm, which is considerably larger than the point diameter (0.2 nm) and almost the expected diameter of the cluster (0.7 nm). At larger distances, however, both reconstructions fail to match the input pattern’s signal, staying outside the envelope much longer. This behavior is consistent with the expected

impact of local magnification: the small, dense clusters get smeared out and look like larger, lower density clusters.

It is to be expected that the source-sink method works better at smaller distances: it is a local adjustment of point positions. While this will correct for near-field effects due to the evaporation field difference between Si and B, which leads to local magnification and delayed evaporation of the higher-field B clusters, far-field effects (*e.g.* tip shape non-ideality) will still impact reconstruction quality.[63, 65, 126] Some marginal improvement might be expected if the practical limitation on neighborhood size can be removed, expanding the size of regions that can be corrected, but the method is targeted at local trajectory changes. The method should have no problem integrating with larger-scale correction methods, such as image sharpening techniques or dynamic standard reconstruction parameters that have been proposed to deal with larger aberrations.[126, 147] This should improve the fidelity of the reconstruction even further, increasing confidence in the conclusions drawn from it.

## 5.5 Conclusion

The fidelity of APT reconstructions is crucial to extracting high-quality spatial information. Unfortunately, the heterogeneous structures that are most interesting can also affect the evaporation process (*e.g.* evaporation field differences leading to local magnification effects), causing signal degradation. The source-sink reconstruction process partially corrects for near-field effects, such as chromatic aberrations, by exploring the local configuration space; these local effects are challenging to correct, especially in the absence of correlated external measurements. By using the assumption of well-ordered evaporation, it can use physical properties to maintain interpoint spacing, bringing the reconstruction closer to the true sample and outperforming even an error-minimized standard reconstruction. In combination with complementary far-field corrections, source-sink reconstruction can significantly improve the accuracy of reconstructions and increase confidence in any morphological conclusions.

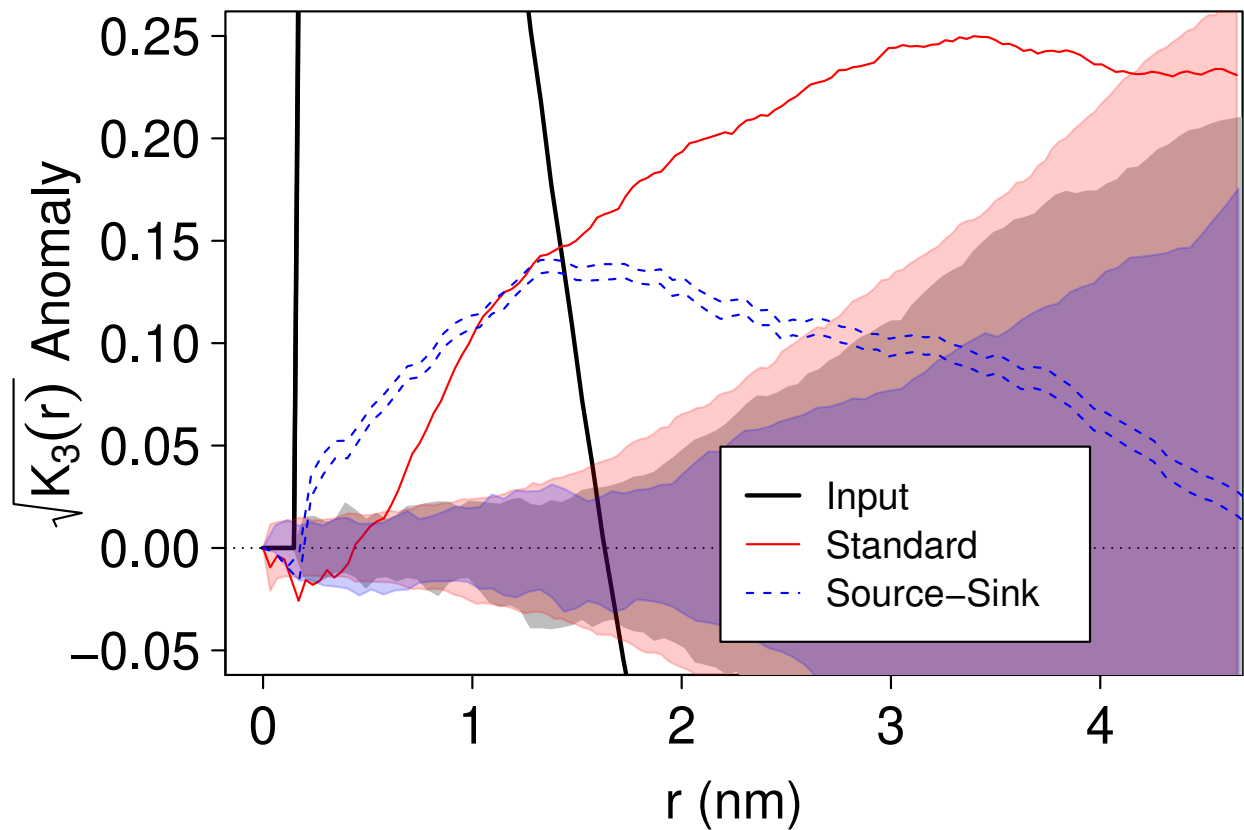


Figure 5.6: Comparison of the source-sink method (blue) to the standard method (red) of reconstruction using the K function the envelopes are 98% acceptance intervals. While both fail to match the behavior of the input pattern (black) at large  $r$ , the source-sink method reproduces the behavior at small  $r$  much better.

## CHAPTER 6

### CONCLUSION

*Scientific understanding of the underlying physics and chemistry [of materials] requires advanced characterization tools that provide critical three-dimensional information at the subnanometer length scale.*

–Amouyal and Schmitz [66]

Morphology is inextricably linked to the behavior of organic devices, and it is crucial to understand—and ultimately control—the structures of these systems. Using atom probe tomography (APT) to study small-molecule organic semiconducting systems can potentially answer long-standing questions of device characteristics and bolster a broader theory of organic electronic physics. The high chemical discrimination ( $< 1$  Da), spatial resolution ( $\sim 0.3$  nm in  $z$  and  $\sim 1$  nm in  $x$ - $y$ ), and analytic sensitivity ( $\sim 50$  ppm) we have achieved with APT are unmatched for studying the morphology of small-molecule organic semiconducting materials.[54]

Through APT we have definitively explained a long-standing question about the open circuit voltage ( $V_{OC}$ ) of the bilayer tetracene (Tc)/ $C_{60}$  organic photovoltaic (OPV) system.[1] We directly detected an interfacial solid-state Diels-Alder cycloadduct (DAc) and reconstructed the spatial distribution of this product in an OPV device to confirm it is confined to the donor-acceptor interface (see Figure 4.3). This, combined with device data showing changes in  $V_{OC}$  with DAc concentration (see Figure 4.4), permits a very clear explanation of the mechanism: the cycloaddition reaction removes the deepest traps from the heterointerface, reducing the average reorganization energy for charge transfer (CT)-exciton formation and consequently increasing  $V_{OC}$ . APT played a critical role in understanding this structure-property relationship.

In addition to layered devices, APT can look at bulk materials for structure. We measured clustering in the active layer of an organic light-emitting diode (OLED) system consisting of a tris[2-phenylpyridinato-C2,N]iridium(III) ( $\text{Ir}(\text{ppy})_3$ ) guest in a matrix of 4,4'-bis(N-carbazolyl)-1,1'-biphenyl (CBP) (see Figure 4.6).[54] This clustering has ramifications on device performance through mechanisms such as triplet-triplet annihilation (TTA) or triplet-polaron quenching (TPQ), though work to fully describe the impact of system morphology on device properties is ongoing. More broadly, analysis of molecular positions in the bulk of a sample enables investigations of solid-state molecular solubility, directing materials design to control morphology and hence device performance.

APT can answer questions about degradation processes as well. We showed that photodegradation in  $\text{Ir}(\text{ppy})_3$  primarily results in  $\text{Ir}(\text{ppy})_3$  oligomers and 2-phenylpyridine (ppy) by performing ultraviolet (UV) exposure *in situ* using the laser system already present on the Local Electrode Atom Probe<sup>TM</sup> 4000X Si (LEAP). The formation of these products is dependent on exciton density (*i.e.* APT laser pulse energy), with the oligomers detected when exposed at 10 pJ but absent at 1 pJ (see Figure 4.12); an as yet unidentified product at 168 Da has a higher onset threshold of 20 to 30 pJ (see Figure 4.10). These results already provide new information to the OLED community, which has had challenges analyzing chemical composition and degradation products.[62, 80] By extending these studies to materials systems (*e.g.*  $\text{Ir}(\text{ppy})_3$ :CBP), the locations of these products and their molecular environment can help uncover particular degradation pathways.

In all this work, the quality of the reconstruction is critical to our confidence in our interpretations. The source-sink reconstruction method helps correct for known artifacts due to near-field effects that are challenging to address in other ways. It can partially recover a clustering signal in a simulated sample with a strong evaporation field difference that was completely washed-out in an error-minimized reconstruction using the standard method in CAMECA's integrated visualization and analysis software (IVAS) (see Figure 5.4). Combining this correction with reconstruction methods that adjust for far-field effects will

complement this enhanced reconstruction accuracy, further improving confidence and our ability to perform spatial analyses.

The data analysis tools of spatial statistics are highly valuable as APT pushes its limits of spatial analysis. The `rapt` package is a toolkit that brings together the different analyses needed for APT data into one place, leveraging the excellent data analytics environment of `R`. In particular, the natural application of spatial statistical methods is streamlined by creating a single environment for processing and analysis. By making it easy to perform spatial statistics tests, `rapt` helps these analyses to be adopted by the APT community, which enhances the rigor of scientific inquiry. Further demonstrations of the capabilities of `rapt` and spatial statistics for APT are forthcoming.

The spatial information provided by APT is particularly valuable for closing the experiment-theory loop. Positions of molecules could be fed into a model of electronic transport to compare predicted and measured device properties, which would allow rapid testing of models and point to areas of theory that require refinement. Presently, organic layer morphologies are simulated, meaning that many assumptions and simplifications exist in the transport model at initialization, making it more challenging to compare results to what is observed in devices.[148] Using APT data—either directly or through a morphological model that has been experimentally validated using spatial statistics—will provide a closer representation of molecular distribution, allowing for more precise comparisons of behavior between the model results and device performance. This makes the unique data that APT provides highly valuable for improving our understanding of the physics of small-molecule organic semiconducting systems.

Taken together, the demonstrated capabilities of APT already enable many outstanding questions in the organic semiconducting community to be answered with its help, but there are ways to further improve its reach. The largest of these is using focused ion beam (FIB) milling to prepare APT samples. Over the last decade or so, this has become a standard method of sample preparation for APT,[39] and while this makes sample preparation more

challenging, it is similar in complexity to the preparation of organic samples for transmission electron microscopy (TEM) imaging.[24] Some work has been done to use a FIB to lift out a section of organic material from a film.[31, 149] If radiation damage can be mitigated, FIB lift-outs should allow for better spatial resolution both because it removes the limitation on the radius of curvature to be locally flat, permitting smaller tip radii to enhance spatial resolution, and through possible correlative TEM measurements.[130]

FIB lift-out of organic semiconductor devices also opens up many more avenues for experimentation. In particular, it allows devices to be analyzed after operation, which permits observations of the morphological differences between devices before and after. This would facilitate direct experimental testing of models, such as the current filamentation expected during OLED operation, which should leave a signature through TPQ degradation products.[150] More generally, studying of how operation and processing affect morphology, molecular migration, or new chemical species creation due to material reactions will deepen our understanding of degradation processes.[10] This capability would expand the applicability of APT for small-molecule organic semiconducting materials and enhance the value of modeling results derived from its data.

Through chemically-specific and spatially-resolved information, APT can answer questions about both bulk and interfacial structures. This capability adds another powerful characterization tool for the organic electronics community, enabling new experimental directions. As APT matures, it will become an ever more valuable technique for studying organic molecular materials. By providing high-resolution and chemically-specific information, APT can help move organic semiconductors towards their promise of large-scale, high-versatility, and low-cost electronics.

## REFERENCES CITED

- [1] Andrew P. Proudian, Matthew B. Jaskot, Christelle Lyiza, David R. Diercks, Brian P. Gorman, and Jeramy D. Zimmerman. Effect of Diels–Alder Reaction in C60-Tetracene Photovoltaic Devices. *Nano Letters*, 16(10):6086–6091, oct 2016. doi: 10.1021/acs.nanolett.6b02238.
- [2] Mikkel Jørgensen, Kion Norrman, and Frederik C. Krebs. Stability/degradation of polymer solar cells. *Solar Energy Materials and Solar Cells*, 92(7):686–714, jul 2008. doi: 10.1016/j.solmat.2008.01.005.
- [3] Daniel J Gaspar. Materials, Processing, and Applications. In Daniel J Gaspar and Evgueni Polikarpov, editors, *OLED Fundamentals: Materials, Devices, and Processing of Organic Light-Emitting Diodes*, page 437. CRC Press, 2015.
- [4] Bernard Kippelen and Jean-Luc Bredas. Organic Photovoltaics. *Energy & Environmental Science*, 2(3):251–261, 2009. doi: 10.1039/b812502n.
- [5] Noel C. Giebink, Gary P Wiederrecht, Michael R Wasielewski, and Stephen R Forrest. Ideal diode equation for organic heterojunctions. I. Derivation and application. *Physical Review B*, 82(15):155305, oct 2010. doi: 10.1103/PhysRevB.82.155305.
- [6] Yunhui L. Lin, Michael A. Fusella, and Barry P. Rand. The Impact of Local Morphology on Organic Donor/Acceptor Charge Transfer States. *Advanced Energy Materials*, 1702816:1702816, 2018. doi: 10.1002/aenm.201702816.
- [7] K. Maturova, S. S. van Bavel, M M Wienk, R A J Janssen, and Martijn Kemerink. Morphological Device Model for Organic Bulk Heterojunction Solar Cells. *Nano Letters*, 9(8):3032–3037, aug 2009. doi: 10.1021/nl901511a.
- [8] Michael A. Brady, Gregory M. Su, and Michael L. Chabinye. Recent progress in the morphology of bulk heterojunction photovoltaics. *Soft Matter*, 7(23):11065, 2011. doi: 10.1039/c1sm06147j.
- [9] Chris Groves, Obadiah G Reid, and David S Ginger. Heterogeneity in Polymer Solar Cells: Local Morphology and Performance in Organic Photovoltaics Studied with Scanning Probe Microscopy. *Accounts of Chemical Research*, 43(5):612–620, may 2010. doi: 10.1021/ar900231q.

- [10] Arthur R.G. G Smith, Jeremy L. Ruggles, Hamish Cavaye, Paul E. Shaw, Tamim a. Darwish, Michael James, Ian R. Gentle, and Paul L. Burn. Investigating morphology and stability of fac-tris (2-phenylpyridyl) iridium(III) films for OLEDs. *Advanced Functional Materials*, 21(12):2225–2231, 2011. doi: 10.1002/adfm.201002365.
- [11] Wei Lin Leong, Gregory C. Welch, Jason Seifert, Jung Hwa Seo, Guillermo C. Bazan, and Alan J. Heeger. Understanding the role of thermal processing in high performance solution processed small molecule bulk heterojunction solar cells. *Advanced Energy Materials*, 3(3):356–363, 2013. doi: 10.1002/aenm.201200631.
- [12] Alfred Neuhold, Hannes Brandner, Simon J. Ausserlechner, Stefan Lorbeck, Markus Neuschitzer, Egbert Zojer, Christian Teichert, and Roland Resel. X-ray based tools for the investigation of buried interfaces in organic electronic devices. *Organic Electronics*, 14(2):479–487, 2013. doi: 10.1016/j.orgel.2012.11.016.
- [13] Koen Vandewal, Scott Himmelberger, and Alberto Salleo. Structural Factors That Affect the Performance of Organic Bulk Heterojunction Solar Cells. *Macromolecules*, 46:6379–6387, 2013. doi: 10.1021/ma400924b.
- [14] Yao-Tsung Tsung Fu, Demetrio A. Da Silva Filho, Gjergji Sini, Abdullah M. Asiri, Saadullah Gary Aziz, Chad Risko, and Jean-Luc Bredas. Structure and Disorder in Squaraine-C60 Organic Solar Cells: A Theoretical Description of Molecular Packing and Electronic Coupling at the Donor-Acceptor Interface. *Advanced Functional Materials*, 24(24):3790–3798, feb 2014. doi: 10.1002/adfm.201303941.
- [15] Shuqiong Lan, Huihuang Yang, Guocheng Zhang, Xiaomin Wu, Wen Ning, Shuiming Wang, Huipeng Chen, and Tailiang Guo. Impact of Fullerene Structure on Nanoscale Morphology and Miscibility and Correlation of Performance on Small Molecules: Fullerene Solar Cell. *The Journal of Physical Chemistry C*, 120(38):acs.jpcc.6b08025, 2016. doi: 10.1021/acs.jpcc.6b08025.
- [16] Jane Vinokur, Stas Obuchovsky, Igal Deckman, Lishai Shoham, Tom Mates, Michael L. Chabinyc, and Gitti L. Frey. Dynamics of Additive Migration to Form Cathodic Interlayers in Organic Solar Cells. *ACS Applied Materials and Interfaces*, 9(35):29889–29900, sep 2017. doi: 10.1021/acsami.7b06793.
- [17] Brian W. D’Andrade, Stephen R. Forrest, and Anna B. Chwang. Operational stability of electrophosphorescent devices containing p and n doped transport layers. *Applied Physics Letters*, 83(19):3858–3860, 2003. doi: 10.1063/1.1624473.
- [18] Ines Rabelo De Moraes, Sebastian Scholz, Björn Lüssem, and Karl Leo. Chemical degradation processes of highly stable red phosphorescent organic light emitting diodes. *Organic Electronics*, 13(10):1900–1907, 2012. doi: 10.1016/j.orgel.2012.04.025.

- [19] Yong Joo Cho, Yingjie Zhang, Hyeonghwa Yu, and Hany Aziz. The Root Causes of the Limited Stability of Solution-Coated Small-Molecule Organic Light-Emitting Devices: Faster Host Aggregation by Exciton-Polaron Interactions. *Advanced Functional Materials*, 26(47):8662–8669, 2016. doi: 10.1002/adfm.201603542.
- [20] Isabel Fraga Domínguez, Andreas Distler, and Larry Lüer. Stability of Organic Solar Cells: The Influence of Nanostructured Carbon Materials. *Advanced Energy Materials*, 7(10), 2017. doi: 10.1002/aenm.201601320.
- [21] William R. Mateker and Michael D. McGehee. Progress in Understanding Degradation Mechanisms and Improving Stability in Organic Photovoltaics. *Advanced Materials*, 29(10):1603940, mar 2017. doi: 10.1002/adma.201603940.
- [22] Shou Cheng Dong, Lisong Xu, and Ching W. Tang. Chemical degradation mechanism of TAPC as hole transport layer in blue phosphorescent OLED. *Organic Electronics: physics, materials, applications*, 42:379–386, 2017. doi: 10.1016/j.orgel.2016.11.041.
- [23] John S. Bangsund, Kyle W. Hershey, and Russell J. Holmes. Isolating Degradation Mechanisms in Mixed Emissive Layer Organic Light-Emitting Devices. *ACS Applied Materials and Interfaces*, 10(6):5693–5699, feb 2018. doi: 10.1021/acsami.7b16643.
- [24] Wei Chen, Maxim P. Nikiforov, and Seth B. Darling. Morphology characterization in organic and hybrid solar cells. *Energy & Environmental Science*, 5(8):8045, 2012. doi: 10.1039/c2ee22056c.
- [25] Martin Pfannmöller, Wolfgang Kowalsky, and Rasmus R. Schröder. Visualizing physical, electronic, and optical properties of organic photovoltaic cells. *Energy & Environmental Science*, 6(10):2871, 2013. doi: 10.1039/c3ee41773e.
- [26] John D. Roehling, K. Joost Batenburg, F. Benjamin Swain, Adam J. Moulé, and Ilke Arslan. Three-Dimensional Concentration Mapping of Organic Blends. *Advanced Functional Materials*, 23(17):2115–2122, may 2013. doi: 10.1002/adfm.201202190.
- [27] Elizabeth M. Tennyson, John M. Howard, and Marina S. Leite. Mesoscale Functional Imaging of Materials for Photovoltaics. *ACS Energy Letters*, 2(8):1825–1834, 2017. doi: 10.1021/acseenergylett.7b00382.
- [28] A. Neuhold, J. Novák, H. G. Flesch, A. Moser, T. Djuric, L. Grodd, S. Grigorian, U. Pietsch, and R. Resel. X-ray radiation damage of organic semiconductor thin films during grazing incidence diffraction experiments. *Nuclear Instruments and Methods in Physics Research, Section B: Beam Interactions with Materials and Atoms*, 284:64–68, 2012. doi: 10.1016/j.nimb.2011.07.105.

- [29] Wolfram Schindler, Markus Wollgarten, and Konstantinos Fostiropoulos. Revealing nanoscale phase separation in small-molecule photovoltaic blends by plasmonic contrast in the TEM. *Organic Electronics*, 13(6):1100–1104, jun 2012. doi: 10.1016/j.orgel.2012.03.008.
- [30] John A. Love, Christopher M. Proctor, Jianhua Liu, Christopher J. Takacs, Alexander Sharenko, Thomas S. Van Der Poll, Alan J. Heeger, Guillermo C. Bazan, and Thuc Quyen Nguyen. Film morphology of high efficiency solution-processed small-molecule solar cells. *Advanced Functional Materials*, 23(40):5019–5026, 2013. doi: 10.1002/adfm.201300099.
- [31] A. Orthacker, R. Schmied, B. Chernev, J. E. Fröch, R. Winkler, J. Hobisch, G. Trimmel, and H. Plank. Chemical degradation and morphological instabilities during focused ion beam prototyping of polymers. *Phys. Chem. Chem. Phys.*, 16(4):1658–1666, 2014. doi: 10.1039/c3cp54037e.
- [32] Sebastian Reineke, Gregor Schwartz, Karsten Walzer, Meiken Falke, and Karl Leo. Highly phosphorescent organic mixed films: The effect of aggregation on triplet-triplet annihilation. *Applied Physics Letters*, 94(16):2007–2010, 2009. doi: 10.1063/1.3123815.
- [33] Dan Deng, Yajie Zhang, Jianqi Zhang, Zhen Zaiyu Zhen Zaiyu Wang, Lingyun Zhu, Jin Fang, Benzhen Xia, Zhen Zaiyu Zhen Zaiyu Wang, Kun Lu, Wei Ma, and Zhixiang Wei. Fluorination-enabled optimal morphology leads to over 11% efficiency for inverted small-molecule organic solar cells. *Nature Communications*, 7:1–9, 2016. doi: 10.1038/ncomms13740.
- [34] S. V. Vickers, H. Barcena, K. A. Knights, R. K. Thomas, J. C. Ribierre, S. Gambino, I. D W Samuel, P. L. Burn, and Giovanna Fragneto. Light-emitting dendrimer film morphology: A neutron reflectivity study. *Applied Physics Letters*, 96(26):4–7, 2010. doi: 10.1063/1.3457438.
- [35] Sean E. Shaheen, Christoph J. Brabec, Niyazi Serdar Sariciftci, Franz Padinger, Thomas Fromherz, and Jan C. Hummelen. 2.5% Efficient Organic Plastic Solar Cells. *Applied Physics Letters*, 78(6):841, 2001. doi: 10.1063/1.1345834.
- [36] Jeroen K J van Duren, Xiaoni Yang, Joachim Loos, Corrie W T Bulle-Lieuwma, Alexander B. Sieval, Jan C. Hummelen, and René A J Janssen. Relating The Morphology Of Poly(P-Phenylene Vinylene)/Methanofullerene Blends To Solar-Cell Performance. *Advanced Functional Materials*, 14(5):425–434, may 2004. doi: 10.1002/adfm.200305049.
- [37] C. R. McNeill, C. J.R. R Fell, J. L. Holdsworth, and P. C. Dastoor. Screening for artifacts in near-field scanning photocurrent microscopy images of polymer solar cells. *Synthetic Metals*, 153(1-3):85–88, 2005. doi: 10.1016/j.synthmet.2005.07.159.

- [38] Nicholas J. Popczun, Lars Breuer, Andreas Wucher, and Nicholas Winograd. On the SIMS Ionization Probability of Organic Molecules. *Journal of The American Society for Mass Spectrometry*, 28(6):1182–1191, jun 2017. doi: 10.1007/s13361-017-1624-0.
- [39] Thomas F. Kelly and Michael K. Miller. Invited review article: Atom probe tomography. *Review of Scientific Instruments*, 78(3):31101, mar 2007. doi: 10.1063/1.2709758.
- [40] Thomas F. Kelly and David J. Larson. Atom Probe Tomography 2012. *Annual Review of Materials Research*, 42(1):1–31, aug 2012. doi: 10.1146/annurev-matsci-070511-155007.
- [41] Robert M. Ulfing, Ty J. Prosa, Yimeng Chen, Katherine P. Rice, Isabelle. Martin, David A. Reinhard, Brian P. Gieser, Edward Oltman, Dan R. Lenz, Joseph Bunton, Michael Van Dyke, Thomas F. Kelly, and David J. Larson. Hardware and Software Advances in Commercially Available Atom Probe Tomography Systems. *Microscopy and Microanalysis*, 23(S1):40–41, jul 2017. doi: 10.1017/S1431927617000885.
- [42] Brian P Geiser, Thomas F Kelly, David J. Larson, Jason Schneir, and Jay P Roberts. Spatial Distribution Maps for Atom Probe Tomography. *Microscopy and Microanalysis*, 13(06):437–447, dec 2007. doi: 10.1017/S1431927607070948.
- [43] P Bas, Alain Bostel, Bernard Deconihout, and Didier Blavette. A general protocol for the reconstruction of 3D atom probe data. *Applied Surface Science*, 87-88(1-4): 298–304, 1995.
- [44] E.S. S Machlin, A. Freilich, D.C. C Agrawal, J.J. J Burton, and C.L. L Briant. Field ion microscopy of biomolecules. *Journal of Microscopy*, 104(2):127–168, 1975. doi: 10.1111/j.1365-2818.1975.tb04012.x.
- [45] John A. Panitz. Point-Projection Imaging of Unstained Ferritin Clusters. *Ultramicroscopy*, 7:241–248, 1982.
- [46] John A. Panitz. Direct Visualization of Unstained Nucleic Acids on a Metal Substrate. *Ultramicroscopy*, 11:161–166, 1983.
- [47] O. Nishikawa, T. Sekine, Y. Ohtani, K. Maeda, Y. Numada, and M. Watanabe. Atomic Investigation of Individual Apexes of Diamond Emitters by a Scanning Atom Probe. *Journal of Vacuum Science & Technology B*, 16(2):836–840, 1998.
- [48] Osamu Nishikawa and Hitoshi Kato. Atom-probe study of a conducting polymer: The oxidation of polypyrrole. *The Journal of Chemical Physics*, 85(11):6758–6764, 1986. doi: 10.1063/1.451407.

- [49] T. Maruyama, Y. Hasegawa, T. Nishi, and T. Sakurai. FIM AND ATOM-PROBE STUDY OF POLYMERS. *Le Journal de Physique Colloques*, 48(C6):269–274, nov 1987. doi: 10.1051/jphyscol:1987644.
- [50] Yi Zhang. *Three dimensional atom probe tomography of nanoscale thin films, interfaces and particles*. PhD thesis, Iowa State University, 2009. URL <http://www.grin.com/en/doc/232384/three-dimensional-atom-probe-tomography-of-nanoscale-thin-films-interfaces>.
- [51] Ty J. Prosa, S Kostrna Keeney, and Thomas F. Kelly. Atom Probe Tomography Analysis of poly(3-alkylthiophene)s. *Journal of Microscopy*, 237(2):155–167, feb 2010. doi: 10.1111/j.1365-2818.2009.03320.x.
- [52] Derk Joester, Andrew Hillier, Yi Zhang, and Ty J. Prosa. Organic Materials and Organic/Inorganic Heterostructures in Atom Probe Tomography. *Microsc. Today*, 20(03):26–31, may 2012. doi: 10.1017/S1551929512000260.
- [53] James S. Chickos and William E. Acree. Enthalpies of vaporization of organic and organometallic compounds, 1880-2002. *Journal of Physical and Chemical Reference Data*, 32(2):519–878, 2003. doi: 10.1063/1.1529214.
- [54] Andrew P. Proudian, Matthew B. Jaskot, David R. Diercks, Brian P. Gorman, and Jeremy D. Zimmerman. Atom Probe Tomography of Molecular Organic Materials: Sub-Dalton Nanometer-Scale Quantification. *Chemistry of Materials*, 31(7):2241–2247, apr 2019. doi: 10.1021/acs.chemmater.8b04476.
- [55] Markus Schworer and Hans Christoph Wolf. *Organic Molecular Solids*. WILEY-VCH, KGaA, Weinheim, 2007. ISBN 978-3-527-40540-4.
- [56] Martin Pope, H P Kallmann, and P Magnante. Electroluminescence in Organic Crystals. *The Journal of Chemical Physics*, 38(1963):2042, 1963. doi: 10.1063/1.1733929.
- [57] Ching W. Tang and S. A. Vanslyke. Organic electroluminescent diodes. *Applied Physics Letters*, 51(1987):913–915, 1987. doi: 10.1063/1.98799.
- [58] M. A. Baldo, M. E. Thompson, and S. R. Forrest. High-efficiency fluorescent organic light-emitting devices using a phosphorescent sensitizer. *Nature*, 403(6771):750–753, feb 2000. doi: 10.1038/35001541.
- [59] Marc A. Baldo, D. F. O’Brien, Y. You, A. Shoustikov, S. Sibley, Mark E. Thompson, and Stephen R. Forrest. Highly efficient phosphorescent emission from organic electroluminescent devices. *Nature*, 395(6698):151–154, 1998. doi: 10.1038/25954.

- [60] Mark Thompson. The Evolution of Organometallic Complexes in Organic Light- Emitting Devices. *MRS Bulletin*, 32(September):694–701, 2007.
- [61] Marc A. Baldo, C. Adachi, and S. R. Forrest. Transient analysis of organic electrophosphorescence. II. Transient analysis of triplet-triplet annihilation. *Physical Review B*, 62(16):10967–10977, oct 2000. doi: 10.1103/PhysRevB.62.10967.
- [62] Sebastian Scholz, Denis Kondakov, Björn Lüssem, and Karl Leo. Degradation mechanisms and reactions in organic light-emitting devices. *Chemical Reviews*, 115(16): 8449–8503, 2015. doi: 10.1021/cr400704v.
- [63] Baptiste Gault, Michael P Moody, Julie M Cairney, and Simon P Ringer. *Atom Probe Microscopy*. Springer, 2012.
- [64] Erwin W Müller, John A Panitz, and S Brooks McLane. The Atom-Probe Field Ion Microscope. *Review of Scientific Instruments*, 39(1):83–86, jan 1968. doi: 10.1063/1.1683116.
- [65] David J. Larson, Ty J. Prosa, Robert M. Ulfig, Brian P. Geiser, and Thomas F. Kelly. *Local Electrode Atom Probe Tomography*. Springer New York, New York, NY, 2013. ISBN 978-1-4614-8720-3. doi: 10.1007/978-1-4614-8721-0.
- [66] Yaron Amouyal and Guido Schmitz. Atom probe tomography — A cornerstone in materials characterization. *MRS Bulletin*, 41(January):13–18, 2016. doi: 10.1557/mrs.2015.313.
- [67] T. Philippe, S. Duguay, G. Grancher, and D. Blavette. Point process statistics in atom probe tomography. *Ultramicroscopy*, 132:114–120, sep 2013. doi: 10.1016/j.ultramic.2012.10.004.
- [68] Ate Poorthuis and Matthew Zook. Small Stories in Big Data: Gaining Insights From Large Spatial Point Pattern Datasets. *Cityscape*, 17(1):151–160, 2015.
- [69] Scott R. Broderick, Aaron Bryden, Santosh K. Suram, and Krishna Rajan. Data mining for isotope discrimination in atom probe tomography. *Ultramicroscopy*, 132: 121–128, sep 2013. doi: 10.1016/j.ultramic.2013.02.001.
- [70] Julie M. Cairney, Krishna Rajan, Daniel Haley, Baptiste Gault, Paul A.J. Bagot, Pyuck-Pa Pa Choi, Peter J. Felfer, Simon P. Ringer, Ross K.W. W Marceau, and Michael P. Moody. Mining information from atom probe data. *Ultramicroscopy*, 159: 324–337, dec 2015. doi: 10.1016/j.ultramic.2015.05.006.

- [71] François Vurpillot, W. Lefebvre, Julie M. Cairney, Christian Oberdorfer, Brian P. Geiser, and Krishna Rajan. Advanced volume reconstruction and data mining methods in atom probe tomography. *MRS Bulletin*, 41(01):46–52, jan 2016. doi: 10.1557/mrs.2015.312.
- [72] A. Cerezo, P. J. Warren, and George D.W. W Smith. Some aspects of image projection in the field-ion microscope. *Ultramicroscopy*, 79(1-4):251–257, sep 1999. doi: 10.1016/S0304-3991(99)00071-6.
- [73] Adrian Baddeley, Ege Rubak, and Rolf Turner. *Spatial Point Patterns: Methodology and Applications with R*. CRC Press, Boca Raton, 2016.
- [74] Nathan D. Wallace, Anna V. Ceguerra, Andrew J. Breen, and Simon P. Ringer. On the Retrieval of Crystallographic Information from Atom Probe Microscopy Data via Signal Mapping from the Detector Coordinate Space. *Ultramicroscopy*, 189:65–75, 2018. doi: 10.1016/j.ultramic.2018.02.006.
- [75] Lan Yao, Julie M. Cairney, Baptiste Gault, C. Zhu, and Simon P. Ringer. Correlating spatial, temporal and chemical information in atom probe data: new insights from multiple evaporation in microalloyed steels. *Philosophical Magazine Letters*, 93(5): 299–306, 2013. doi: 10.1080/09500839.2013.771823.
- [76] David W. Saxey. Correlated ion analysis and the interpretation of atom probe mass spectra. *Ultramicroscopy*, 111(6):473–479, 2011. doi: 10.1016/j.ultramic.2010.11.021.
- [77] Frédéric De Geuser, Baptiste Gault, Alain Bostel, and François Vurpillot. Correlated field evaporation as seen by atom probe tomography. *Surface Science*, 601(2):536–543, 2007. doi: 10.1016/j.susc.2006.10.019.
- [78] Alan E. Gelfand, Peter J. Diggle, Montserrat Fuentes, and Peter Guttorp, editors. *Handbook of Spatial Statistics*. Chapman and Hall/CRC, Boca Raton, 2010. ISBN 978-1-4200-7287-7.
- [79] Peter J Diggle. *Statistical Analysis of Spatial and Spatio-Temporal Point Patterns*. Chapman and Hall/CRC, 3 edition, 2013. ISBN 9781466560239.
- [80] D. Y. Kondakov, W. C. Lenhart, and W. F. Nichols. Operational degradation of organic light-emitting diodes: Mechanism and identification of chemical products. *Journal of Applied Physics*, 101(2), 2007. doi: 10.1063/1.2430922.
- [81] A. Hinderhofer, A. Gerlach, Katharina Broch, Takuya Hosokai, K. Yonezawa, K. Kato, S. Kera, Nobuo Ueno, and F. Schreiber. Geometric and Electronic Structure of Templated C60 on Diindenoperylene Thin Films. *The Journal of Physical Chemistry C*, 117(2):1053–1058, jan 2013. doi: 10.1021/jp3106056.

- [82] Baptiste Gault, Michael P. Moody, Frederic de Geuser, Daniel Haley, Leigh T. Stephenson, and Simon P. Ringer. Origin of the Spatial Resolution in Atom Probe Microscopy. *Applied Physics Letters*, 95(3):34103, 2009. doi: 10.1063/1.3182351.
- [83] RM Fleming, B Hessen, T Siegrist, and AR Kortan. Crystalline Fullerenes: Round Pegs in Square Holes. In George S. Hammond and Valerie J. Kuck, editors, *Fullerenes: Synthesis, Properties, and Chemistry*, pages 25–39. American Chemical Society, 1992. ISBN 0841221820.
- [84] Yuanping Yi, Veaceslav Coropceanu, and Jean-Luc Bredas. Exciton-Dissociation and Charge-Recombination Processes in Pentacene/C 60 Solar Cells: Theoretical Insight into the Impact of Interface Geometry. *Journal of the American Chemical Society*, 131(43):15777–15783, nov 2009. doi: 10.1021/ja905975w.
- [85] Yao Tsung Fu, Chad Risko, and Jean-Luc Bredas. Intermixing at the pentacene-fullerene bilayer interface: A molecular dynamics study. *Advanced Materials*, 25(6): 878–882, 2013. doi: 10.1002/adma.201203412.
- [86] M. Dolores Perez, Carsten Borek, Stephen R Forrest, and Mark E Thompson. Molecular and Morphological Influences on the Open Circuit Voltages of Organic Photovoltaic Devices. *Journal of the American Chemical Society*, 131(26):9281–9286, jul 2009. doi: 10.1021/ja9007722.
- [87] Kenneth R. Graham, Patrick Erwin, Dennis Nordlund, Koen Vandewal, Ruipeng Li, Guy O. Ngongang Ndjawa, Eric T. Hoke, Alberto Salleo, Mark E. Thompson, Michael D. McGehee, and Aram Amassian. Re-evaluating the role of sterics and electronic coupling in determining the open-circuit voltage of organic solar cells. *Advanced Materials*, 25(42):6076–6082, 2013. doi: 10.1002/adma.201301319.
- [88] Yves Rubin and Saeed Khan. Synthesis and x-ray structure of a Diels-Alder adduct of fullerene C60. *J. Am. Chem. Soc.*, 115:344–345, 1993. doi: 10.1021/ja00054a049.
- [89] Sanjio S. Zade, Natalia Zamoshchik, A. Ravikumar Reddy, Galit Fridman-Marueli, Dennis Sheberla, and Michael Bendikov. Products and mechanism of acene dimerization. A computational study. *J. Am. Chem. Soc.*, 133(28):10803–10816, 2011. doi: 10.1021/ja106594v.
- [90] Franco Cataldo, D Aníbal García-hernández, Arturo Manchado, D Aníbal García-Hernández, Arturo Manchado, D Aníbal García-hernández, and Arturo Manchado. A Study on the Synthesis and Stability of the C60 Fullerene/Tetracene Adduct. *European Chemical Bulletin*, 3(8):740–744, 2014. doi: 10.17628/ECB.2014.3.740.

- [91] Francesco Fringuelli and Aldo Taticchi. *The Diels-Alder Reaction: Selected Practical Methods*. John Wiley, New York, NY, 2002.
- [92] Roger Taylor and David R M Walton. The chemistry of fullerenes. *Nature*, 363(6431): 685–693, jun 1993. doi: 10.1038/363685a0.
- [93] Roger Taylor. *Lecture Notes on Fullerene Chemistry: A Handbook for Chemists*. Imperial College Press, 1999.
- [94] Jonathan B Briggs and Glen P Miller. [60]Fullerene-acene chemistry: a review. *Comptes Rendus Chimie*, 9(7-8):916–927, jul 2006. doi: 10.1016/j.crci.2005.11.014.
- [95] John A Schlueter, Julie M Seaman, Sharif Taha, Harry Cohen, Keith R Lykke, H Hau Wang, and Jack M Williams. Synthesis, purification, and characterization of the 1 : 1 addition product of C60 and anthracene. *Journal of the Chemical Society, Chemical Communications*, (11):972, 1993. ISSN 0022-4936. doi: 10.1039/c39930000972.
- [96] Minoru Tsuda, Takayuki Ishida, Takashi Nogami, Sadamu Kurono, and Mamoru Ohashi. Isolation and characterization of Diels–Alder adducts of C60 with anthracene and cyclopentadiene. *J. Chem. Soc., Chem. Commun.*, (16):1296–1298, 1993. doi: 10.1039/C39930001296.
- [97] Ginka H. Sarova and Mário N. Berberan-Santos. Kinetics of the Diels–Alder reaction between C60 and acenes. *Chemical Physics Letters*, 397(4-6):402–407, oct 2004. doi: 10.1016/j.cplett.2004.09.005.
- [98] Wanda Śliwa. Cycloaddition Reactions of Fullerenes. *Fullerene Science and Technology*, 3(3):243–281, jan 1995. doi: 10.1080/153638X9508543782.
- [99] Maria Ángeles Herranz and Luis Echegoyen. Tandem addition reactions of dialkoxyanthracenes with C 60 . Thermal vs. electrochemical stability of Diels–Alder adducts. *New Journal of Chemistry*, 28(4):513–518, 2004. doi: 10.1039/B313984K.
- [100] James Mack and Glen P Miller. Synthesis and Characterization of a C 60 -Pentacene Monoadduct. *Fullerene Science and Technology*, 5(3):607–614, apr 1997. doi: 10.1080/15363839708015911.
- [101] Glen P Miller, Jonathan Briggs, James Mack, Pamela A Lord, Marilyn M Olmstead, and Alan L. Balch. Fullerene-Acene Chemistry: Single-Crystal X-ray Structures for a [60]Fullerene-Pentacene Monoadduct and a cis -Bis[60]fullerene Adduct of 6,13-Diphenylpentacene. *Organic Letters*, 5(22):4199–4202, oct 2003. doi: 10.1021/ol035646l.

- [102] Y. Murata, N. Karo, K. Fujiwara, and K. Komatsu. Solid-state [4 + 2] cycloaddition of fullerene C60 with condensed aromatics using a high-speed vibration milling technique. *J. Org. Chem.*, 64(10):3483–3488, 1999. doi: 10.1021/jo990013z.
- [103] William C Herndon and Lowell H Hall. Endo and Exo Transition States in the Diels-Alder Reaction. *Tetrahedron Letters*, 32(32):3095–3100, 1967.
- [104] John E. Anthony. The larger acenes: Versatile organic semiconductors. *Angewandte Chemie - International Edition*, 47(3):452–483, 2008. doi: 10.1002/anie.200604045.
- [105] Tobias Breuer, Andrea Karthäuser, and Gregor Witte. Effects of Molecular Orientation in Acceptor-Donor Interfaces between Pentacene and C 60 and Diels-Alder Adduct Formation at the Molecular Interface. *Advanced Materials Interfaces*, 3(7):1500452, apr 2016. ISSN 21967350. doi: 10.1002/admi.201500452.
- [106] Woong-Kwon Kim, Bang Joo Song, Kihyon Hong, Kisoo Kim, and Jong-Lam Lee. Effect of O<sub>2</sub>-Plasma Treatment of Mo on the Crystal Growth Mode of Pentacene of Organic Thin-Film Transistors. *Journal of The Electrochemical Society*, 156(8): H674, 2009. doi: 10.1149/1.3153121.
- [107] Feilong L Liu, P P Ruden, Ian H. Campbell, Darryl L. Smith, P. Paul Ruden, Ian H. Campbell, and Darryl L. Smith. Device model for electronic processes at organic/organic interfaces. *J. Appl. Phys.*, 111(9):94507, 2012. doi: 10.1063/1.4709210.
- [108] K H Drexage and F P Schafer. Dye Laser. In *Topics in Applied Physics*. Springer-Verlag, 1 edition, 1977.
- [109] D. R. Lutz, Keith A. Nelson, C. R. Gochanour, and M. D. Fayer. Electronic excited state energy transfer, trapping by dimers and fluorescence quenching in concentrated dye solutions: Picosecond transient grating exp. *Chemical Physics*, 58(3):325–334, 1981. doi: 10.1016/0301-0104(81)80068-7.
- [110] Ching W. Tang, S. A. Vanslyke, and Chin H. Chen. Electroluminescence of doped organic thin films. *Journal of Applied Physics*, 65(9):3610–3616, 1989. doi: 10.1063/1.343409.
- [111] Sebastian Reineke, Gregor Schwartz, Karsten Walzer, and Karl Leo. Reduced efficiency roll-off in phosphorescent organic light emitting diodes by suppression of triplet-triplet annihilation. *Applied Physics Letters*, 91(12):4–7, 2007. doi: 10.1063/1.2786840.
- [112] Dandan Song, Suling Zhao, Yichun Luo, and Hany Aziz. Causes of efficiency roll-off in phosphorescent organic light emitting devices: Triplet-triplet annihilation versus triplet-polaron quenching. *Applied Physics Letters*, 97(24), 2010. doi: 10.1063/1.3527085.

- [113] Marc A. Baldo, D F O'Brien, and Stephen R Forrest. Excitonic singlet-triplet ratio in a semiconducting organic thin film. *Physical Review B*, 60(20):14422–14428, 1999.
- [114] S. Lamansky, Peter I Djurovich, D. Murphy, F. Abdel-Razzaq, H. E. Lee, C. Adachi, P. E. Burrows, Stephen R. Forrest, and Mark E. Thompson. Highly phosphorescent bis-cyclometalated iridium complexes: Synthesis, photophysical characterization, and use in organic light emitting diodes. *Journal of the American Chemical Society*, 123(3):4304–4312, 2001. doi: 10.1021/ja003693s.
- [115] Yuichiro Kawamura, Jason Brooks, Julie J. Brown, Hiroyuki Sasabe, and Chihaya Adachi. Intermolecular interaction and a concentration-Quenching mechanism of phosphorescent Ir(III) complexes in a solid film. *Physical Review Letters*, 96(1):11–14, 2006. doi: 10.1103/PhysRevLett.96.017404.
- [116] Y. Divayana and X. W. Sun. Observation of excitonic quenching by long-range dipole-dipole interaction in sequentially doped organic phosphorescent host-guest system. *Physical Review Letters*, 99(14):1–4, 2007. doi: 10.1103/PhysRevLett.99.143003.
- [117] B D Ripley. Modelling Spatial Patterns. *Journal of the Royal Statistical Society*, 39(2):172–212, 1977.
- [118] Changyeong Jeong, Caleb Coburn, Muazzam Idris, Yongxi Li, Peter I. Djurovich, Mark E. Thompson, and Stephen R. Forrest. Understanding molecular fragmentation in blue phosphorescent organic light-emitting devices. *Organic Electronics*, 64:15–21, jan 2019. doi: 10.1016/j.orgel.2018.10.001.
- [119] Reinder Coehoorn, Harm Van Eersel, Peter A. Bobbert, and René A.J. Janssen. Kinetic Monte Carlo Study of the Sensitivity of OLED Efficiency and Lifetime to Materials Parameters. *Advanced Functional Materials*, 25(13):2024–2037, 2015. doi: 10.1002/adfm.201402532.
- [120] Noel C. Giebink, B. W. D'Andrade, M. S. Weaver, P. B. Mackenzie, J. J. Brown, M. E. Thompson, and S. R. Forrest. Intrinsic luminance loss in phosphorescent small-molecule organic light emitting devices due to bimolecular annihilation reactions. *Journal of Applied Physics*, 103(4):044509, feb 2008. doi: 10.1063/1.2884530.
- [121] Noel C. Giebink, B. W. D'Andrade, M. S. Weaver, J. J. Brown, and S. R. Forrest. Direct evidence for degradation of polaron excited states in organic light emitting diodes. *Journal of Applied Physics*, 105(12):124514, jun 2009. doi: 10.1063/1.3151689.
- [122] Hyeonghwa Yu and Hany Aziz. Direct Observation of Exciton-Induced Molecular Aggregation in Organic Small-Molecule Electroluminescent Materials. *The Journal of Physical Chemistry C*, 123(26):16424–16429, jul 2019. doi: 10.1021/acs.jpcc.9b03364.

- [123] Sebastian Scholz, Rico Meerheim, Björn Lüssem, and Karl Leo. Laser desorption/ionization time-of-flight mass spectrometry: A predictive tool for the lifetime of organic light emitting devices. *Applied Physics Letters*, 94(4):043314, jan 2009. doi: 10.1063/1.3075607.
- [124] Varatharajan Sivasubramaniam, Florian Brodkorb, Stephanie Hanning, Oliver Buttler, Hans Peter Loebel, Volker van Elsbergen, Herbert Boerner, Ullrich Scherf, and Martin Kreyenschmidt. Degradation of HTL layers during device operation in PhOLEDs. *Solid State Sciences*, 11(11):1933–1940, 2009. doi: 10.1016/j.solidstatesciences.2009.07.017.
- [125] Sebastian Reineke, Karsten Walzer, and Karl Leo. Triplet-exciton quenching in organic phosphorescent light-emitting diodes with Ir-based emitters. *Physical Review B*, 75(12):125328, mar 2007. doi: 10.1103/PhysRevB.75.125328.
- [126] David J. Larson, Baptiste Gault, Brian P. Geiser, Frederic De Geuser, and François Vurpillot. Atom probe tomography spatial reconstruction: Status and directions. *Current Opinion in Solid State and Materials Science*, 17(5):236–247, 2013. doi: 10.1016/j.cossms.2013.09.002.
- [127] Baptiste Gault, D. Haley, Frederic de Geuser, Michael P. Moody, Emmanuelle A. Marquis, David J. Larson, and Brian P. Geiser. Advances in the reconstruction of atom probe tomography data. *Ultramicroscopy*, 111(6):448–457, 2011. doi: 10.1016/j.ultramicro.2010.11.016.
- [128] David J. Larson, Brian P. Geiser, Ty J. Prosa, Stephan S.A. A Gerstl, David A. Reinhard, and Thomas F. Kelly. Improvements in planar feature reconstructions in atom probe tomography. *Journal of Microscopy*, 243(1):15–30, 2011. doi: 10.1111/j.1365-2818.2010.03474.x.
- [129] Daniel Beinke, Christian Oberdorfer, and Guido Schmitz. Towards an accurate volume reconstruction in atom probe tomography. *Ultramicroscopy*, 165:34–41, 2016. doi: 10.1016/j.ultramicro.2016.03.008.
- [130] Brian P. Gorman, A. Puthucode, David R. Diercks, and M. J. Kaufman. Cross-correlative TEM and atom probe analysis of partial crystallisation in NiNbSn metallic glasses. *Materials Science and Technology*, 24(6):682–688, jun 2008. doi: 10.1179/174328408X293595.
- [131] David R. Diercks, Brian P. Gorman, Rita Kirchhofer, Norman Sanford, Kris Bertness, and Matt Brubaker. Atom probe tomography evaporation behavior of C-axis GaN nanowires: Crystallographic, stoichiometric, and detection efficiency aspects. *Journal of Applied Physics*, 114(18):184903, 2013. doi: 10.1063/1.4830023.

- [132] W. Lefebvre, D. Hernandez-Maldonado, F. Moyon, F. Cuvilly, C. Vaudolon, D. Shinde, and F. Vurpillot. HAADF-STEM atom counting in atom probe tomography specimens: Towards quantitative correlative microscopy. *Ultramicroscopy*, 159:403–412, 2015. doi: 10.1016/j.ultramic.2015.02.011.
- [133] Patrick P. Camus, David J. Larson, and Thomas F. Kelly. A method for reconstructing and locating atoms on the crystal lattice in three-dimensional atom probe data. *Applied Surface Science*, 87-88(C):305–310, 1995. doi: 10.1016/0169-4332(94)00503-6.
- [134] Michael P. Moody, Baptiste Gault, Leigh T. Stephenson, Daniel Haley, and Simon P. Ringer. Qualification of the tomographic reconstruction in atom probe by advanced spatial distribution map techniques. *Ultramicroscopy*, 109(7):815–824, 2009. doi: 10.1016/j.ultramic.2009.03.016.
- [135] Michael P. Moody, Baptiste Gault, Leigh T. Stephenson, Ross K W Marceau, Rebecca C. Powles, Anna V. Ceguerra, Andrew J. Breen, and Simon P. Ringer. Lattice rectification in atom probe tomography: Toward true three-dimensional atomic microscopy. *Microscopy and Microanalysis*, 17(2):226–239, 2011. doi: 10.1017/S1431927610094535.
- [136] Anna V Ceguerra, Alec C Day, and Simon P Ringer. Assessing the Spatial Accuracy of the Reconstruction in Atom Probe Tomography and a New Calibratable Adaptive Reconstruction. *Microscopy and Microanalysis*, 25(02):309–319, apr 2019. doi: 10.1017/S1431927619000369.
- [137] François Vurpillot, L. Renaud, and Didier Blavette. A new step towards the lattice reconstruction in 3DAP. *Ultramicroscopy*, 95(SUPPL.):223–229, 2003. doi: 10.1016/S0304-3991(02)00320-0.
- [138] Emmanuelle A. Marquis and Francois Vurpillot. Chromatic Aberrations in the Field Evaporation Behavior of Small Precipitates. *Microscopy and Microanalysis*, 14(6): 561–570, dec 2008. ISSN 1431-9276. doi: 10.1017/S1431927608080793.
- [139] Christian Oberdorfer, Sebastian Manuel Eich, and Guido Schmitz. A full-scale simulation approach for atom probe tomography. *Ultramicroscopy*, 128:55–67, 2013. doi: 10.1016/j.ultramic.2013.01.005.
- [140] Ahmed Shariq, Talaat Al-Kassab, Reiner Kirchheim, and Ricardo B. Schwarz. Exploring the next neighbourhood relationship in amorphous alloys utilizing atom probe tomography. *Ultramicroscopy*, 107(9):773–780, 2007. doi: 10.1016/j.ultramic.2007.02.030.
- [141] James Munkres. Algorithms for the Assignment and Transportation Problems. *Journal of the Society for Industrial and Applied Mathematics*, 5(1):32–38, 1957.

- [142] Donald E. Knuth. Dancing links. *Millennial Perspectives in Computer Science: Proceedings of the 1999 Oxford–Microsoft Symposium in Honour of Sir Tony Hoare*, pages 187–214, 2000.
- [143] Ketan Date and Rakesh Nagi. GPU-accelerated Hungarian algorithms for the Linear Assignment Problem. *Parallel Computing*, 57:52–72, 2016. doi: 10.1016/j.parco.2016.05.012.
- [144] T. Philippe, F. De Geuser, S. Duguay, W. Lefebvre, O. Cojocar-Mirédin, G. Da Costa, and D. Blavette. Clustering and nearest neighbour distances in atom-probe tomography. *Ultramicroscopy*, 109(10):1304–1309, sep 2009. doi: 10.1016/j.ultramic.2009.06.007.
- [145] T. Philippe, S. Duguay, and D. Blavette. Clustering and pair correlation function in atom probe tomography. *Ultramicroscopy*, 110(7):862–865, jun 2010. doi: 10.1016/j.ultramic.2010.03.004.
- [146] Adrian Baddeley, Peter J. Diggle, Andrew Hardegen, Thomas Lawrence, Robin K. Milne, and Gopalan Nair. On tests of spatial pattern based on simulation envelopes. *Ecological Monographs*, 84(3):477–489, aug 2014. doi: 10.1890/13-2042.1.
- [147] Baptiste Gault, Shyeh Tjing Loi, Vicente J. Araullo-Peters, Leigh T. Stephenson, Michael P. Moody, Sachin L. Shrestha, Ross K.W. W Marceau, Lan Yao, Julie M. Cairney, and Simon P. Ringer. Dynamic reconstruction for atom probe tomography. *Ultramicroscopy*, 111(11):1619–1624, 2011. doi: 10.1016/j.ultramic.2011.08.005.
- [148] Chris Groves. Modeling OPV Performance—Morphology, Transport, and Recombination. In Barry P Rand and Henning Richter, editors, *Organic Solar Cells: Fundamentals, Devices, and Upscaling*, chapter 10, pages 497–535. Pan Stanford Publishing, Singapore, 2014. ISBN 978-981-4463-66-9.
- [149] Suhan Kim, Moon Jeong Park, Nitash P. Balsara, Gao Liu, and Andrew M. Minor. Minimization of focused ion beam damage in nanostructured polymer thin films. *Ultramicroscopy*, 111(3):191–199, 2011. doi: 10.1016/j.ultramic.2010.11.027.
- [150] Yufei Shen and Noel C. Giebink. Monte Carlo Simulations of Nanoscale Electrical Inhomogeneity in Organic Light-Emitting Diodes and Its Impact on Their Efficiency and Lifetime. *Physical Review Applied*, 4(5):1–12, nov 2015. doi: 10.1103/PhysRevApplied.4.054017.
- [151] T. Matsuo, H. Suga, W.I.F. David, R.M. Ibberson, P. Bernier, A. Zahab, C. Fabre, A. Rassat, and A. Dworkin. The Heat Capacity of Solid C60. *Solid State Communications*, 83(9):711–715, sep 1992. doi: 10.1016/0038-1098(92)90149-4.

## APPENDIX A

### TAPSIM PARAMETERS

Below is a listing of the configurations used in the evaporation simulation described in Chapter 5. The parameters are standard for TAPSim.[139]

#### A.1 Mesh Generation Configuration

LEVEL\_LIMIT = 0

INPUT\_XY\_EXPANSION = 2.3

INPUT\_Z\_EXPANSION = 1.5

INPUT\_PLC\_CONTOUR\_RADIUS = 100

INPUT\_PLC\_CONTOUR\_PHI = 16

INPUT\_PLC\_CONTOUR\_HEIGHT = 100

INPUT\_PLC\_RECOVERY\_RADIUS = 50

INPUT\_PLC\_RECOVERY\_PHI = 32

INPUT\_PLC\_RECOVERY\_HEIGHT = 1e-08

INPUT\_CYLINDER\_XY\_EXPANSION = 7.5

INPUT\_CYLINDER\_Z\_EXPANSION = 7.5

INPUT\_CYLINDER\_RESOLUTION = 32

FIRST\_LEVEL\_TETGEN\_PARAMS = zpqQa

FIRST\_LEVEL\_VOLUME\_CONSTRAINTS = 1.33333e-27

SECOND\_LEVEL\_TETGEN\_PARAMS = zpqQ

SECOND\_LEVEL\_MAXIMUM\_CONSTRAINTS = 1.79769e+308

THIRD\_LEVEL\_CYLINDER\_RADIUS = 4e-06  
THIRD\_LEVEL\_CYLINDER\_HEIGHT = 1e-06  
THIRD\_LEVEL\_INNER\_CYLINDER\_RESOLUTION = 64  
THIRD\_LEVEL\_OUTWARD\_CYLINDER\_RESOLUTION = 64  
THIRD\_LEVEL\_MAXIMUM\_CONSTRAINTS = 1.79769e+308

FOURTH\_LEVEL\_CYLINDER\_RADIUS = 0.4  
FOURTH\_LEVEL\_CYLINDER\_HEIGHT = 0.1  
FOURTH\_LEVEL\_INNER\_CYLINDER\_RESOLUTION = 32  
FOURTH\_LEVEL\_OUTWARD\_CYLINDER\_RESOLUTION = 512  
FOURTH\_LEVEL\_MAXIMUM\_CONSTRAINTS = 1.66667e-07

MINIMUM\_VOLUME = 2.08333e-27  
VOLUME\_DECAY\_EXPONENT = 3

DISTANCE\_MEASURE\_RADIUS\_RESOLUTION = 1000  
DISTANCE\_MEASURE\_THETA\_RESOLUTION = 32  
DISTANCE\_MEASURE\_PHI\_RESOLUTION = 64

MAXIMUM\_REFINE\_CYCLES = 15  
REFINE\_THRESHOLD = 0

MAXIMUM\_EDGE\_FILTER\_CYCLES = 15  
EDGE\_FILTER\_LENGTH = 5e-10

VACUUM\_MARKER = 0  
TOP\_MARKER = 1

BOTTOM\_MARKER = 2

SIDES\_MARKER = 3

ASCII\_OUTPUT\_MODE = 0

## A.2 Sample Configuration

ASCII

TEMPERATURE = 0.00000e+00

ID = 0

NAME = Vacuum

CHARGE\_DENSITY = 0.00000e+00

DIELECTRICITY = 1.00000e+00

REMOVABLE = 0

NEUMANN\_BOUNDARY = 0

DIRICHLET\_BOUNDARY = 0

POTENTIAL = 0.00000e+00

MASS = 0.00000e+00

EVAPORATION\_CHARGE\_STATE = 0

EVAPORATION\_FIELD\_STRENGTH = 0.00000e+00

EVAPORATION\_ACTIVATION\_ENERGY = 0.00000e+00

ID = 1

NAME = Top

CHARGE\_DENSITY = 0.00000e+00

DIELECTRICITY = 1.00000e+00

REMOVABLE = 0

NEUMANN\_BOUNDARY = 0  
DIRICHLET\_BOUNDARY = 1  
POTENTIAL = 0.00000e+00  
MASS = 0.00000e+00  
EVAPORATION\_CHARGE\_STATE = 0  
EVAPORATION\_FIELD\_STRENGTH = 0.00000e+00  
EVAPORATION\_ACTIVATION\_ENERGY = 0.00000e+00

ID = 2  
NAME = Bottom  
CHARGE\_DENSITY = 0.00000e+00  
DIELECTRICITY = 1.00000e+00  
REMOVABLE = 0  
NEUMANN\_BOUNDARY = 1  
DIRICHLET\_BOUNDARY = 0  
POTENTIAL = 1.00000e+03  
MASS = 0.00000e+00  
EVAPORATION\_CHARGE\_STATE = 0  
EVAPORATION\_FIELD\_STRENGTH = 0.00000e+00  
EVAPORATION\_ACTIVATION\_ENERGY = 0.00000e+00

ID = 3  
NAME = Sides  
CHARGE\_DENSITY = 0.00000e+00  
DIELECTRICITY = 1.00000e+00  
REMOVABLE = 0  
NEUMANN\_BOUNDARY = 0

DIRICHLET\_BOUNDARY = 1  
POTENTIAL = 0.00000e+00  
MASS = 0.00000e+00  
EVAPORATION\_CHARGE\_STATE = 0  
EVAPORATION\_FIELD\_STRENGTH = 0.00000e+00  
EVAPORATION\_ACTIVATION\_ENERGY = 0.00000e+00

ID = 10  
NAME = Silicon  
CHARGE\_DENSITY = 0.00000e+00  
DIELECTRICITY = 1.00000e+06  
REMOVABLE = 1  
NEUMANN\_BOUNDARY = 0  
DIRICHLET\_BOUNDARY = 1  
POTENTIAL = 1.00000e+03  
MASS = 28.086  
EVAPORATION\_CHARGE\_STATE = 2  
EVAPORATION\_FIELD\_STRENGTH = 33.0e-9  
EVAPORATION\_ACTIVATION\_ENERGY = 1.00000e+00

ID = 11  
NAME = Boron  
CHARGE\_DENSITY = 0.00000e+00  
DIELECTRICITY = 1.00000e+06  
REMOVABLE = 1  
NEUMANN\_BOUNDARY = 0  
DIRICHLET\_BOUNDARY = 1

POTENTIAL = 1.00000e+03  
MASS = 10.811  
EVAPORATION\_CHARGE\_STATE = 1  
EVAPORATION\_FIELD\_STRENGTH = 64.0e-9  
EVAPORATION\_ACTIVATION\_ENERGY = 1.00000e+00

### A.3 Evaporation Configuration

RESULTS\_FILENAME = results\_data  
RESULTS\_BINARY\_OUTPUT = 0  
RESULTS\_CHUNK\_SIZE = 10000

TRAJECTORY\_FILENAME = trajectory\_data  
TRAJECTORY\_BINARY\_OUTPUT = 0  
TRAJECTORY\_CHUNK\_SIZE = 10000

GRID\_FILENAME = grid\_data  
GRID\_BINARY\_OUTPUT = 1  
GRID\_INTERVAL = 2147483647

SURFACE\_FILENAME = surface\_data  
SURFACE\_BINARY\_OUTPUT = 1  
SURFACE\_INTERVAL = 2147483647

GEOMETRY\_FILENAME = geometry.dat  
GEOMETRY\_BINARY\_OUTPUT = 1  
GEOMETRY\_CONTENTS = 0xff

DUMP\_FILENAME = dump

DUMP\_INTERVAL = 10000

OUTPUT\_DELAY\_TIME = 60

METHOD\_EVAPORATION\_PROBABILITY = 0

METHOD\_EVAPORATION\_CHOICE = 0

VACUUM\_CELL\_IDENTIFIERS = Vacuum

COMPUTE\_TRAJECTORY = 1

TRAJECTORY\_INTEGRATOR\_TYPE = 1

TRAJECTORY\_STEPPER\_TYPE = 1

TRAJECTORY\_INITIAL\_TIME\_STEP = 1e-14

TRAJECTORY\_MINIMUM\_TIME\_STEP = 1e-16

TRAJECTORY\_ERROR\_THRESHOLD = 1e-6

TRAJECTORY\_NON\_RANDOM\_START\_POSITION = 1

TRAJECTORY\_NO\_INITIAL\_VELOCITY = 1

VOLTAGE\_QUEUE\_SIZE = 0

LOCAL\_RELAXATION\_ERROR\_THRESHOLD = 1e-2

LOCAL\_RELAXATION\_SHELL\_SIZE = 3

LOCAL\_RELAXATION\_CYCLE\_SIZE = 5

LOCAL\_RELAXATION\_QUEUE\_SIZE = 5

GLOBAL\_RELAXATION\_STEPS = 1

REFRESH\_RELAXATION\_INTERVAL = 0

REFRESH\_RELAXATION\_ERROR\_THRESHOLD = 0.0

REFRESH\_RELAXATION\_CYCLE\_SIZE = 100

REFRESH\_RELAXATION\_QUEUE\_SIZE = 25

## APPENDIX B

### EVAPORATION FIELDS

Because we have analyzed a number of compounds to this point, estimating the zero-barrier evaporation field ( $F_E$ ) is useful to understand how these small-molecule organic semi-conducting materials behave as compared to more traditional materials analyzed with APT.

#### B.1 Radius Only $F_E$ Estimation

A basic assumption of APT is that the field strength at the surface is given by:[65]

$$F = \frac{V}{Rk_f} \quad (\text{B.1})$$

The first, most simplistic way to estimate the evaporation field is assuming that the temperature and laser pulse energy do not matter and that the onset evaporation voltage,  $V_{\text{onset}}$ , is equivalent to the free evaporation voltage,  $V_E$ . Then,

$$F_E \approx \frac{V_{\text{onset}}}{Rk_f} \quad (\text{B.2})$$

Using Table 3.1, we can crudely estimate the evaporation field (Table B.1). It is interesting to note that all of these estimates are below  $10 \text{ V nm}^{-1}$ , making them quite small compared to typical APT materials.[63] For trends, we can look at how the field changes with molecular weight, which might be expected to be proportional to the ease of evaporation. Figure B.1 shows that there is mild evidence for increasing evaporation field with molecular weight, but it is likely obscured by temperature and pulse energy effects. Similarly, comparing the field to the deposition power<sup>1</sup> used to thermally evaporate the material (Figure B.2) shows similar behavior. This suggests that correcting for temperature and pulse energy effects may uncover a stronger correlation.

---

<sup>1</sup>This is an internal parameter (expressed as a percentage) on the Angstrom Engineering deposition system.

Table B.1: A table evaporation fields based on the evaporation parameters in Table 3.1. The fields are calculated solely based on Equation B.2, and do not account for the pulse energy or sample temperature.

<b>Material</b>	<b>Evaporation Field (V/nm)</b>
Alq <sub>3</sub>	4.61
Alq <sub>3</sub>	2.36
BPhen	2.06
C <sub>60</sub>	2.67
C <sub>60</sub>	0.73
CBP	4.24
DCM2	2.61
DIP	3.64
DIP	4.55
Ir(ppy) <sub>3</sub>	3.03
Ir(ppy) <sub>3</sub>	4.70
mCBP	2.79
SimCP2	4.73
Tc	1.33
Tc	0.85
TCP	4.24
TCP	4.24

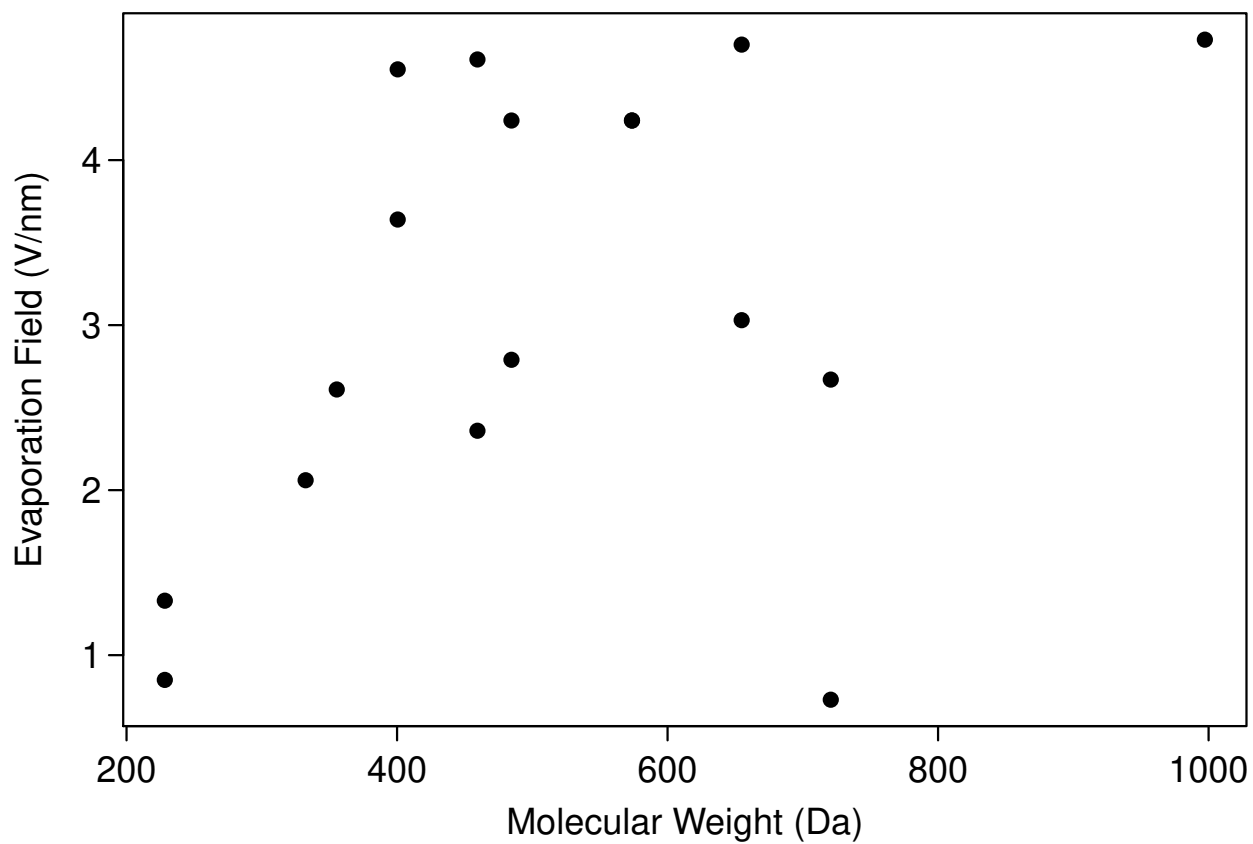


Figure B.1: The crudely estimated evaporation fields (Table B.1) versus molecular weight. There appears to be a weak trend, but the relationship is likely obscured by temperature and pulse energy effects that are not accounted for by Equation B.2.

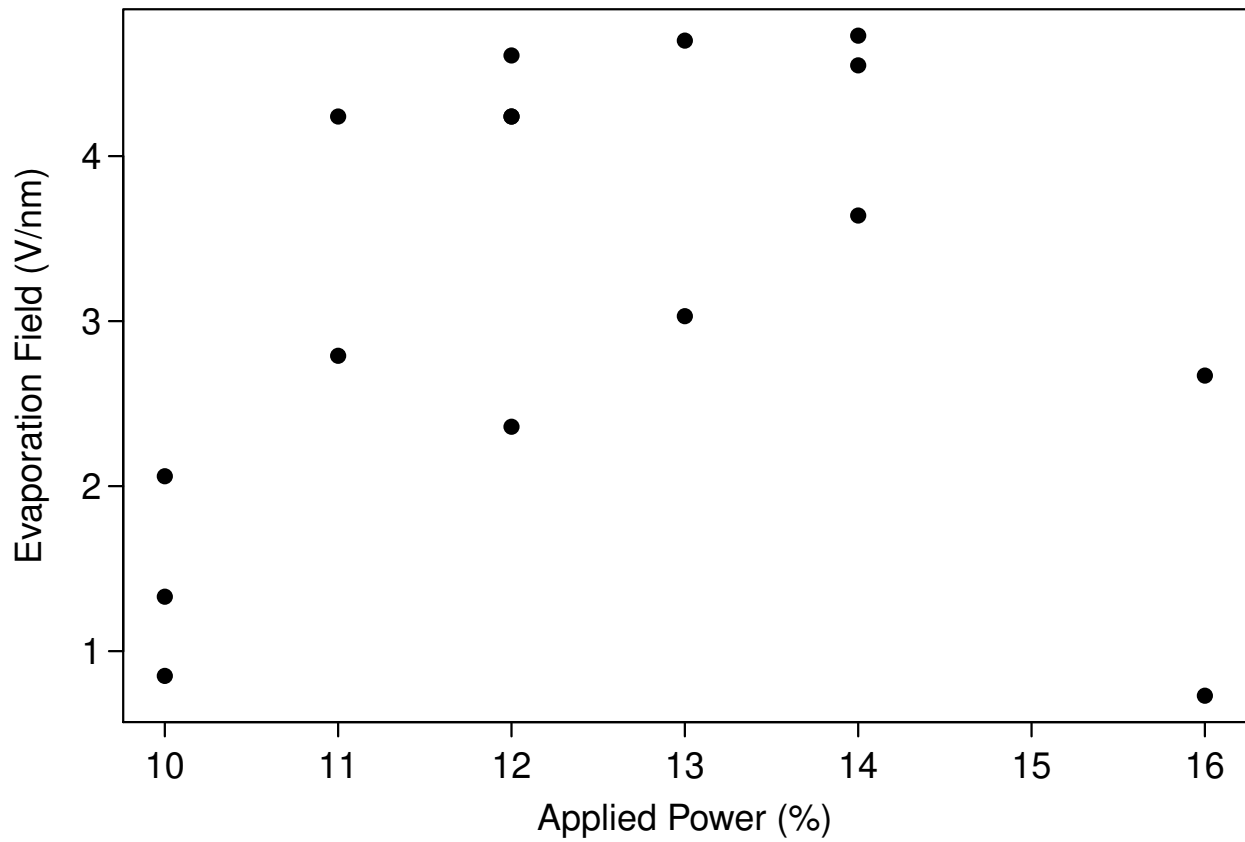


Figure B.2: The crudely estimated evaporation fields (Table B.1) versus deposition power. Similar to Figure B.1, it seems that the expected trend is mostly obscured by temperature and pulse energy effects.

## B.2 $F_E$ Including $E_p$ and $T$

If we assume thermal activation for the ionization process (escape charge state) to define the rate[65]

$$r = An_{\text{hr}} \exp\left(-\frac{Q_n(F)}{k_B T}\right)$$

we can make some assumptions and transformations that will allow us to estimate  $F_E$ . Assuming the laser pulse is a purely thermal effect, we change the denominator of the exponential as  $Tk_B \rightarrow Tk_B + \alpha\delta_n E_p$ , where  $\delta_n$  is a pulse energy conversion factor that is likely material dependent and  $\alpha$  is a geometric conversion factor to account for the cross-section of the sample in the laser path.

For the numerator of the exponential, close to  $F_E$  we can assume the field sensitivity is linear, taking the form  $Q = \beta_n(F - F_E)$  because of the definition that  $Q_n(F_E) \equiv 0$ . [65] Assuming the field is given by B.1, we make a linear approximation of  $Q(F)$  near  $F_E$ :

$$Q \approx \beta_n \left( \frac{V}{k_f R} - F_E \right)$$

With these simplifying assumptions, the rate equation becomes

$$r = A_n n_{\text{hr}} \exp\left(-\beta_n \frac{\frac{V}{k_f R} - F_E}{k_B T + \alpha\delta_n E_p}\right)$$

As stated in Chapter 4, the LEAP uses a laser pulse with a gaussian beam shape having a diameter of  $3\ \mu\text{m}$  at  $4\sigma$ , meaning that  $\sigma = 375\ \text{nm}$ . For the most simplistic assumption of a circular cross-section, this means that

$$\alpha(R) = 1 - \exp\left(-\frac{1}{2} \left(\frac{R}{\sigma}\right)^2\right)$$

Using a sample detector distance of  $d = 90\ \text{mm}$  and an approximate detector radius for collected ions of  $r_d = 30\ \text{mm}$ , we can make a crude estimate of the field of view. The maximum angle is  $\theta = \tan^{-1} \frac{r_d}{d}$ , meaning that the visible area is

$$A_s = R^2 \Omega = 2\pi R^2 \cos \theta = \frac{2\pi R^2}{\sqrt{\left(\frac{r_d}{d}\right)^2 + 1}}$$

If we approximate a molecule as having a cross-sectional area of  $A_m = 1 \text{ nm}^2$ , this means

$$n_{\text{hr}} = \eta \xi \frac{2\pi R^2}{\sqrt{\left(\frac{r_d}{d}\right)^2 + 1}}$$

where  $\eta$  is the detection efficiency and  $\xi$  is the fraction of high probability surface molecules.

As a side note, with this field-of-view calculation, assuming a detection efficiency of 55 % (standard for the LEAP), we can estimate the evaporation radius of curvature. For example, in a 100 nm thick Ir(ppy)<sub>3</sub> sample with a total ion count of  $\sim 30 \times 10^6$ , if we assume that each layer is 1 nm thick this says that the radius is 303 nm. This is approximately what we estimate based on the crude calibration provided by the “hit ring” that appears on smaller radius tips, which we attribute to the substrate radius of curvature being smaller than that of the equilibrium evaporation radius.

In addition to the assumptions listed above, to make this problem easier with the limited measurements currently available, we assume:

- $\delta_n = \delta$  (*i.e.* the pulse energy conversion factor is material independent)
- $\beta_n = \beta$  (*i.e.* the linearized field sensitivity factor is material independent)
- $A_n = A$  (*i.e.* the rate constant pre-factor is material independent)
- $k_f$  is the same for all samples

These additional assumptions result in the rate equation we will use to estimate  $F_E$ :

$$r = A\eta\xi \frac{2\pi R^2}{\sqrt{\left(\frac{r_d}{d}\right)^2 + 1}} \exp\left(-\beta \frac{V}{k_f R} - F_E\right) \quad (\text{B.3})$$

### B.2.1 Application to Ir(ppy)<sub>3</sub>

We begin with Ir(ppy)<sub>3</sub> because it has a pulse energy series (see Chapter 4) that measured the voltage as a function of pulse energy on the same sample; the radius of curvature for

the particular sample substrate is  $R = 330 \text{ nm}$ . Using Equation B.3, we know that for measurements on the same sample

$$\frac{V - V_E}{k_B T + \alpha \delta E_p} = \text{const.}$$

where we have converted  $V_E = F_E k_f R$  because these are measured on the same sample. This means we can write

$$V(E_p) = C \alpha \delta E_p + C k_B T + V_E \quad (\text{B.4})$$

Thus, a fit to the form  $ax + b$  allows us to extract  $C = \frac{a}{\alpha \delta}$  and thus

$$V_E = b - \frac{a}{\alpha \delta} k_B T$$

The voltage data and fit are shown in Figure B.3. First, the behavior of the data does appear linear, indicating that the simplifying assumptions made thus far are consistent with the data. Not knowing the value of  $\delta$ , we can make a first approximation using  $V_E = b$ , which gives  $F_E = 7.1 \text{ V nm}^{-1}$ .

The best way to estimate  $\delta$  is by measuring  $V(T)$ ; that is, measure how voltage changes with temperature while holding the evaporation rate and pulse energy constant. However, such a series is currently unavailable, so we must use alternative methods.

Given how we have defined  $\delta$  in Equation B.3, we can equate this to a heat capacity of the material:

$$\delta = \frac{k_B}{C_p N_m}$$

where  $N_m$  is the number of molecules of the interaction. As above, if we choose a spherical interaction volume defined by the sample radius and assume a molecule has a volume of  $1 \text{ nm}^3$ , this becomes

$$\delta = \frac{3k_B}{4\pi C_p R^3}$$

so this allows us to modify how we extract  $V_E$  from Equation B.4 to

$$V_E = b - \frac{4\pi a C_p R^3}{3\alpha} T$$

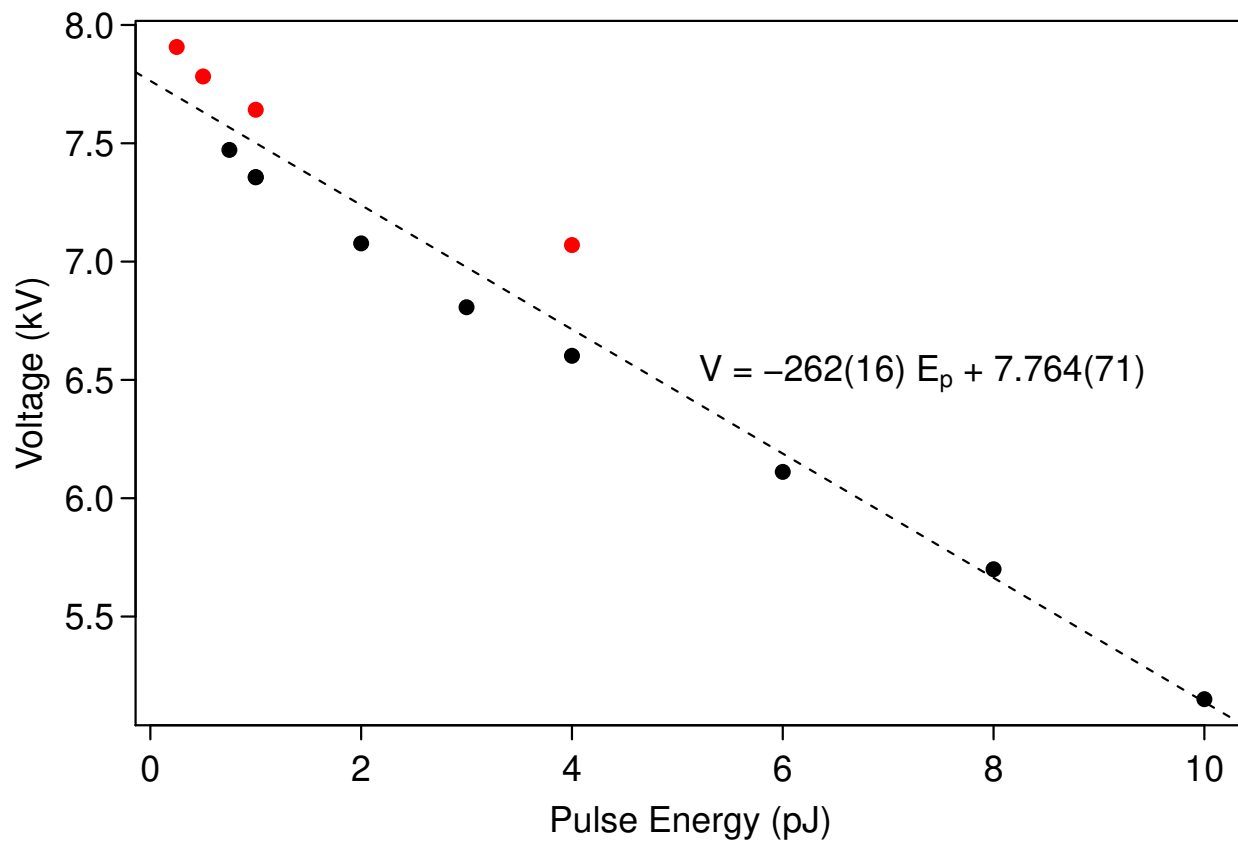


Figure B.3: Equilibrium evaporation voltage of  $\text{Ir}(\text{ppy})_3$  versus laser pulse energy. Fitting with Equation B.4 gives  $C\alpha\delta = 262 \pm 16 \text{ kV J}^{-1}$  and  $Ck_B T + V_E = 7.764 \pm 0.071 \text{ kV}$  with  $R^2 = 0.96$ . Simply using the intercept of this fit gives an estimate of  $F_E = 7.1 \text{ V nm}^{-1}$  for  $\text{Ir}(\text{ppy})_3$ .

### B.2.2 Estimating $F_E$ from Table 3.1

We are nearly ready to get evaporation field values from the table. The final piece is to estimate  $\beta$ , the field sensitivity.

With the fit using the Ir(ppy)<sub>3</sub> pulse energy series, we choose  $C_p = 50 \text{ J K}^{-1} \text{ mol}^{-1}$  in line with the measured value for C<sub>60</sub> at these temperatures,[151] which gives  $F_E = 7.4 \text{ V nm}^{-1}$ . We can then use this evaporation field to estimate  $\beta$  using the two measurements of Ir(ppy)<sub>3</sub> from the table by equating their rates in Equation B.3

$$\beta = \frac{2k_f R_1 R_2 (k_b T_1 + \alpha_1 \delta_1 E_1) (k_b T_2 + \alpha_2 \delta_2 E_2) \log(R_1/R_2)}{k_B R_2 T_2 V_1 - k_B R_1 T_1 V_2 - \alpha_1 \delta_1 E_1 R_1 V_2 + \alpha_2 \delta_2 E_2 R_2 V_1 + F_E k_f R_1 R_2 (k_B T_1 - k_B T_2 + \alpha_1 \delta_1 E_1 - \alpha_2 \delta_2 E_2)}$$

Assuming the tabulated values in Table 3.1 are at the same rate, we can solve for the evaporation field by equating rates in Equation B.3:

$$F_E = \frac{\frac{V_1 \beta}{k_B k_f R_1 T_1 + k_f R_1 \alpha_1 \delta_1 E_1} - \frac{V_2 \beta}{k_B k_f R_2 T_2 + k_f R_2 \alpha_2 \delta_2 E_2} - 2 \log(R_1/R_2)}{\beta ((k_B T_1 + \alpha_1 \delta_1 E_1)^{-1} - (k_B T_2 + \alpha_2 \delta_2 E_2)^{-1})} \quad (\text{B.5})$$

Because this method requires two measurements, we can only fill out part of the table; the estimated evaporation fields for these materials are given in Table B.2. Even with these adjustments, all of the measured materials have evaporation fields around or below  $10 \text{ V nm}^{-1}$ . These corrections improve the trend with molecular weight (Figure B.4) and deposition power (Figure B.5), showing a clearer relationship in line with expectations.

Table B.2: The estimated fields based on Table 3.1 accounting for the temperature and laser pulse energy, assuming a uniform heat capacity of  $C_p = 50 \text{ J K}^{-1} \text{ mol}^{-1}$  in the estimate of  $\delta$  in Equation B.5; the values for CBP and mCBP are the same because they were used together to fulfill the two measurement requirement. The estimated error is  $\pm 1 \text{ V nm}^{-1}$ .

Material	Evaporation Field (V/nm)
Alq <sub>3</sub>	3.1
C <sub>60</sub>	10.3
CBP	4.8
DIP	6.5
Ir(ppy) <sub>3</sub>	7.4
mCBP	4.5
Tc	1.7
TCP	5.4

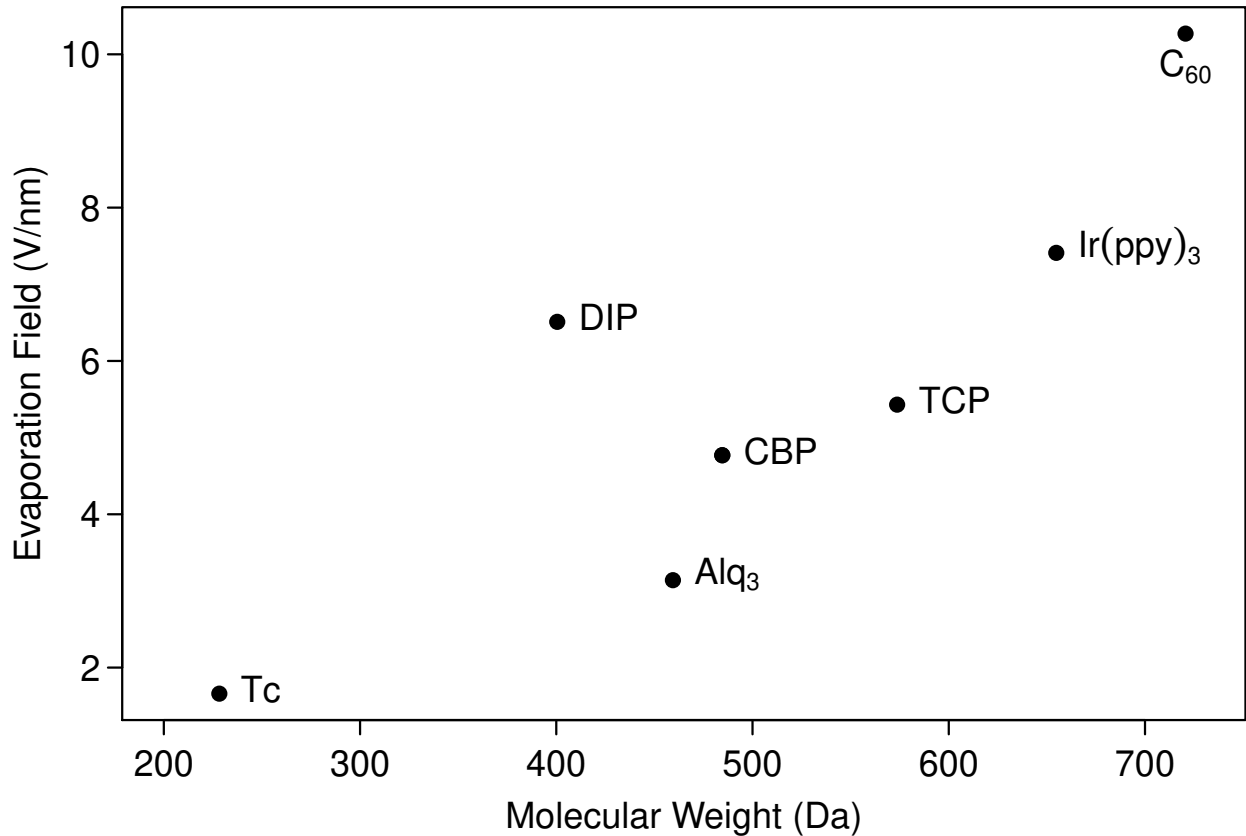


Figure B.4: The estimated evaporation fields (Table B.2) versus molecular weight. The trend that was somewhat apparent in the basic field evaporation estimates (Figure B.1) is much clearer.

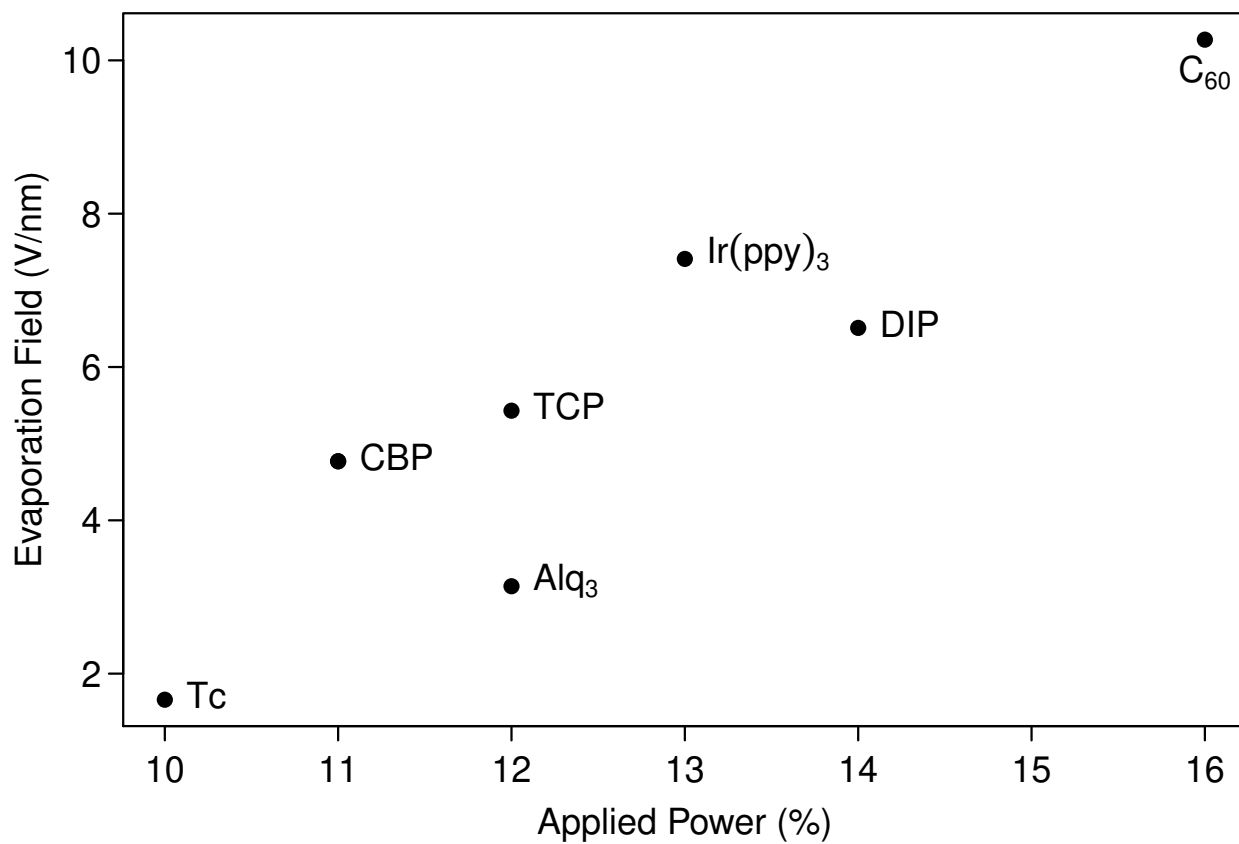


Figure B.5: The estimated evaporation fields (Table B.2) versus deposition power. The trend that was somewhat apparent in the basic field evaporation estimates (Figure B.2) is much clearer.